THE UNIVERSITY OF MANITOBA

A STUDY OF THE $^{3}H(p,pn)d$, $^{3}H(p,pn)d^{*}$, AND $^{3}H(p,dn)p$ REACTIONS AT 45.4 MEV

by

D. J. ROBERTS

A THESIS

SUBMITTED TO THE FACULTY OF GRADUATE STUDIES

IN PARTIAL FULFILMENT OF THE REQUIREMENTS FOR THE DEGREE

OF DOCTOR OF PHILOSOPHY

DEPARTMENT OF PHYSICS

WINNIPEG, MANITOBA

FEBRUARY, 1976

"A STUDY OF THE $^{3}H(p,pn)d$, $^{3}H(p,pn)d^{*}$, AND $^{3}H(p,dn)p$ REACTIONS AT 45.4 MEV"

by

D.J. ROBERTS

A dissertation submitted to the Faculty of Graduate Studies of the University of Manitoba in partial fulfillment of the requirements of the degree of

DOCTOR OF PHILOSOPHY

ABSTRACT

The $^3H(p,pn)d$, $^3H(p,pn)d^*$, and $^3H(p,dn)p$ reactions have been studied at an incident proton energy of 45 MeV for a variety of coplanar symmetric and asymmetric angle pairs. Here d* refers to an n-p pair at low relative energy in a singlet spin state. The coincidence cross sections have been compared to predictions of the Simple Impulse Approximation (SIA) for quasi-free scattering modified by an attenuation coefficient. In a semi-classical model, this coefficient is the product of the transmission probabilities for the outgoing neutron and proton not to interact with the spectator deuteron and so contribute to the dominant reaction mechanism, quasi-free scattering. Repulsive core Eckart functions have been used to describe the tri-nucleon bound state as a system of a neutron and deuteron. An anisotropic half-off-the-energy-shell t-matrix was used to describe the scattering of a neutron and proton. Total cross sections for neutron-deuteron scattering in the doublet state were generated from a phase shift analysis for use in the attenuation model calculation.

The experimental peak cross section data for the $^3H(p,pn)d$ reaction exhibit a strong angular dependence while that of $^3H(p,pn)d^*$ does not. This effect is not predicted by either the attenuation model or SIA. The peaks are also sometimes shifted from the positions predicted by these theories. The SIA overestimates the cross sections, while the attenuation model underestimates them unless the cross sections used in the

transmission coefficient calculation are reduced in magnitude by 30%. In the $^{3}H(p,dn)p$ spectra, peaks are observed for kinematic conditions suggesting that the proton is a spectator and a quasi-free reaction occurs. The reaction is $p+(nn) \rightarrow d+n$, where (nn) is a di-neutron in the ^{3}H target nucleus.

ACKNOWLEDGEMENTS

I would like to express my appreciation to all who have contributed to this project. Dr. D.O. Wells introduced me to nuclear physics and acted as my supervisor. Drs. J.W. Watson and D.I. Bonbright guided me during the experimental measurements, analysis of the data, and preparation of this thesis. Dr. W.T.H. van Oers provided valuable advice on many occasions and Dr. C.A. Miller originated some of the data collection and analysis procedures. Drs. J.P. Svenne and B.S. Bhakar counselled with respect to various theoretical questions.

I would also like to thank Dr. A.M. McDonald for assistance during the experiment, Mr. John Bruckshaw for sharing his drafting expertise, the cyclotron staff, and the many undergraduate students who participated in the data collection.

I am also grateful to the National Research Council, Atomic Energy Control Board, and University of Manitoba for financial assistance.

This manuscript was typeset using the IBM Program Product "Text360" as modified by the University of Manitoba Computer Centre.

TABLE OF CONTENTS

LIST OF FIGURES

Chapter 1

INTRODUCTION

Section 1.1 Historical Review

During the 1960's, work on the few-body problem became quite popular. This was chiefly due to three important factors. Firstly, many advances in technology were made. The predominant experimental technique up to this time used a single counter to detect protons from breakup reactions (T58). However, the study of many important aspects of three-body reactions requires knowledge of some parameters that a single counter experiment masks by integrating over too large a phase space volume. If two known particles from a reaction with three particles in the final state are detected at given angles and their energies are measured, the experiment is called kinematically complete, because the direction and energy of the third particle can be determined analytically; all kinematic parameters are measured or can be calculated. Two outgoing particles are detected in coincidence, that is, almost simultaneously. In order to determine particle types, it is necessary to use a stack of two detectors at both angles. Thus, the minimum configuration for a typical kinematically complete experiment consists of four detectors in coincidence. Recently developed semiconductor detectors, modern trigger circuits, and advanced modular electronics allowed the construction of sophisticated coincidence circuits having good timing and energy resolution at reasonable cost. The new

sector-focused cyclotrons produced more intense, better quality beams around 50 MeV so that more angles could be scanned in experiments. Higher beam currents were also required because coincidence experiments measure cross sections that are typically 200 times smaller than those measured in single counter experiments.

Secondly, there was an increasing appreciation of the need for a better understanding of the few-body problem. The three-body system was particularly interesting because, in the impulse approximation of Chew and Low (C59), the deuteron provides an essentially free neutron target. The projectile is assumed to interact with only one of a pair of particles forming the target. Neutron beams were difficult to obtain and so proton scattering from deuterium provided one of the best methods of obtaining information on the proton-neutron interaction. Also, the only method of obtaining neutron-neutron scattering parameters has been through a final state interaction (FSI) in a multi-particle reaction. By selecting appropriate kinematic regions in photo-, electro-, nucleon or pion induced disintegration of ^{2}H, ^{3}H, or ^{3}He, enhancements could be observed due to the low energy interaction of two nucleons. The three-body system must be understood in order to extract the accurate information on the two-body interaction that these experiments can supply. A comprehensive review of the effectiveness of the various experiments in determining two-body data from three-particle reactions has been given by van Oers (Va71). It was also hoped to determine if three-body forces

exist.

The third stimulus for work on the three-body problem came in 1961 when Kuckes, Wilson, and Cooper (K61) improved the accuracy of three-body breakup calculations with a new formulation of the impulse approximation (now called the Simple Impulse Approximation, SIA). It avoided the use of zero range or Born approximations by substituting an experimental cross section for the potential describing the two-body interaction. Consider a reaction 2(1,34)5. In the impulse approximation, the target 2 (a composite of particles 4 and 5) is broken up as the projectile 1 scatters inelastically from particle 4. The projectile is then detected as particle 3. The recoil particle 5 is undisturbed and retains the same momentum that it had before the reaction took place; it plays the role of a "spectator" to the reaction. This process is called quasi-free scattering (QFS) or a "knockout reaction", and represents only the first (pcle) term in a multiple scattering series depicted schematically in Figure 1.1.1. The approach of Kuckes et al yields a cross section which may be written in the laboratory frame (G70) as

$$\frac{d^3\sigma}{d\Omega_3\, d\Omega_4\, dE_3} = S \cdot KF \cdot |\phi(q)|^2 \cdot \frac{d\sigma}{d\Omega_{34}^{cm}}$$

where S is a spin factor, KF is a kinematic factor

$$KF = p_3 p_4^2 E_5 E_{34}^2{}_{cm} / \left[p_1 \sqrt{m_4^2 + p_5^2}\, |p_4 E_5 + E_4 (p_4 - p_1 \cos\theta_4 + p_3 \cos\theta_{34})| \right]$$

$\phi(q)$ is the wavefunction describing the relative momentum distribution of the two bodies forming the target, and $\frac{d\sigma}{d\Omega_{34}^{cm}}$ is

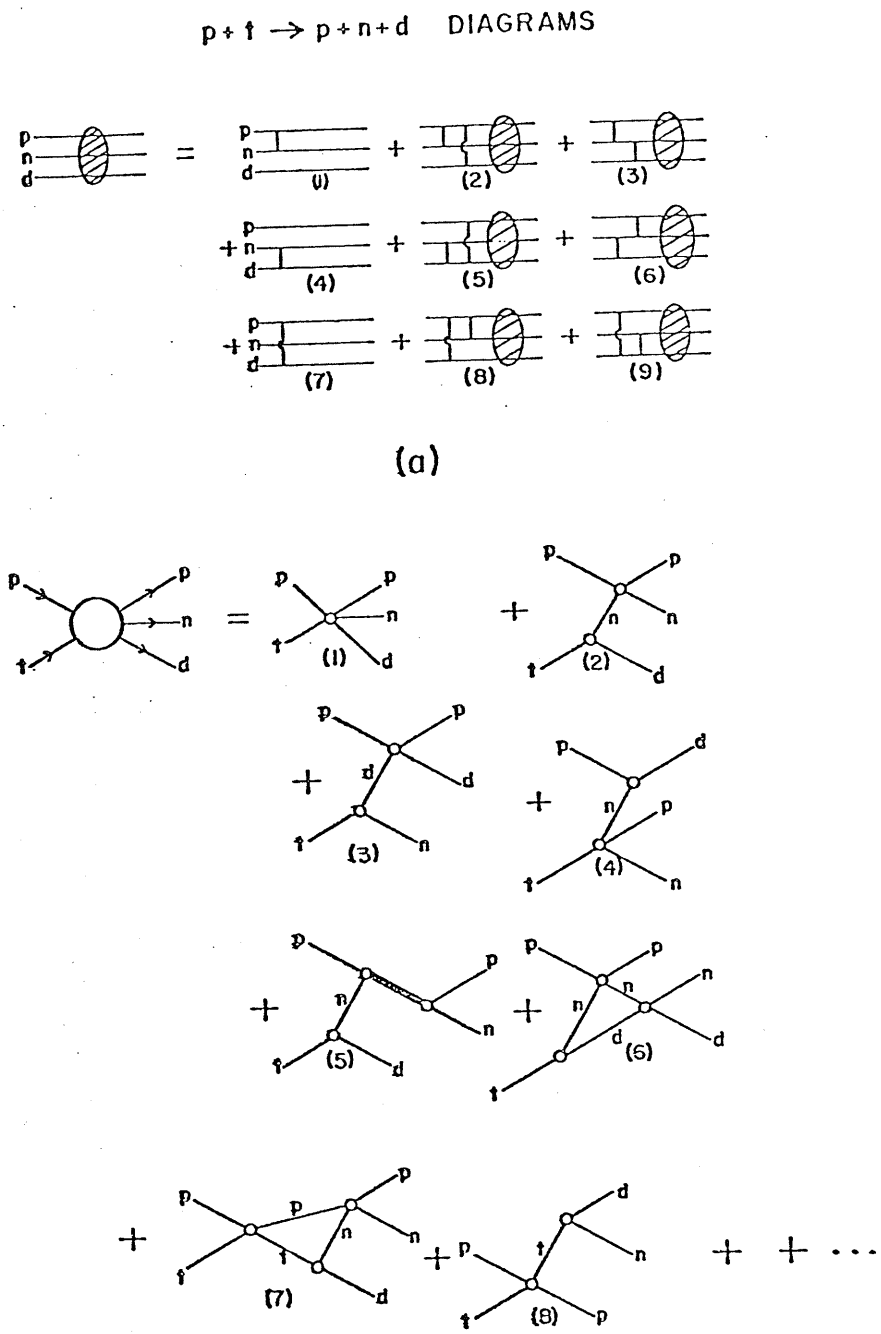

Figure 1.1.1 (a) Exact Faddeev Feynmann diagram expansion for p+t⟶p+n+d
(b) Some individual terms in the multiple scattering series
1) instantaneous breakup 2) p-n QFS
3) p-d QFS 4) neutron pickup 5) n-p FSI
6) triagle diagram 7) initial state scatter before QFS 8) sequential process

a two-body scattering cross section for particles 3 and 4. In the SIA then, the momentum p5 of the recoil particle is equal to the relative momentum q of particles 4 and 5 in the target nucleus at the instant of collision, because particle 5 has not engaged in any interaction after the collision occurred. In general, the shape of the QFS peak is determined by $\phi(q)$, but the magnitude is proportional to the two-body cross section. This cross section cannot be measured in a two-body experiment because the t-matrix that it replaces is off-the-energy-shell (i.e. $p^2+m^2 \neq E^2$, one of the particles is bound to the spectator). Usually an elastic (i.e. free scattering) cross section is used, but the process is basically inelastic. The relative error (proportional to the ratio of binding energy to projectile energy) decreases with increasing projectile energy. A necessary but not sufficient condition for the dominance of the pole graph is invariance in the Trieman-Yang angle (T62). Several experiments on deuterium have tested for invariance in the Trieman-Yang angle with opposing conclusions (C71), but no work has been done on tritium breakup (or with two different outgoing particles being detected).

It would be preferable to include all pairwise interactions among the three particles when performing a calculation. It was known, however, that the three-body Lippmann-Schwinger equations, which describe the collision exactly within the framework of nonrelativistic quantum mechanics, were intractable. Noncompact kernels in the integral equations lead to solutions which are not unique. An unexpected improvement in

the theoretical picture occurred in 1961 when Faddeev (F61) was able to rearrange the three-body equations and render them solvable in principle. Other groups (A63) improved on this formulation, notably by reducing the number of degrees of freedom by using t-matrices which were separable into products of functions of the initial and final coordinates. Several groups (Ca71) used such calculations to extract nucleon-nucleon scattering parameters from their data, but the codes were not widely distributed.

It is useful to study some Feynman diagrams relating to relevant physical processes. Consider Figure 1.1.1. Part (a) shows an exact Faddeev expansion for three-body scattering. The first and seventh terms represent QFS while the fourth term represents no scattering at all. The other diagrams are more complicated. Part (b) shows some individual terms in the series. Graph (1) represents instantaneous breakup of the three-body system and is usually considered to be relatively independent of momentum transfer. It thus forms a background. (Strictly speaking, this graph does not represent any single term in the Faddeev series.) Usually, only one of the two QFS diagrams (2) and (3) contributes significantly to the cross section. If a proton and neutron are detected at forward angles, then it is likely that the incident proton may have struck the neutron, and diagram (2) dominates. Similarly, if a proton and deuteron are detected at forward angles, diagram (3) dominates. Diagram (4) represents neutron pickup. Graph (5) represents an FSI of a neutron and proton. This is unlikely to

occur at the angles considered, but the p-d or n-p FSI should contribute at the boundary of the QFS enhancement. Proximity scattering could be represented by the triangle diagram (6), while (7) shows initial state scattering before QFS. Graph (8) describes a sequential process. The excited (internal) particle "t" is short-lived and so this diagram should be unimportant. However, the process would be observed as an enhancement parallel to an energy axis. These are only a few of the terms contributing, but they represent some of the processes for which the cross section can most strongly vary. It is hoped that in selected regions of phase space one can associate the behavior of the cross section with individual terms or a coherent addition of several terms.

Section 1.2 Experimental Work on the Trion

Proton breakup experiments on the trion (bound state of the three-nucleon system) were studied with hopes that they would provide information on the trion ground state wavefunction, existence of resonances in the three-body system, and two nucleon scattering parameters. Table I shows some of the presently accepted properties of tritium. The S state is symmetric in all three coordinates while the S' state is antisymmetric under interchange of one pair. The probabilities of the states given in the table were calculated by Strayer and Sauer (S74). Because of the complexity of the four-body problem, no calculations have been performed using any exact formulation (such as that of Faddeev) and acceptable two-body potentials, although the equations are well known (Y67). Perhaps the most sophisticated calculations to date for knockout reactions on trions have been performed by Lehman (L72). Most groups analysing knockout or FSI data on trions have used the SIA (or modifications thereof) or Watson-Migdal theory (W52) respectively. The idea has been to simplify the four-body problem by choosing kinematic regions where one- or two-step processes for three bodies would dominate the reaction mechanism and the three-body cross section becomes strongly dependent on only one kinematic variable.

Van der Woude et al and Williams et al (Wo71) reported observing a T=1/2 resonance in ^{3}He using the ^{1}H(d, γ)^{3}He and ^{3}H(p,n) reactions. However, no supporting evidence for resonant or excited states in the three-nucleon system was

Table I

Properties of Tritium

Atomic mass	3.016050 u
Ground State spin,parity	$1/2^+$
Ground state isospin	1/2
Magnetic moment	2.9786
Binding energy	8.482 MeV
Half life	12.26 years
Decay energy	18.61 keV
Charge radius	1.70±.05 fm
Magnetic radius	1.70±.05 fm
Probability of S state	90 %
S'	1.5%
D	9 %

found by Bray et al (B71) using $^{6}Li(p,\alpha)$, or by Bunker et al (B72) using the $^{3}He(p,2p)$ reactions at 45 MeV. Since sequential decay of an excited trion is a process which would compete with $^{3}H(p,pn)$ QFS, it is important to know that this reaction has a negligible probability. The paper of Bray et al contains a summary of the experimental results to 1971.

The momentum distribution of the proton relative to the deuteron in ^{3}He has been extracted from experimental data by several groups using the SIA. Multiple scattering effects reduce the cross section from the SIA values. As the ingoing and outgoing relative energies rise, these effects become less important. One would expect the width to tend to the theoretical QFS value as the energy rises and multiple scatterings decrease in importance. The following table summarizes the results obtained thus far.

Table II

Previous Measurements of the n-d and p-d

Momentum Distribution for ^{3}H and ^{3}He

Experimenter	Energy (MeV)	Reaction	Flux Loss	Exp HWHM (MeV/c)	SIA HWHM (MeV/c)
Kitching	590	$^{3}He(p,pd)$	29%		52
et al (K72)	590	$^{3}He(p,2p)$	17		52
Frascaria	155	$^{3}He(p,2p)$	30	48	52
et al (F71)					
Cowley	100	$^{3}He(p,2p)$	54		52
et al (C72)	69	$^{3}He(p,2p)$	75		52
	69	$^{3}He(p,pd)$	75		52
Jain et al (J73)	46	$^{3}He(p,2p)$	54	45	52
Tin et al (T74)	46	$^{3}He(p,2p)$		48	52
	46	$^{3}H(p,pd)$	76	43	65
Slaus et al (S171)	35	$^{3}He(p,pd)$	71		52

The flux loss represents (1 - data/SIA), and the widths of the momentum distribution were obtained using an S-state trion wavefunction represented by an Irving-Gunn (G51) function overlapped with a Hulthen deuteron (H57) wavefunction. The widths are of the same order of magnitude as predicted by the uncertainty principle. All the (p,pd) experiments found shifts in the peak position from q=0 (where the SIA predicts the peak should be if the p (or n) and d are in a relative S state). Slaus suggested that this might be due to reaction mechanisms other than QFS (although he calculated that FSI could not account for all of the shift), or an influence of the D state component of the wavefunction (although the D state should have negligible effect near q=0 where it vanishes). It has been pointed out by Lehman (L72) that two other diagrams, antisymmetrization and neutron pickup, contribute significantly to these reactions and so the pole term alone should not be expected to explain the data.

Several experiments have investigated the ^{3}He(p,2p)d* reaction. The d* represents the unbound low energy singlet state of the n-p system with quantum numbers J=0 and T=1. The singlet interaction causes a quasistationary state (in particular a virtual state) to appear at 100 keV for the relative kinetic energy of a neutron and proton. At this energy, the two nucleons spend 200 times as much time within the range of the nuclear interaction than they would if no attraction were present (B69). In a summary by Jain et al (J73) it is reported

that the decomposition probability ratio (p+d)/(p+d*) was found to be 10 at 35 MeV (S171), 5.9 at 45 MeV (J73), and 4.5 at 155 MeV (F71). Frascaria et al (F71) studied the effect of various wavefunctions for the trion and demonstrated that the Irving-Gunn function is superior to the Irving or Gaussian wavefunctions (I51). This agrees with the results of the Griffy and Oakes study (G64) of electron scattering data. Lehman (L72) has suggested that the asymptotic form alone of the Irving-Gunn wavefunction is responsible for contributing the correct propagator for $^3He \rightarrow p+d$ if the vertex amplitude for this virtual decomposition is assumed to be a slowly varying function of q. He noted that the Irving and Gaussian wavefunctions do not have this characteristic.

Few knockout experiments have used ^3H as a target, mostly because of radioactivity hazards. Fritts and Parker (F72) studied the $^3H(p,2p)nn$ reaction at 20 MeV, but they were primarily interested in extracting the n-n scattering length. Slaus et al (S73) studied various ^3He + ^3H reactions and determined that other mechanisms beside QFS play an important role in breakup reactions. Tin (T74) studied the $^3H(p,pd)n$ and $^3H(p,2p)nn$ reactions at 46 MeV.

Although (p,2p) and (p,pn) reactions are quite similar theoretically, the vast majority of experimenters have chosen to measure (p,2p) cross sections. Working with neutrons involved certain difficulties, notably low and uncertain detection efficiency, sensitivity to background radiation, and increased experimental complexity compared to charged particle

experiments. Some of these problems remain, but certain technological advances, to be described later, have now made neutron experiments easier than a decade ago. In some respects (p,pn) experiments are superior to (p,2p) experiments because low energy neutrons are easier to detect than low energy charged particles. Also, there is less spectrum contamination due to detection of protons elastically scattered from the target than occurs in (p,2p) experiments. Because the two detected particles are different for (p,pn), there is no requirement from the Pauli principle that the angular correlation of the cross section should be symmetric in the two angles, although this symmetry is useful in checking the consistency of (p,2p) data. Neutrons are almost always detected using time-of-flight (TOF) techniques, because neutrons of a precise energy do not deposit a unique energy in a detector unless the detector is very large in size.

Two types of (p,pn) experiments have been performed. In the first (C69), the proton and neutron are detected in the same direction and the reaction is interpreted as (p,d*) using PWBA theory. In the second type, which is used in this thesis, the neutron and proton are detected on opposite sides of the beam and the d*, if produced, is the residual particle.

Petersen et al (P69) have studied the D(p,pn) knockout reaction, while Valkovic et al (V71) have investigated the D(p,pn) and D(d,pn) knockout reactions. In (P69) it was reported that the (p,pn) cross sections were larger than equivalent (p,2p) data, although there was considerable rescat-

tering below 50 MeV. Also, there is a variation in cross section with p-n scattering angle that did not manifest itself in (p,2p) reactions. Both these effects have also been observed for (p,2p) and (p,pn) knockout reactions on ^{6}Li (M72,M74a). A number of ^{2}H(p,pn) experiments (see (K74) for example) have also been performed which studied final state interactions.

Section 1.3 Attenuation Model

As discussed above, the standard analysis of knockout data has used the SIA. This reaction model suffers from some serious deficiencies, notably 1) violation of unitarity, 2) indeterminacy of the appropriate 3-4 cross section due to off-the-energy-shell effects, 3) neglect of higher order terms in the scattering series, and 4) neglect of the Pauli principle.

The Faddeev equations provide an "exact" route for calculating knockout amplitudes and have been successfully applied to the breakup of deuterium using local (K73) and nonlocal (A66) potentials. It should be realized that these potentials are simplified forms not capable of fitting the two-body data as well as the Reid potential (R68), for example. However, four-body systems are perhaps beyond present computational abilities. These difficulties become more insurmountable with increasingly massive cores (spectators) so that approximations are necessary.

Several techniques have been developed in an attempt to avoid complete rejection of the impulse approximation, while still accounting for the infinite number of multiple scattering terms omitted by the approximation. The distorted-wave impulse approximation (DWIA) transfers flux from the breakup channel to the elastic channel, by replacing the ingoing and outgoing plane waves with waves that are distorted by interaction with the target as a whole. DWIA calculations have had some success at medium energies (155 MeV) for ^{3}He (F71) and at 45 MeV for

heavier targets (M74), but it is improbable that the DWIA would perform well on tritium at 45 MeV. The appropriate optical potentials would be difficult to obtain, and also all present DWIA codes contain approximations related to the mass of the spectator (with results deteriorating for lighter spectators). Some groups (S69) have attempted to calculate the multiple scattering expansion perturbatively, but the series seems to converge slowly.

Another method of simulating the multiple scattering corrections has been to modify the wavefunction $\Phi(\vec{r})$ (or its Fourier transform $\phi(\vec{q})$) of the knocked-out particle. Green and Brown (G60) applied the radius cutoff method of Butler (B57) to the analysis of QFS using the impulse approximation. A radial cutoff is introduced into the overlap integral

$$\Phi(\vec{r}) = \int_{rcut}^{\infty} \int_{4\pi} \Psi_{target}(\vec{r},\vec{r}') \, \Gamma_{spect}(\vec{r}') \, d\vec{r}'$$

$$\phi(\vec{q}) = \int_{all\ space} e^{i\vec{q}\cdot\vec{r}} \, \Phi(\vec{r}) \, d\vec{r}$$

where Ψ_{target} is the wavefunction of the knocked-out particle and spectator in the target and Γ_{spect} is the internal wavefunction of the spectator. If the knocked-out particle is closer than rcut to the spectator, no contribution to QFS occurs. This has the effect of narrowing the momentum distribution of $\phi(q)$, since removal of components at small radii corresponds to removal of components with large momentum. The need for this narrowing of the momentum distribution is evident from Table II. This model emphasizes the peripheral nature and surface localization (F62) of quasi-free processes

(that is, only the asymptotic part of the wavefunction is important). Some theoretical justification from the Faddeev equations for this process has been given by Cahill (C74). No direct account is taken of the projectile-spectator interaction.

The attenuation model of Rogers and Saylor (R72), later modified by Lim (L73), seeks to alter the SIA by multiplying the SIA cross section by two transmission factors, T_{3s} and T_{4s}, which account for the scattering of particles 3 and 4 in the final state with the spectator 5.

$$\frac{d^3\sigma}{d\Omega_3\, d\Omega_4\, dE_3} = T_{3s}(E_{3s}) \left(\frac{d^3\sigma}{d\Omega_3\, d\Omega_4\, dE_3}\right)_{SIA} T_{4s}(E_{4s})$$

T_{is} represents the probability that particle i will not interact with the spectator.

$$T_{is} = \int_{\text{all space}} \psi^*_{is}(\vec{r})\, \tau_{is}(\vec{r}, E_{is})\, \psi_{is}(\vec{r})\, d\vec{r}$$

τ_{is} is an operator involving the total cross section for particle i and 5, ψ_{is} is the relative cluster wavefunction of i and the spectator, and E_{is} is the final state relative energy of particles i and 5. Final state energies are used because the interference with QFS is assumed to occur after the QFS event. However, Lehman (L72) suggests that much of the attenuation is due to initial state scattering of the projectile with the target as a whole. The deBroglie wavelength of a 45 MeV incident proton is .67 fm, while the wavelength of a 5 MeV outgoing proton is 2 fm. It is clear that there is a greater probability for an outgoing nucleon to interact with

both the neutron and deuteron than for the projectile to interact with both particles, whose most probable distance apart in the target is 3 fm (at the peak of the exponential wavefunction in F71). Shapiro has noted (Sh68) that q must be less than K (where $K^2/2m$ is the n-d binding energy of the trion and m is the n-d reduced mass) for the pole approximation to be valid. K is 88.5 MeV/c for the trion. Several forms have been proposed (L73) for τ_{is}:

$$\tau_{is} = \begin{cases} = 1 - \sigma(E_{is})/4\pi r^2 \\ = e^{-\sigma(E_{is})/4\pi r^2} \text{ (used in this paper)} \\ = \tfrac{1}{2}\left[1 + (1 - \sigma(E_{is})/4\pi r^2)^{1/2}\right] \end{cases} \Big\} 4\pi r^2 > \sigma(E_{is})$$

$$= 0 \quad \text{otherwise}$$

The philosophy behind these forms is that a contribution to QFS is most likely when particle i is far away from the spectator. As the two move closer together, the contribution decreases and abruptly drops to zero at a certain radius. This bears some resemblance to the cutoff model, but provides a procedure for estimating the cutoff radius that is energy dependent (Table II shows that the narrowing of the QFS peak and decrease in peak height is energy dependent). However, it is obvious that considerably more nuclear information (mostly contained in the total cross section) is put into this calculation. The $\phi(q)$ generated using a sharp cutoff has the regrettable characteristic of "ringing" (oscillating), but the effective momentum distribution created by the attenuation model does not have this disadvantage.

It should be noted that this model approximates second and

higher order scattering with the spectator, but neglects scattering between particles 3 and 4 after interactions with particle 5. It is expected that these contributions will be randomly distributed over all available phase space. Also, it overestimates the attenuation, since although QFS events will be lost if either particle 3 or particle 4 interacts with the spectator, if both 3 and 4 interact with the spectator, the cross section should not be reduced further. To correct for this effect, Lim suggests (L73) that total cross sections reduced in magnitude from the experimental values be used in calculating the T's.

Section 1.4 Objectives and Philosophy

The present experiment studied the $^3H(p,pn)d$, $^3H(p,dn)p$, and $^3H(p,pn)d^*$ reactions. It is possible to create the d* only if kinematic conditions allow low n-p relative energy to be obtained. The reaction geometry is shown in Figure 1.4.1. One of the objects of the experiment is to study the correlations between the nucleons in tritium. One such correlation can create a cluster of the neutron and proton to form a "deuteron" (S=1) (although this cluster may not have exactly the same properties as a free deuteron), or a "singlet deuteron" (S=0). Although it would be expected that the deuteron would not make a very good cluster because of its low binding energy, the results to be described here show that the model assuming its existence within the nucleus performs surprisingly well.

One would like to determine the probabilities of forming these two clusters and measure their momentum distributions relative to the remaining neutron. These factors can currently be extracted from the data only if some particular reaction mechanism such as quasi-free scattering is assumed. The reaction mechanism is tested by comparing the extracted results with those predicted by a theory based on the reaction mechanism. If agreement is good, the mechanism and wavefunctions used should be reliable. The experiment was performed at approximately 45.5 MeV in order to compare the results with a study of the $^3H(p,2p)nn$, $^3He(p,2p)d$, and $^3He(p,pd)p$ reactions (T74) performed at the same energy. The data were recorded for coplanar geometries at a variety of symmetric and asymmetric

angle pairs. The convention will be adopted that whenever an angle pair is specified, the charged particle (proton or deuteron) angle will be listed first and the neutron angle will be given second.

We adopt the following philosophy for analysing the experimental cross sections. Using previously determined information such as electron scattering data, we will choose the best theoretical wavefunctions and parameters for use in the framework of the SIA and attenuation model. The predictions of both the SIA and attenuation model will be compared with the data obtained in this experiment. Instead of extracting momentum distributions from the data assuming the off-the-energy-shell cross sections to be correct (or vice versa), the predictions of the models as a whole will be compared with the cross sections themselves. This should result in less ambiguity about the origins of any conclusions.

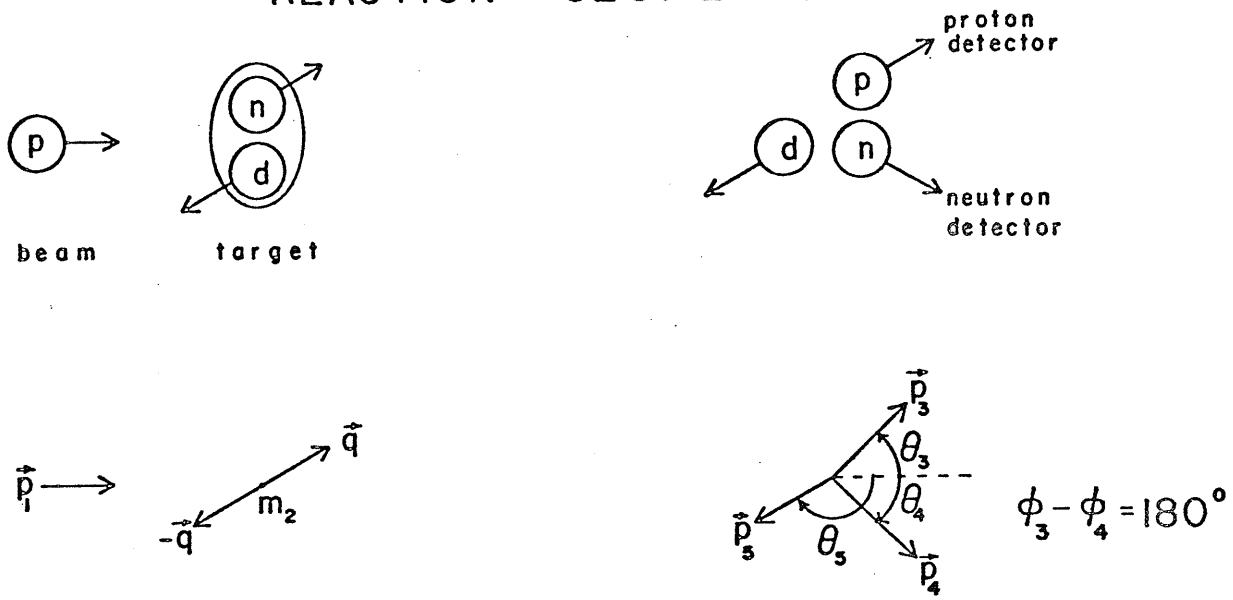

Figure 1.4.1 Reaction Geometry

The convention will be adopted that the reaction is 2(1,34)5 Particle 3 is always charged and particle 4 is a neutron.

Chapter 2

THE EXPERIMENT

Section 2.1 The Target

The target consisted of .27 mg/cm² of tritium absorbed in 11.7 mg/cm² of scandium and deposited on a backing of 5 mg/cm² of aluminum. The active area was a circle .5 inches in diameter. It was constructed at Oak Ridge National Laboratories especially for this experiment and was the first of this composition ever prepared at that laboratory (and perhaps anywhere in the world, at present). The conventional tritiated target configuration is tritium in titanium deposited on gold or copper, but such a design was undesirable because of fears that Coulomb scattering from the high Z gold or copper would cause several percent of the beam to be lost during transport between the scattering chamber and a distant beam dump. Scandium and aluminum were specified because their large negative Q-values for (p,pn) reactions of -11.32 and -13.06 MeV respectively usually place (p,pn) events from these nuclei outside the regions of kinematic interest. Also, they are monoisotopic and thus only one (p,pn) locus for each element need be considered when studying background effects. Oak Ridge believed that a tritium-to-scandium ratio of 2:1 was probable for the finished target yielding a tritium density of 1.3 mg/cm², but the final target contained substantially less tritium. A "dummy" target of similar composition but without any tritium was also constructed. The dummy target allowed

subtraction of events due to the scandium or aluminum. Figure 2.1.1 shows spectra of protons scattered from the tritiated and dummy targets when they were both exposed to the same number of protons. It appears that the thicknesses of the scandium and aluminum in the two targets are equivalent to within 10%. The peaks labelled epsilon and delta are due to saturation of some amplifiers upon receipt of signals from heavily ionizing particles.

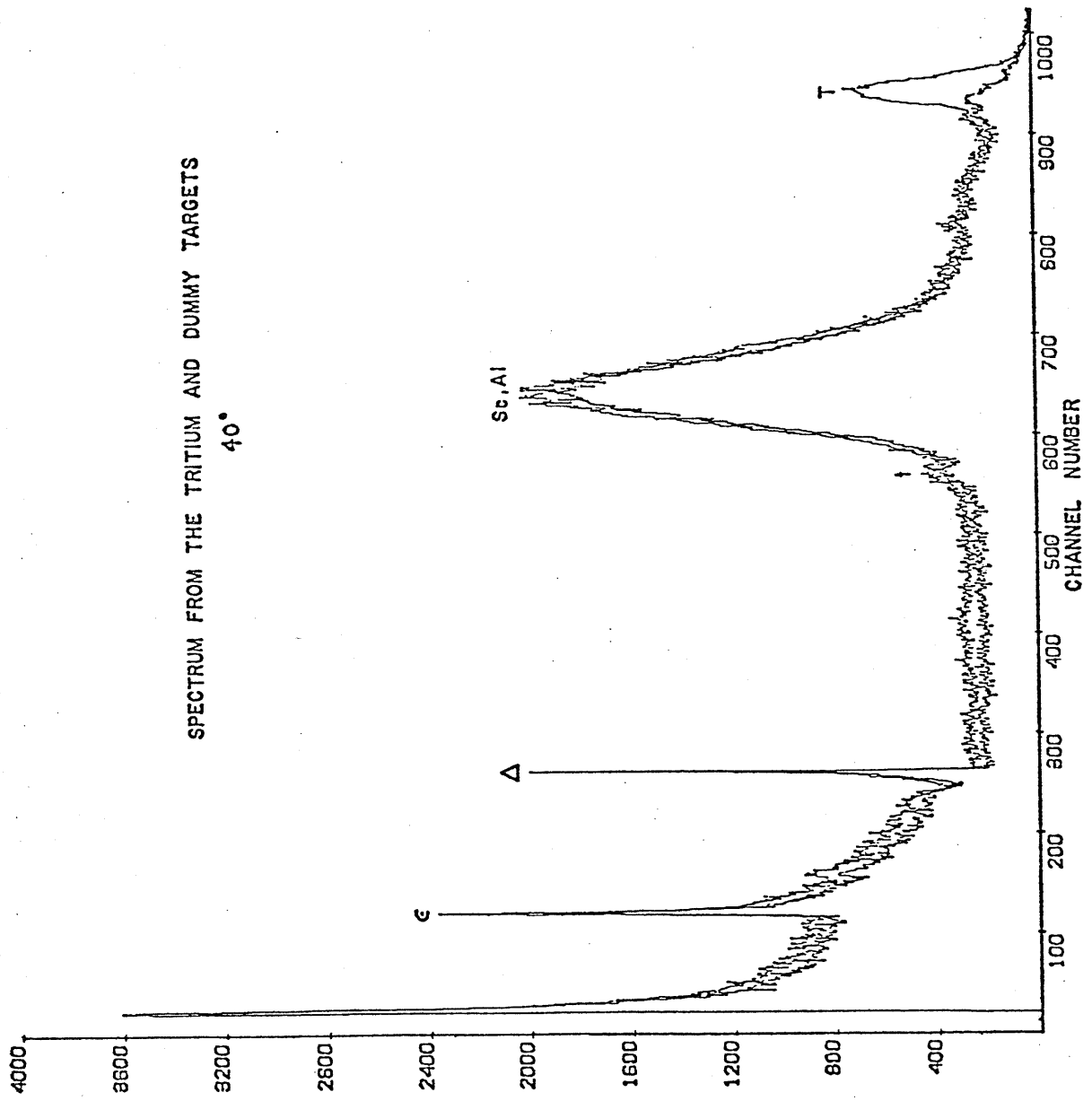

Figure 2.1.1 Spectra from the tritiated (upper curve) and dummy (lower) targets when exposed to the same beam charge. Peaks ϵ and Δ result from saturation of amplifiers, t from recoil tritons, Sc,Al from "folded-back" protons scattered from Sc and Al, and T protons scattered from tritium.

Section 2.2 Equipment

The experiment was performed on the 15° left beamline at the University of Manitoba using its 42 inch sector-focused cyclotron. A plan view of the cyclotron area is shown in Figure 2.2.1. The 15° bend in the switching magnet allowed little momentum analysis to be performed, so that of 300 na of 45 MeV raw beam having an energy spread of 2 MeV, approximately 15 na of 300 keV wide beam was selected. The energy of the proton beam was determined by a time-of-flight (TOF) technique. It measured the difference, delta T, in time of arrival at a position "A" in Figure 2.2.1 of gamma rays created at two successive screen positions in the 15° left beamline upon bombardment by the beam. The screen positions are labelled S1 and S2 in Figure 2.2.1. The cyclotron RF frequency was divided by two and used as a time reference. A typical spectrum is shown in Figure 2.2.2. The energies used for the experiment during the three runs that were performed were 45.4, 45.3, and 46.5 MeV. The beam spot on the target was never larger than 1/8 inch wide by 3/8 inch high. It is desirable to have a small beam spot size in order to define more accurately the scattering angles. However, a large beam spot is beneficial for dissipating heat produced in the target and for more efficient utilization of the active area of the target. In order to decrease background radiation, all slits and the first quadrupole doublet magnet were located behind a concrete shielding wall and the Faraday cup beam dump was buried in the earth beyond the experimental room. Because of the long

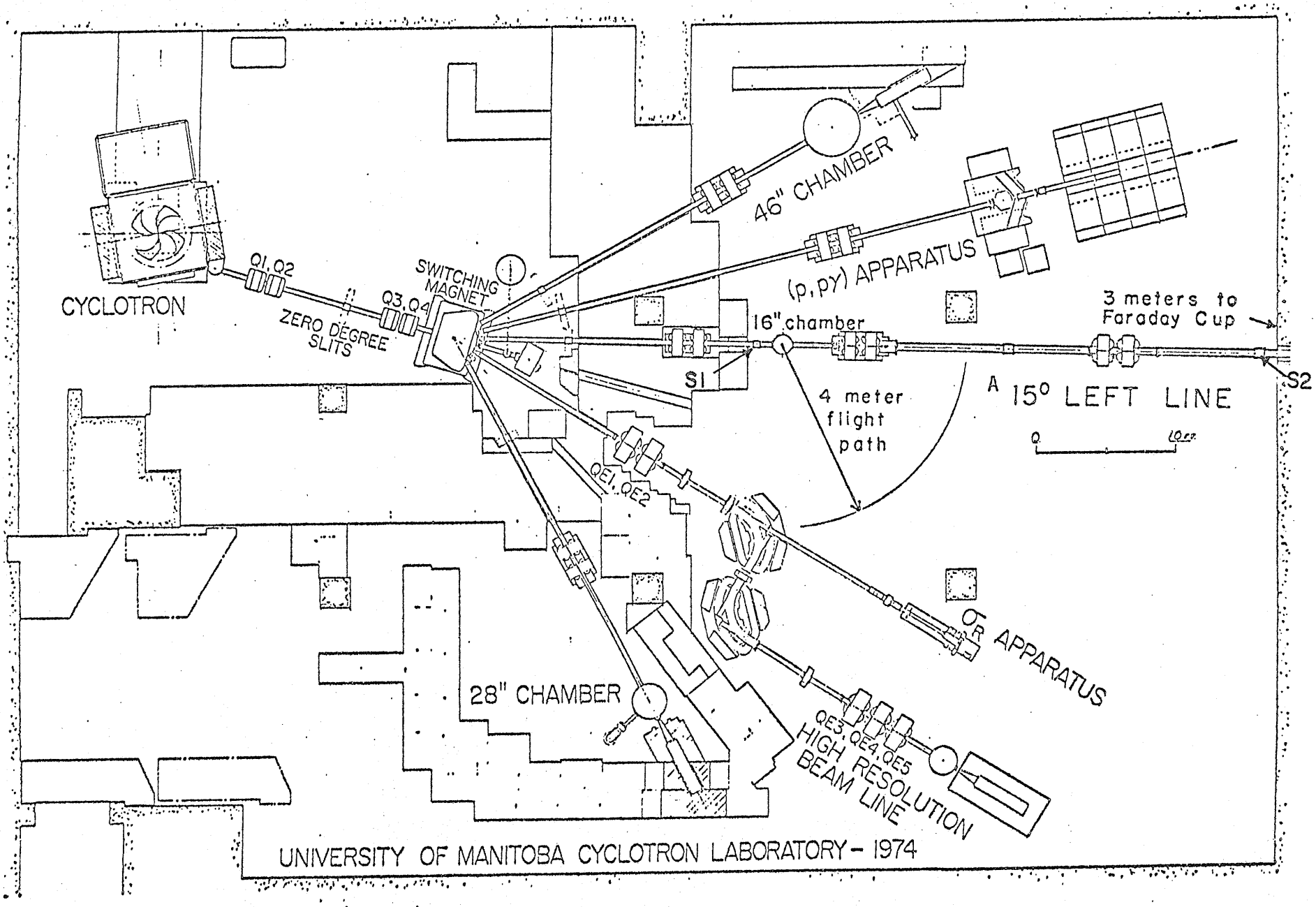

Figure 2.2.1 The Cyclotron Area. The experiment was performed on the 15° left beamline. S1 and S2 represent screen positions. "A" is the position of a beam monitor. The Faraday Cup is buried 3 m outside the wall.

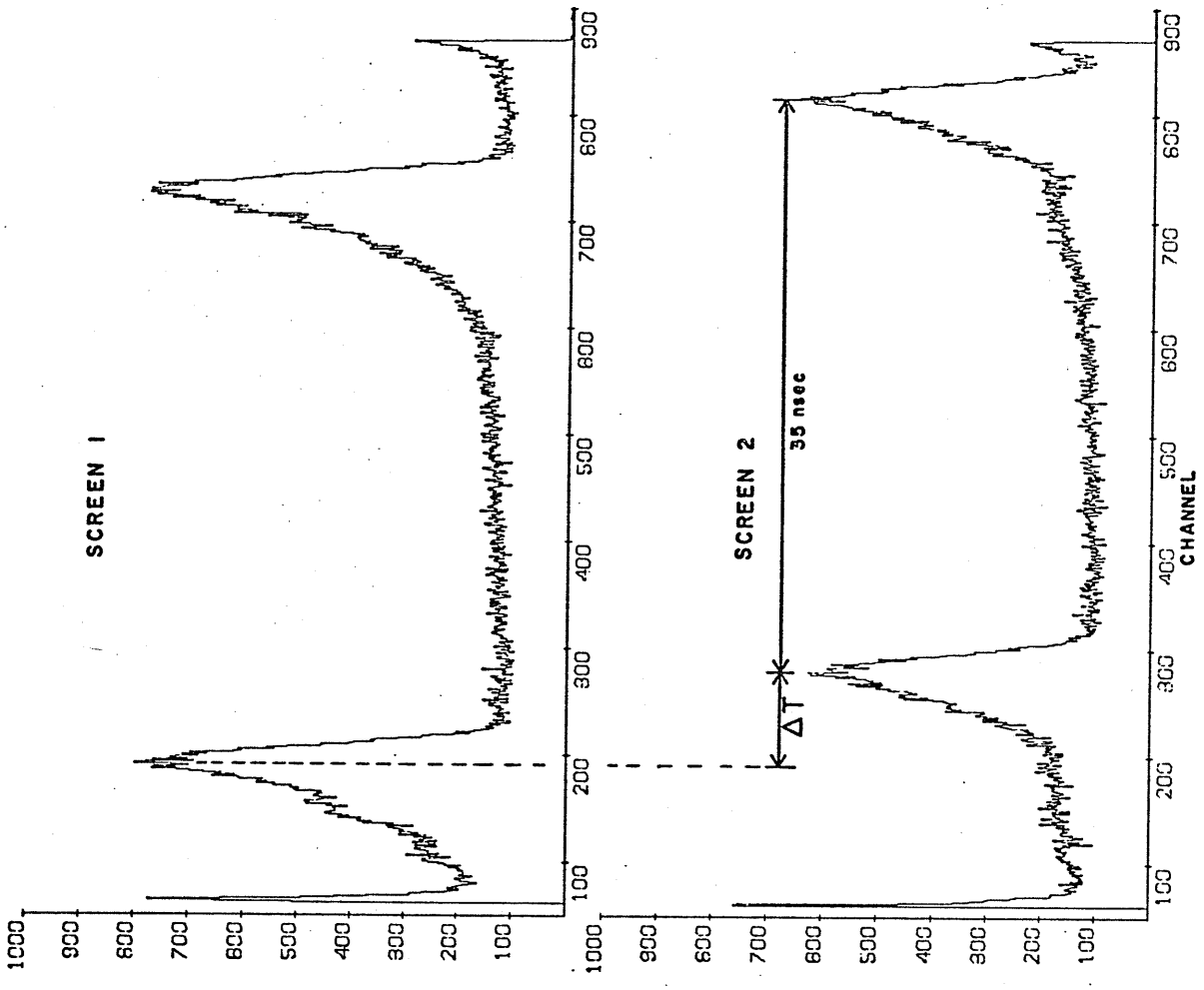

Figure 2.2.2 Beam Energy Determination
Time-of-flight spectra for γ rays produced at screen 1 (S1) and screen 2 (S2). The difference ΔT in time of arrival at the detector yields the beam energy.

distance that the beam must be transported from the scattering chamber to the Faraday cup, a quadrupole doublet was necessary downstream from the chamber. This was located close to the chamber in order to collect those protons Coulomb scattered in the target (it is estimated that less than .3% of the beam was lost). All of the beampipe downstream from this doublet was 6 inches in diameter to allow maximum transmission. The TOF beam energy determination spectra did not usually show any peaks due to collisions with the pipe.

A 16 inch low mass scattering chamber shown in Figure 2.2.3 had been constructed especially for neutron physics experiments. It has thin aluminum walls and a steel roof and floor, the principle of design being that a low mass would reduce neutron "inscattering" from the chamber walls to the neutron detector. The chamber contains a movable detector arm with an attached liquid nitrogen reservoir and filling connection. Angles may be set to an accuracy of .2° (barring systematic errors). A four position target ladder (Figure 2.2.4) was inserted through the floor of the chamber and contained the tritium and dummy targets, as well as a scintillator screen used for beam profile viewing and a deuterated polyethylene (CD_2) target for proton energy calibrations.

The side of the chamber has a 2 inch gap covered with Kapton-H foil which allowed easy escape of protons from p-d scattering for alignment of the signals in the coincidence system. Whenever the tritiated target was inside the chamber, the Kapton was supported by an aluminum ring. This ring formed

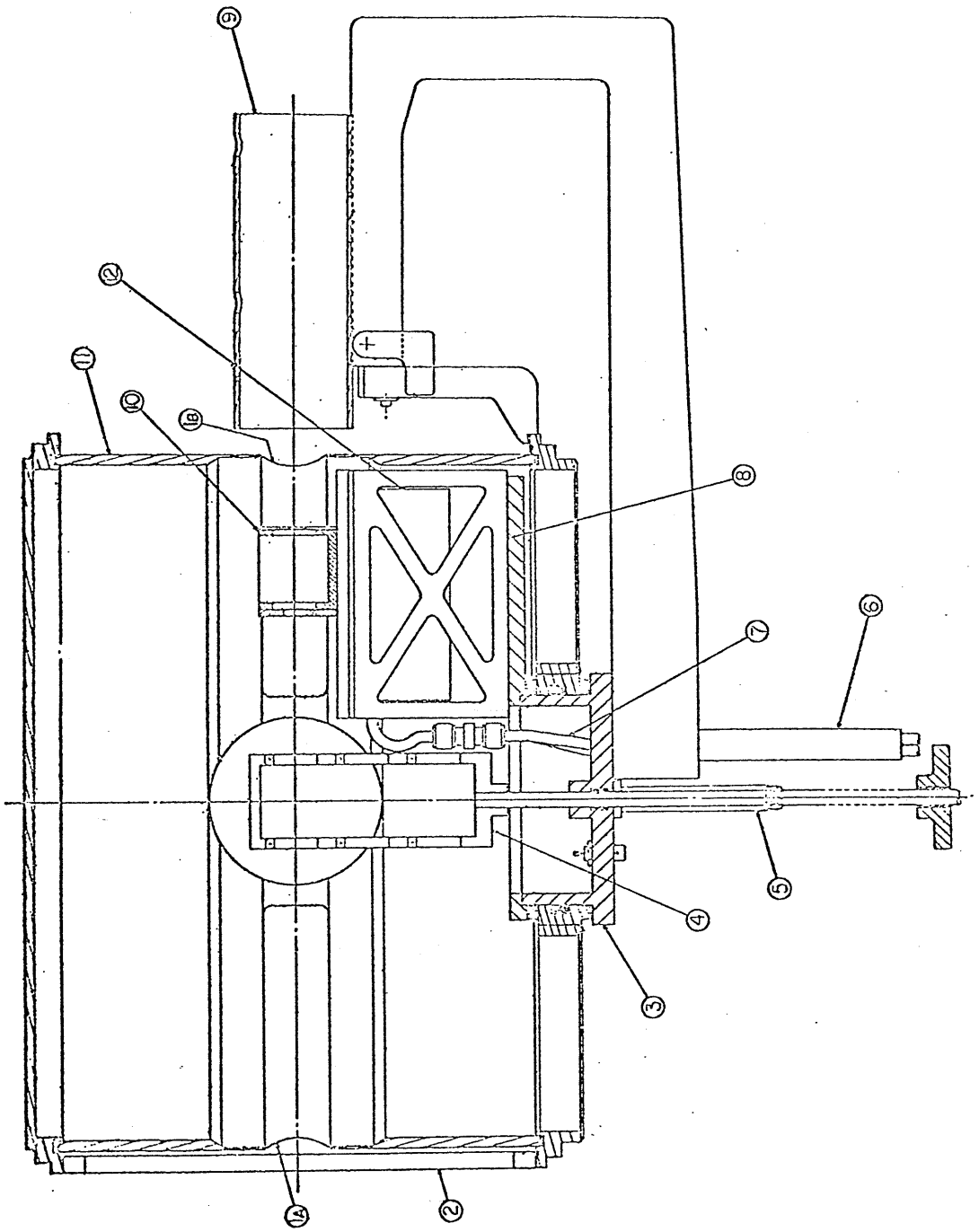

Fig. 2.2.3 A cross section of the 16 inch scattering chamber used for the (p,pn) measurements. The labelled components are as follows:
1. "Kapton-H" foil of thicknesses a) .005 inches b) .003 inches.
2. Moveable pillars 3. Rotating hub for detector platform.
4. Target ladder 5. Target ladder clamp 6. Stainless steel standoff for cooling lines 7. Cooling lines 8. Nylon support for detector platform 9. Mount for NaI(Tl) detector assembly
10. Solid state detector cube 11. Aluminum wall of chamber
12. Liquid nitrogen reservoir

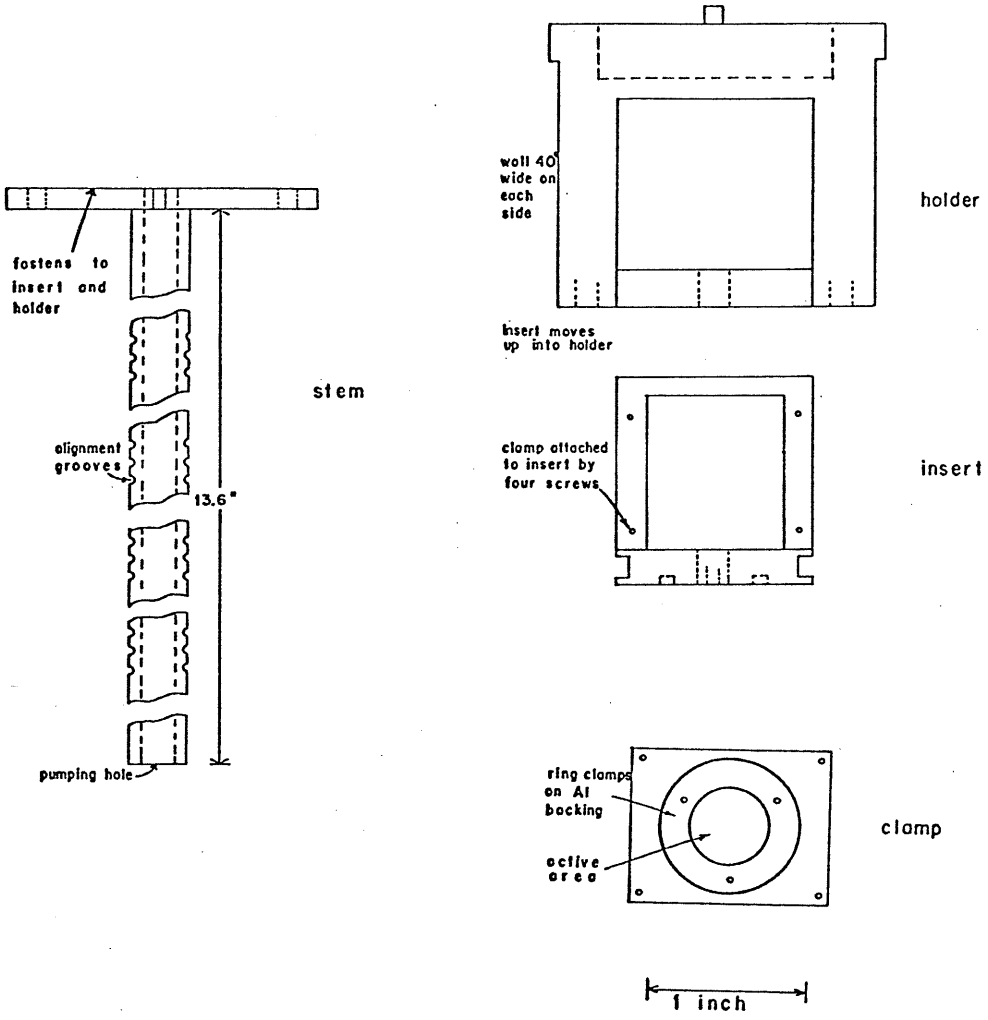

Figure 2.2.4 Components of the Tritium Target Cell

The target cell is of modular construction. The target was attached to an insert using a clamp. The insert was stationed inside a holder with a 320° Kapton wall. The holder was positioned on top of a stem through which pumping occurred.

a rupture shield which took the strain from the Kapton under vacuum, thereby decreasing the probability of a rupture, and shielding the interior of the chamber should an implosion actually occur. However, with the ring in place, it was necessary for neutrons produced by (p,pn) or (p,dn) reactions on tritium to pass through the structure and the observed flux was consequently diminished somewhat.

The tritium target was contained in a cell (Figure 2.2.4) consisting of a 2 inch diameter aluminum cylinder with a .001 inch Kapton wall and an attached steel stem through which the cell could be pumped. A mechanical pump dedicated to radioactive exhaust evacuated the cell through a molecular sieve and was vented to an exhaust line leading to a parking lot above the laboratory. The Kapton served to isolate the tritiated target from the chamber and protect it from accident and pump oil. The cell had been tested before installation of the target to ensure that it was capable of withstanding appropriate positive and negative pressures. The cell for the dummy target was of similar design except that its interior was not entirely isolated from the chamber. Thus evacuation of the dummy target cell occurred during pump-down of the chamber. Space limitations in the chamber required that the diameter of the target cells be small and this in turn dictated careful consideration of angles, beam widths, and slit positions. Figure 2.2.5 shows the layout of the detectors and slits. The detectors were housed inside a brass cube which shielded them from stray radiation. The antiscattering baffle, used to

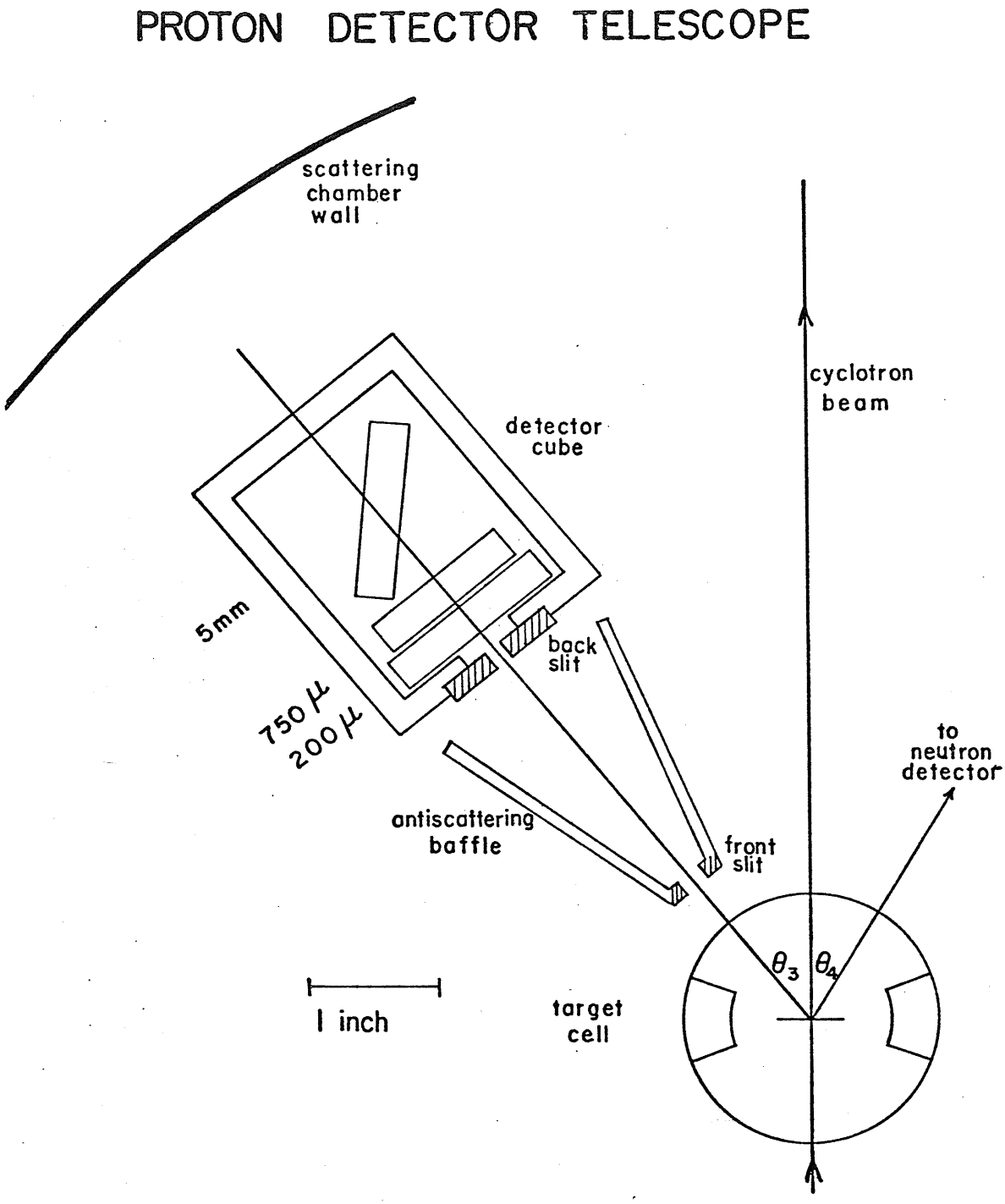

Figure 2.2.5 Detectors and slits for charged particles

eliminate detection of particles originating in the Kapton windows upon bombardment by the beam, was as close to the cell as possible. This forward slit consisted of a 1/8 inch thick tantalum front piece with a 3/16 by 3/8 inch aperture and nickel side pieces constructed so that small detector angles could be reached. The primary slit (which alone determined the solid angle) was fastened to the detector cube and consisted of .158 inch thick nickel with a .157 by .314 inch aperture. At a radius of 3.875 inches, this created an angular acceptance of 2.3° horizontally by 4.6° vertically.

The proton telescope consisted of three silicon detectors. The first, called "EPSILON", closest to the target, was a 200 μm surface barrier detector which allowed particle identification of protons down to 5 MeV. The second detector was a 750 μm surface barrier detector, named "DELTA", which provided timing and energy information. This was the detector which most sensitively affected the performance of the system and was protected from pump oil and low energy particles by EPSILON. The third detector was a 5 mm Si(Li) detector called "E", which provided the bulk of the energy signal for higher energy particles. During the last two runs this detector was canted at an angle of 45° to increase the effective thickness of the detector stack to 8 mm of silicon, sufficient to stop 40 MeV protons. The three detectors were electrically isolated from one another in an effort to reduce ground loop and noise problems. The EPSILON and E detectors were 200 mm^2 in area, but DELTA was 100 mm^2 (and was smaller in area in order to

obtain better timing properties, as will be demonstrated in a later section). Surface barrier detectors are generally superior to Si(Li) detectors because they have smaller dead layers and are more resistant to neutron damage. However, thick surface barrier detectors are prohibitively expensive. A permanent magnet of strength 500 G was mounted on the nickel antiscattering slits to deflect delta rays produced in the target and protect the detectors.

The neutron detector consisted of two liquid scintillators, one above and one below the median plane each having its own phototube. The scintillators were cylinders containing the pure liquid hydrocarbon NE213[1] 4.5 inches in diameter by 5 inches long with the interior painted with isotropically reflecting paint. They were coupled to 4.5 inch diameter RCA 4522 photomultipliers. The scintillators emit light in a spectrum which peaks at 425 nm and the phototubes have bialkali photocathodes most sensitive at 400 nm. NE213 has a hydrogen to carbon ratio of 1.2:1 and the larger this factor, the better the capability for rejection of gamma ray events. Typically, the ratio of gamma ray to neutron counting rates for this experiment was one or two, so that it was necessary to discriminate against this background. The phototubes were designed for high sensitivity, low dark current, fast timing applications (using an in-line focused structure and strong fields to reduce transit time spread) with anode risetimes of 3

---

[1] Nuclear Enterprises, Inc., 935 Terminal Way, San Carlos, Ca 94070 USA

nsec and quantum efficiencies near 30%. The tubes were operated at approximately -1800 volts, negative high voltage being used to simplify interfacing with the discriminators. This required that the scintillators also be placed at high voltage to prevent poisoning of the photocathodes. The scintillators were positioned approximately 4 meters from the target creating an angular acceptance of less than 1.6° horizontally by 3.2° vertically.

Section 2.3 Electronics

A very simplified diagram of the electronics is shown in Figure 2.3.1. An event began with the detection of a charged particle. A discriminator signalled such an occurrence if the charge produced in the DELTA detector developed sufficient voltage to exceed a set threshold. After a certain delay, two time windows were created, the first being used to accept random events and the second receiving real events. During each window, the system could accept a phototube trigger. This was produced if a phototube generated sufficient current to trigger another discriminator. When such a coincidence occurred between the two discriminator signals, a time-to-amplitude converter (TAC) was started, measuring the time-of-flight (TOF) of the neutron. If the pulse height of the phototube signal exceeded the threshold on a single channel analyser (SCA), the event was considered a good one, causing the linear signals to be digitized and the flags gated into the computer. A complete schematic of the circuit is shown in Figure 2.3.2. The coincidence timing was aligned using elastically scattered protons from deuterium to provide signals in coincidence in the charged particle and neutron detectors. Deuterons were detected with the charged particle detectors and the protons were detected in the scintillators. The scintillators were brought within a few feet of the scattering chamber in order to reduce energy loss in the air. Figure 2.3.3 shows the type of coincidence spectrum obtained.

Each of the semiconductor detectors had its own charge

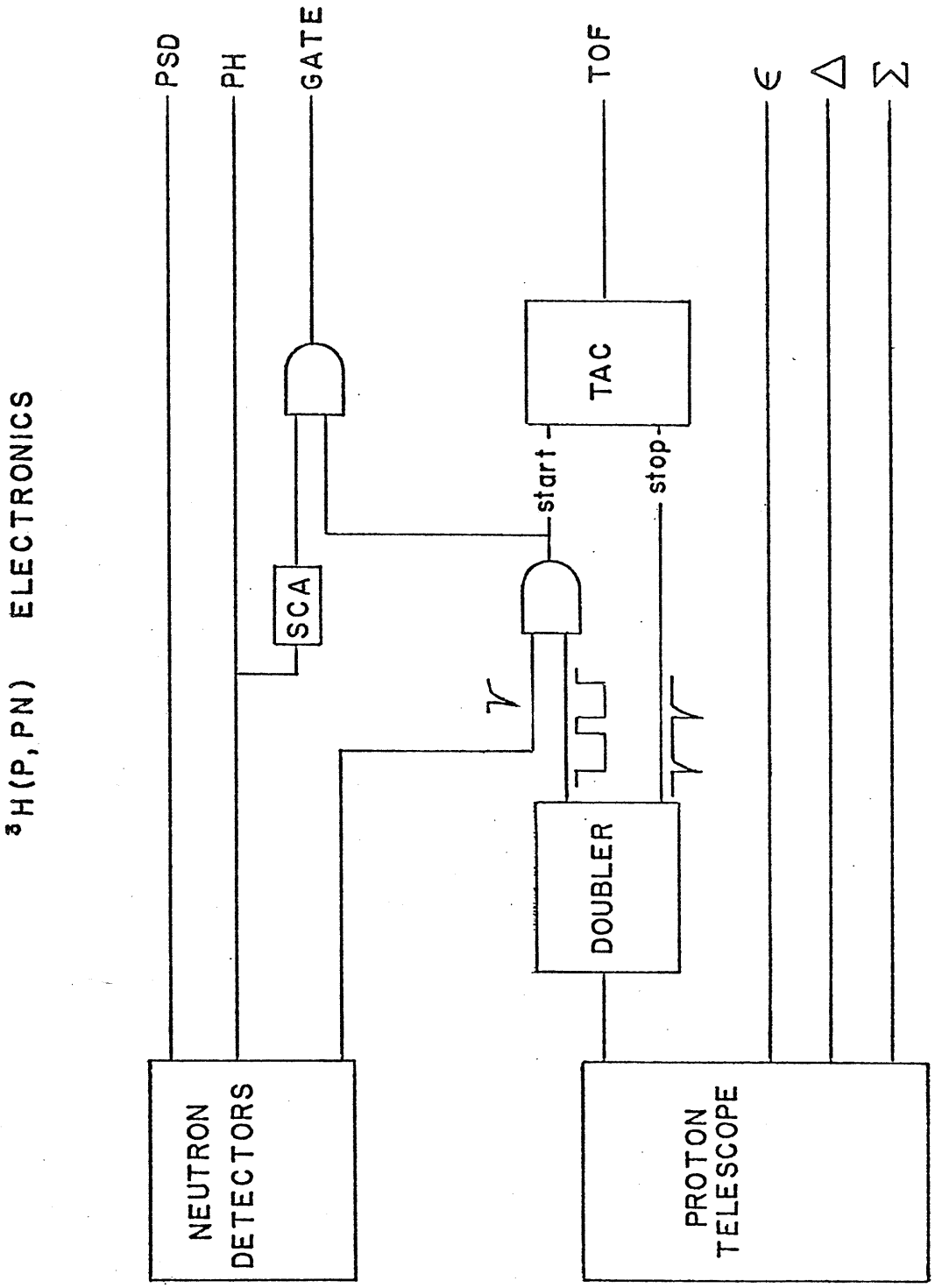

Figure 2.3.1 Simplified Electronics Diagram

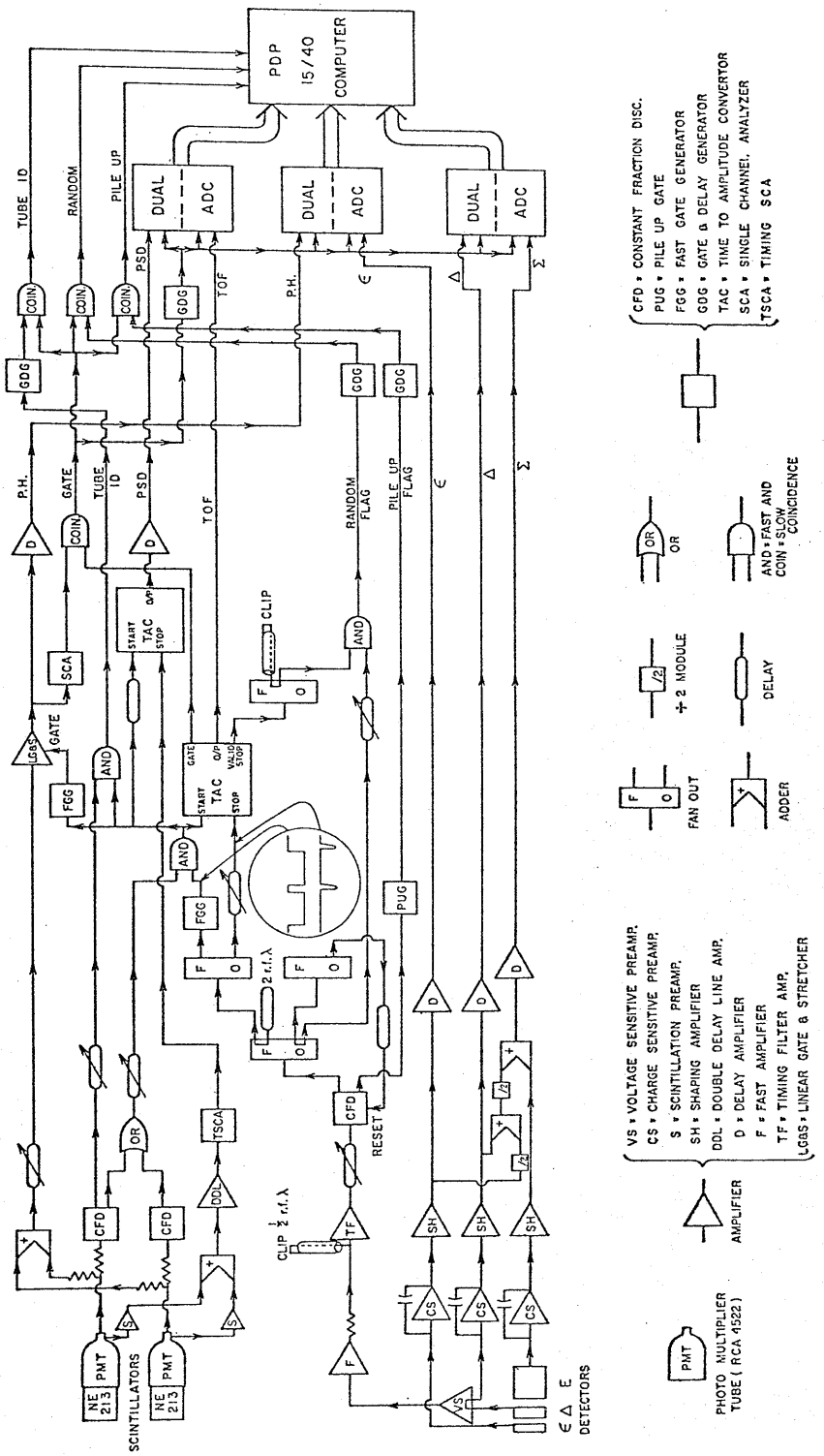

Figure 2.3.2 Complete Electronics Diagram

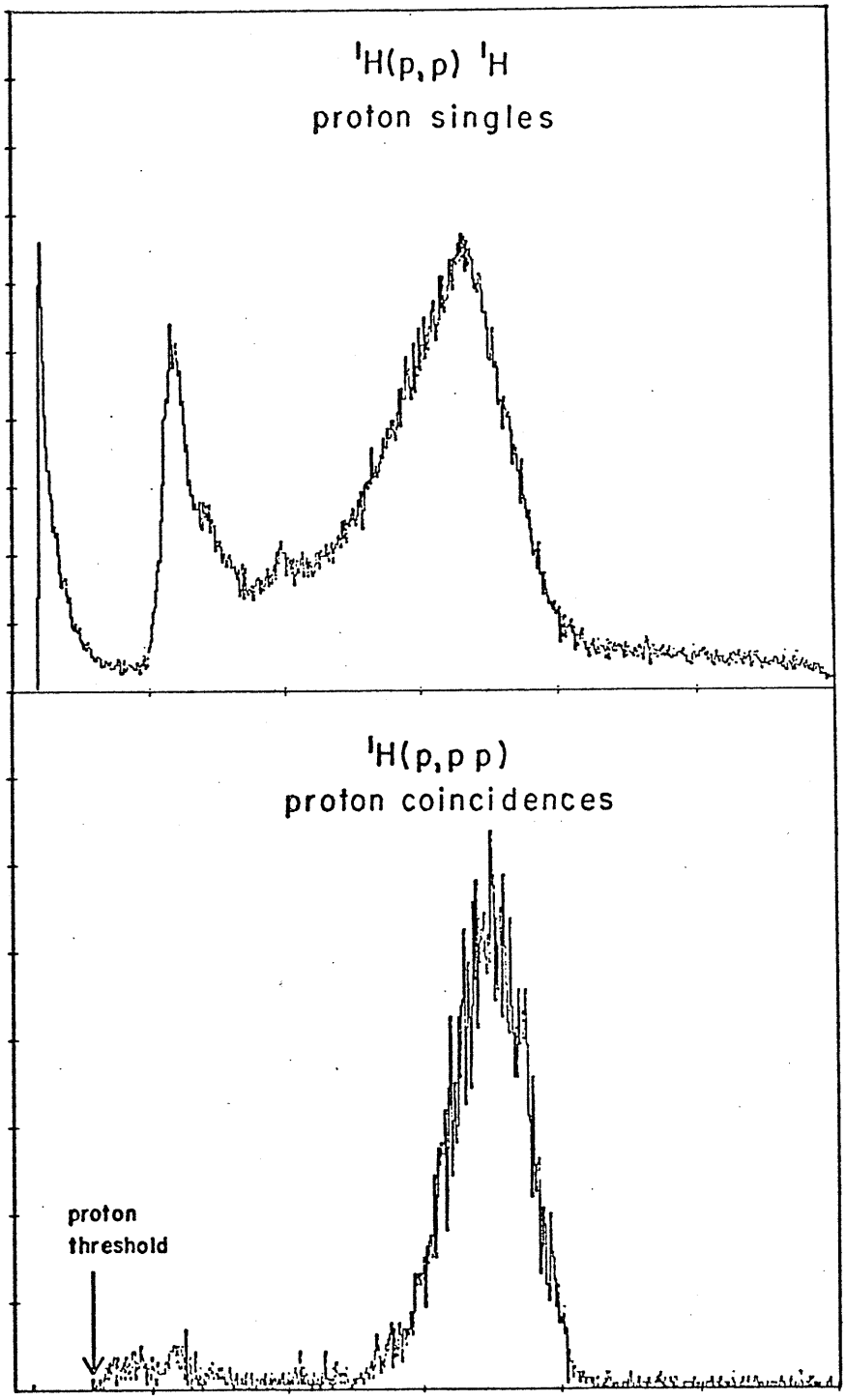

Figure 2.3.3 Coincidence Alignment

Protons are detected in coincidence by the proton and neutron detectors.

sensitive preamplifier located close to the scattering chamber. These fed 1 usec shaping amplifiers with gains set in a 4:2:1 ratio for EPSILON, DELTA, and E so that the deuteron peaks were always nonsaturating. The amplifier outputs were then divided by the above factors and added to obtain a linear summed energy signal called "SIGMA". The gains were matched as follows. The EPSILON amplifier gain was adjusted so that the peak from a 5.5 MeV ^{241}Am alpha source fell in a predetermined channel in a computer display of SIGMA. A pulser was inserted into the EPSILON charge-sensitive amplifier and the pulser's voltage was adjusted until the peak from it fell in the same channel as the alphas. Then the same signal was inserted into the DELTA and E preamps and their amplifier gains were adjusted so that the pulser peaks all fell in the same channel. This magnification of the EPSILON and DELTA signals made particle identification easier.

The DELTA detector provided the signal to start the timing system for the measurement of the neutron TOF. An inductor was placed between this detector and its charge sensitive amplifier with a fast preamplifier sensing the voltage across the inductor and passing the amplified signal outside the chamber to a pair of fast shaping amplifiers. Between these two amplifiers was a clipping stub one half of a cyclotron RF period long which attenuated the RF noise on the signal by a factor of six, but did not affect the timing information in the leading edge of the pulse. The stub was back-terminated but caused severe distortion of the remainder of the pulse. The

second amplifier was a timing filter amplifier with a 10 nsec differentiating time constant. The signal was delayed and presented to a constant-fraction-of-pulse-height discriminator (CFD), but because of the aforementioned distortion it was necessary to operate it in external reset mode, with the reset occurring 200 nsec after the trigger to prevent multiple firing on the complex waveform.

The CFD and fanouts following it supplied pulses for resetting the CFD, triggering the pile-up unit (with resolving time 3 μsec), generating a random flag, and starting the TOF circuitry by creating two pulses 100 nsec wide and 140 nsec (exactly 4 cyclotron RF periods) apart. If a phototube trigger was detected during either of these two time windows, a proton-neutron (or in general charged particle-scintillator) coincidence was signalled. There were two windows in order to generate a spectrum of events similar to those events that were random and included in the set of "real" coincidences by chance. A subtraction of the real minus random energy distributions would provide a cleaner spectrum for the nuclear process under study. Almost identical circumstances must be provided for the real and random spectra, hence the period between the windows should be as small as possible (to protect against beam changes, etc.), but the windows must start an integral number of RF periods apart. Since the main TAC was used on the 100 nsec range, and the RF period is 35.1 nsec, this required that the width of each pulse be 100 nsec and the separation be 140 nsec. The second window corresponded to real

events, and its position was adjusted in time so that most of the accessible kinematic locus was within the range of the window. If the position in time of the real and random windows were interchanged, low energy neutrons from real coincidences (but not accepted by the real window) would contaminate the random spectrum.

Neutron timing began with the production of an anode pulse in one of the photomultipliers. The anode signal of each phototube was split, the major portion (3/4) going to the CFD and the minor portion (1/4) going to the pulse height measurement system. The outputs of the CFDs were mixed with an "OR" circuit and sent to the coincidence system. The pulse heights were added and sent to the linear gate, which when opened by the detection of a coincidence, integrated the pulse height over a period of 100 nsec. Normally the signal from a dynode would be used for pulse height determination, but this would be difficult when fast gating is desired because the dynode preamplifier in the phototube base produces a slow output. If the pulse height was above a certain threshold specified by an SCA, a gate was generated which allowed acceptance of the signal by the analog-to-digital converters (ADCs) and computer system. The SCA was placed on the integrated pulse height signal rather than the raw pulse from the phototube, because the current peak suffers more statistical variation than the integrated peak. The three other thresholds (specified by the two neutron CFDs and the crossover SCA) were always set to lower levels than this final SCA so that it alone determined

the neutron threshold.

Pulse shape discrimination (PSD) to eliminate gamma ray events was performed by measuring the time difference between the anode pulse (as provided by the CFD) and a timing signal derived from the integrated dynode pulse. The CFD on the anode started a second TAC, while the dynode signals from the two tubes were capacitively coupled to preamplifiers located in the phototube bases. Their OR'ed outputs were sent to a double delay line amplifier and an SCA detected the zero crossing of the signal and stopped the TAC. A further description of PSD is given in Section 2.7.

Three logic flags were generated: PILE-UP (produced if the pile-up gate sensed that two charged particle triggers occurred sooner than 3 μsec apart), RANDOM (produced if a coincidence occurred during the first time window), and TUBE-ID (produced if the phototube signal came from the lower phototube).

A considerable proportion of the electronics was present solely to ensure that linear signals were gated, TACs started, and flags generated only if a coincidence between a phototube trigger and a charged particle occurred. This reduced deadtime in the ADCs and TACs to .15% typically, and reduced the probability of mixing of the flags. Because the gate for the phototube pulse height was open only for 100 nsec, no significant number of pile-ups occurred in it and a pile-up unit was not required. The delays shown in the schematic consisted of fixed lengths of RG 8/U cable supplemented by adjustable delay

boxes.

When the pulse height "PH" was above the selected threshold, the "GATE" signal was generated. This signal was used to enable the ADCs and gate the flags into the computer (PDP 15/40) interface. Using a programme named "MULPAR", a scatter plot of any pair of the six ADC signals could be displayed on a 10"x10" CRT, for any combination of flags. MULPAR was also used to log the incoming events on magnetic tape. Most gamma ray events were identified (using software particle identification procedures to be outlined later) and were not logged on magnetic tape. This on-line procedure cut the number of tapes used by a factor of three. The Faraday cup current was integrated using a Brookhaven Instruments Corporation model 1000 integrator. The number of pulses produced as output by this device is proportional to the number of nanoCoulombs of charge it integrates. These pulses were fed into an ADC where the number of pulses was totalled and given to the computer to be stored on tape along with the data. The digitized Faraday cup count represents an accurate live-time normalization factor. Various scalers recorded many other experimental parameters required to monitor the status of the experiment.

Section 2.4 Timing

Because the energy of a neutron is difficult to determine using ordinary techniques, neutron energy is usually determined using time-of-flight techniques. The signal which begins a cycle in a typical TOF system usually originates from either of two sources: 1) the detection of the beam burst at some fixed position (using gamma flash detectors, electromagnetic sensors, current pulse sensing at the Faraday cup, RF pickup, etc.), or 2) the detection of a particle in one of the primary detectors. The first method is susceptible to unpredictable variations in the beam profile possibly ruining the resolution. These changes can be controlled successively over a period of several seconds by using a feedback element to the cyclotron, but this technique is awkward. The beam pulse is typically larger than one nsec wide and can have a complex structure without careful machine tuning. If timing is performed with respect to the beam, one may observe neutrons from successive beam bursts that overlap one another after drifting from the target to the detector. The second approach suffers from none of these disadvantages and was the one chosen for this experiment, using the DELTA detector to detect protons or deuterons.

TOF techniques are also useful with pulsed accelerators because they can allow a reduction in background due to prompt gamma rays. Since neutrons at 45 MeV travel three times as slowly as photons, an adjustment of the neutron flight path can place most of the data of interest outside of the gammma ray bands.

Section 2.4.1 Proton Timing

Timing uncertainty dT in a surface barrier detector may be expressed (C69) as

$$dT = Nd^2C/(mVdE)$$

where N is the noise in the system, d is the detector thickness, C is the total capacitance, m is the electron mobility in silicon, V is the bias voltage, and dE is the energy deposited in the detector. Capacitance is very important to timing resolution, with noise being proportional to it and timing resolution being inversely proportional to it. In an effort to reduce capacitance, a short cable length was used between the detector and preamplifier (by placing the preamplifier inside the chamber next to the detectors), as well as a small timing detector with an area one half of the laboratory standard (200 mm^2). It is common for thin (200 μm or smaller) surface barrier detectors or thicker Si(Li) detectors to be used for timing purposes, but an intermediate thickness surface barrier detector is desirable (H72,E71,S68) to increase signal strength and further decrease capacitance. Hence for this experiment a 750 μm surface barrier detector was chosen. Because timing resolution is also inversely proportional to the risetime of the signal (fast signals have smaller time walk errors), the risetime was reduced by cooling the detector to liquid nitrogen temperatures where the electron mobility of silicon is greatest (E71), being 11 times the value at room temperature. This also had the effect of reducing the leakage current by a factor of 100. Cohen and Fink (C67) have

suggested that the detector should be overbiased by a factor of two for optimum time resolution, but because this can shorten detector life, it was not attempted.

It is known (E71) that superior timing resolution cannot be obtained from the charge pulse using a charge sensitive preamplifier. A more advanced design picks off the current pulse, but then the amplifier senses only part of the current from the detector (S68). Instead, a voltage sensitive preamplifier (S68) developed at Argonne National Laboratories was used. This device sensed the pulse from the detector while it was stored on a 470 μh inductor and the slightly delayed detector signal continued along to a charge sensitive preamplifier for energy determination with no significant degradation in energy resolution. The voltage sensitive amplifier was located next to the detectors, but was isolated from the cooled surfaces in order to maintain the transistors within their operating temperature range. Sherman et al (S68) designed a complete timing system, but this experiment used only their preamplifier and substituted standard NIM modules for the remainder of their specialized electronics. In (S68) it was concluded that the system had a walk of 100 psec over a 30 to 1 dynamic range, but the present experiment used only an 11 to 1 range. The commercial amplifiers used were found to compare favourably to the specialized products described in (S68). These factors assured a subnanosecond timing system for the charged particles. A measurement (M74) detecting both protons from p-p elastic scattering in coincidence using this charged

particle system and a small scintillator mounted on an RCA 8575 phototube showed that the surface barrier timing resolution was 350 psec, but walk was not important in that measurement. Since that measurement of resolution, several improvements have been made to the system.

Section 2.4.2 Neutron Timing

Let E be the neutron energy, and TOF its time-of-flight. Nonrelativistically then,

$$dE = -kE^{3/2}dTOF$$

(where k is a constant) so that the worst energy resolution occurs for high energy neutrons. This can be reduced by increasing the flight path (also increasing neutron attenuation), but maintenance of the same solid angle then requires the use of larger area scintillators which will degrade the timing resolution. The solution to this problem was the use of two scintillators each coupled to a separate phototube.

One would expect that the timing resolution would be largely influenced by the variability in position of the interaction of the neutron in the scintillator. Considering a 5 inch long thin tube of scintillator with absorbing walls, this time difference dT is

$$dT = 5/v_{neut} - 5/(c/n)$$

where v_{neut} is the neutron's velocity and c/n is the speed of light in the scintillator in inches/nsec. For 5 MeV neutrons this is 3.47 nsec and for 40 MeV neutrons it is .81 nsec. However, the walls of our scintillators were covered with

isotropically reflecting paint, and this tends to improve the timing resolution by averaging out the interaction points due to the multiplicity of circuitous paths followed by the photons in the scintillator. Timing uncertainty is also increased by the variation in transit time of photoelectrons, phototube noise, and jitter and walk in the discriminator. Dark current can be decreased by refrigeration of the phototube, but this was not attempted. The 28 to 1 dynamic range of pulse heights (corresponding to 35 MeV to threshold energy neutrons) was well within the range over which the discriminators we used can provide good timing. A measurement of the timing resolution of these neutron detectors was made during some (p,n) experiments (Wi71) and it was found to be approximately 500 psec.

Section 2.5 Energy Resolution

Several effects contribute to the spread in energy of the proton detector system. The first is the energy width of the incident proton beam, estimated to be 300 keV (although on the last run it approached 1 MeV). The second is the kinematic spreading due to finite collimator size; this was typically 700 keV for elastic scattering from ^{3}H. The angular acceptance for the neutron and proton detectors was chosen after an analysis by the computer code MOMERATH (W70). Large solid angles are desirable to decrease data collection time, but they smear out the experimental cross sections and lower the peak value. Figure 2.5.1 shows the effect of our nonzero slit size on a Gaussian recoil momentum distribution with a HWHM of 45 MeV/c. A slit size of 1.64° by 3.28° for the neutron detector was used, thus overestimating the finite resolution effect (because the detector looks like an "8", but the resolution was calculated for a rectangular shape with the maximum dimensions of the "8"). As may be seen from the diagram, the peak is lowered by 1.2% but the width is relatively unaffected. The third effect is the intrinsic resolution capability of the detectors, measured to be approximately 50 keV although it could deteriorate as the run progressed. A fourth factor is the deterioration of the signals due to electronic problems in the amplifiers, summing units and cabling system. A fifth effect is the straggling of the incident and scattered particles in the target and surrounding foil.

Timing resolution does not have any direct effect on the

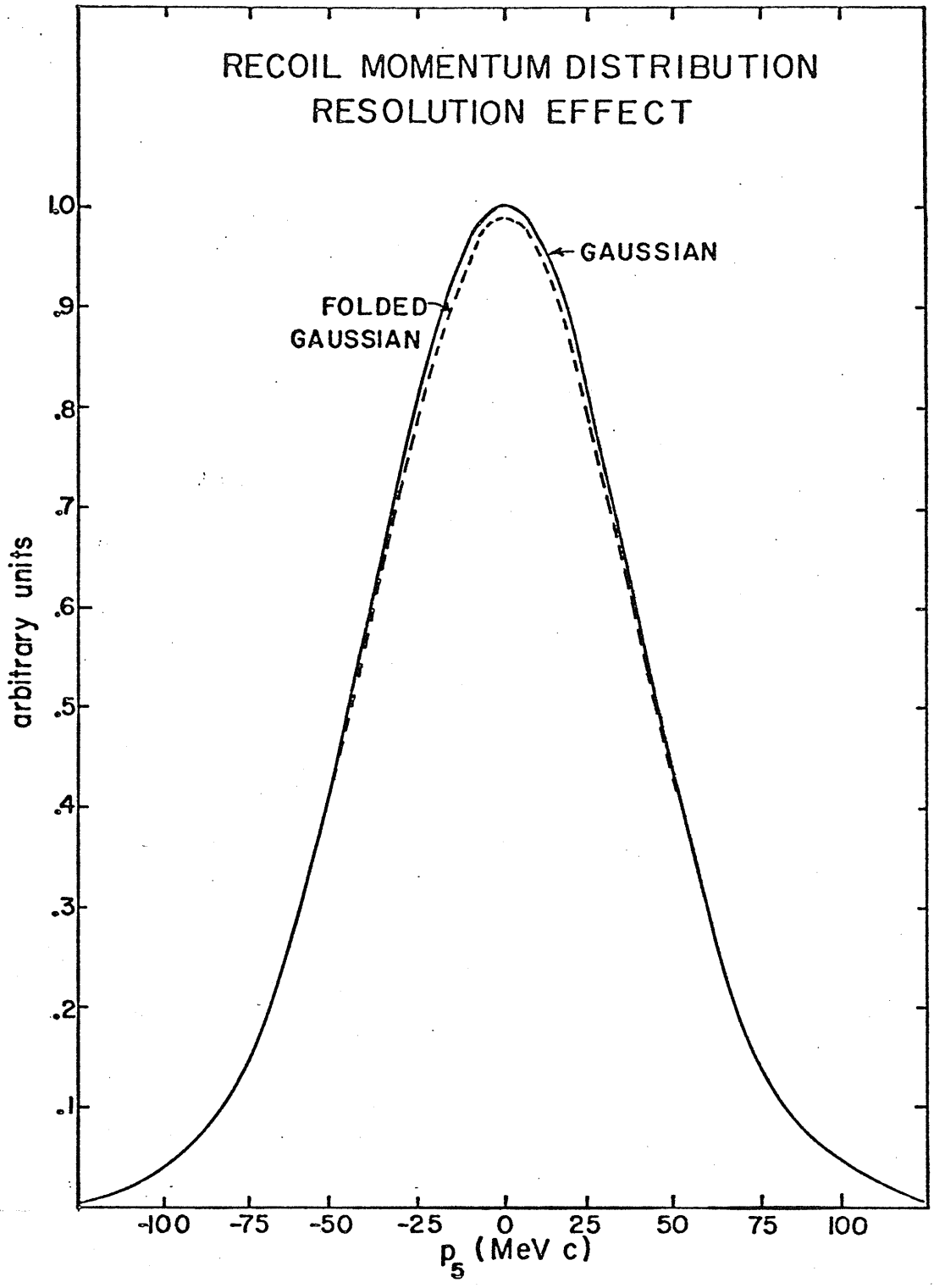

Figure 2.5.1 Resolution Degradation Due to Slits

The effect of nonzero slit (or detector) size is shown for a recoil momentum distribution with a width of 45 MeV/c

energy resolution of the projected spectra presented in Chapter 4 since it widens the kinematic locus only in the direction of projection (all projections were made onto the charged particle energy axis). However, it can produce some overlap of the d and d* loci and this could cause improper measurement of the d* cross section. The energy resolution in the Q-value spectra presented in Chapter 4 is a combination of the proton energy resolution and the neutron timing resolution, the latter being estimated to be 600 psec. The effect of this time resolution on energy resoluton is 1.0 MeV for 40 MeV neutrons and 46 keV for 5 MeV neutrons.

Section 2.6 Neutron Efficiency

The efficiency of a neutron detector depends principally upon the geometry and type of scintillator, pulse height threshold chosen for the photomultiplier signal, and the energy of the neutron. The pulse height threshold was determined by using the 1.275 MeV gamma rays from the decay of ^{22}Na (Compton edge at 1.067 MeV), and the 4.43 MeV gamma rays from a carbon screen lowered into the proton beam (from the decay of the first excited state of ^{12}C). Figure 2.6.1 shows a typical calibration spectrum. A point at two thirds of full height of the Compton peak was chosen as being the channel corresponding to the maximum electron recoil energy. This procedure has been verified by most experimenters (P61), but differs slightly from Knox (Kn72), who used the .87 point on the peak. The threshold will be quoted in terms of the energy of an electron that would produce just enough light to cause an event to be recorded. A neutron having this energy would produce less light because of nonlinearities in light output associated with heavily ionizing radiation. The threshold varied from run to run, but was typically 800 keV with an uncertainty and drift of less than 100 keV (except during portions of the first run when the drift was larger). A Monte Carlo calculation using a computer code written by Stanton (St71) determined the neutron efficiency for a single 4.5 inch diameter by 5 inch long cylindrical detector. The programme is much the same as that written by Kurz (K64) in that it uses nonrelativistic kinematics and assumes that all charged particles stop in the scintillator. The programme was

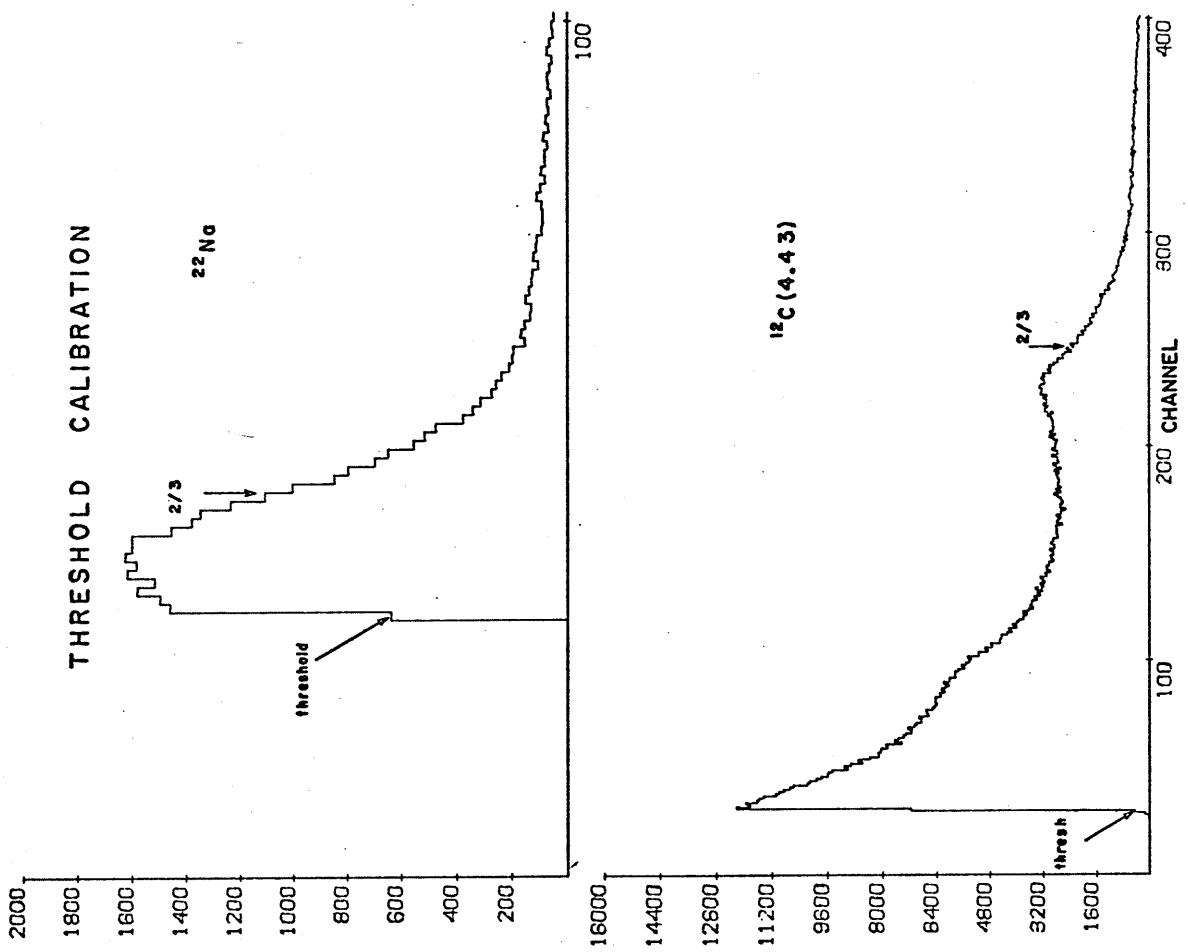

Figure 2.6.1 Threshold Determination

Two γ rays are used to calibrate the pulse height from a photomultiplier and determine the threshold in equivalent electron volts.

modified by feeding in the most modern cross sections, the H:C ratio for NE213 and the neutron response function for NE218 (M70) (which should be like that of NE213 because of their similar properties). Typical curves generated by this efficiency code are shown in Figure 2.6.2. Beyond about 15 MeV, the efficiency is near 30% roughly independent of threshold. Stanton has estimated (St71) that the efficiencies generated by his code are correct to within 5%, but an additional uncertainty is created by the stacking of one detector on top of the other, creating multiple scattering problems. Such scattering will increase the efficiency and thus decrease the measured cross sections, but the effect is not expected to add more than 1 or 2 percent to the uncertainty, bringing the total to 6%.

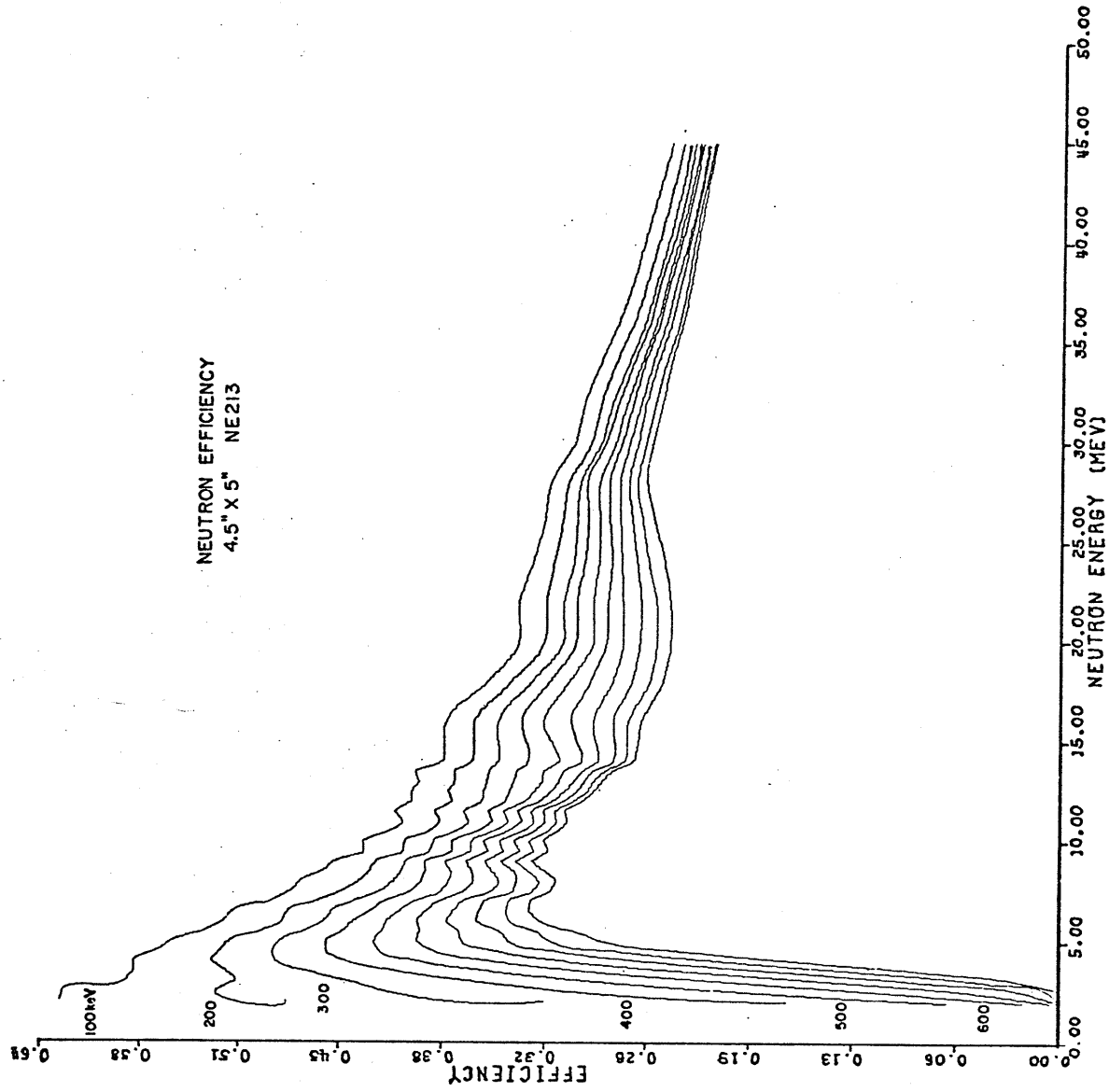

Figure 2.6.2 Neutron Efficiencies
Neutron efficiencies are shown for a 4.5"x5" cylinder of NE213 for thresholds ranging from 100 to 1000 keV in steps of 100 keV.

Section 2.7 Pulse Shape Discrimination

It has been known for some time (B56) that for certain organic substances one can differentiate between excitation due to gamma rays and neutrons. A brief discussion of the subject is in order.

There are two important stages in the process of fluorescence, the first being the emission of light by molecules directly excited by the ionizing radiation, and the second being emission from molecules excited by the recombination of electrons and primarily ionized molecules. When neutrons interact in scintillators it is largely through the production of highly ionizing radiation like protons, while gamma ray interactions mostly produce weakly ionizing radiation like electrons. Whenever the density of ionization is large, some of the molecules are quenched or forced to de-excite without radiating light and are thus undetectable by the phototube. Hence a larger fraction of the neutron (compared to the gamma ray) energy is undetectable and its pulse height is smaller, this effect varying with energy and causing nonlinearities in its pulse height. Much of the light that is created by the neutron is produced in the second process which occurs later in time when the ionization density has decreased, while most of the light due to gamma rays is emitted in the initial surge of fluorescence. Thus neutrons cause a longer decay component than gamma rays. Because the risetime of the scintillation is independent of specific ionization, the risetime of an integrated dynode pulse must then be a reflection of the decay time

of the scintillation and type of detected particle. When the anode signal is used to start a TAC and the zero crossing time for the integrated dynode pulse after shaping by a double delay line amplifier is used to stop the TAC, the output of the TAC is called the pulse shape discrimination (PSD) signal and is larger for neutrons than gamma rays. This technique is illustrated in Figure 2.7.1. The present experiment used NE213 as the scintillator because of its well-known properties of PSD. Typical PSD-PH spectra are shown in Figure 2.7.2. The "bottom" scintillator is clearly superior, but even for the relatively poor neutron-gamma separation of the top scintillator, it is not difficult to draw a locus around the gamma rays on the left to exclude them. The separation is more than 5 nsec, quite adequate for this procedure, but inferior to the value of 29 nsec quoted by Miller (M68).

PULSE SHAPE DISCRIMINATION

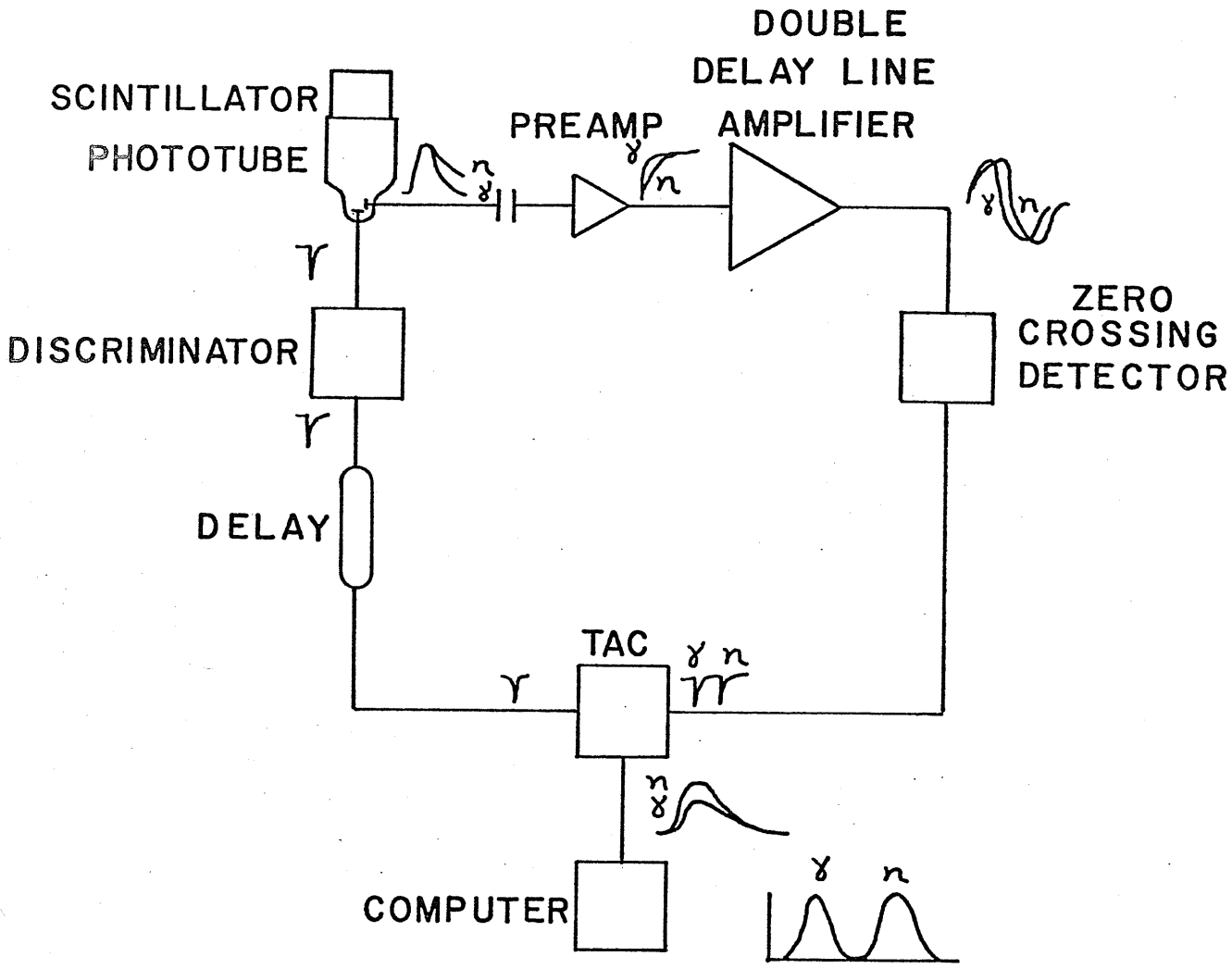

Figure 2.7.1 Pulse Shape Discrimination Electronics

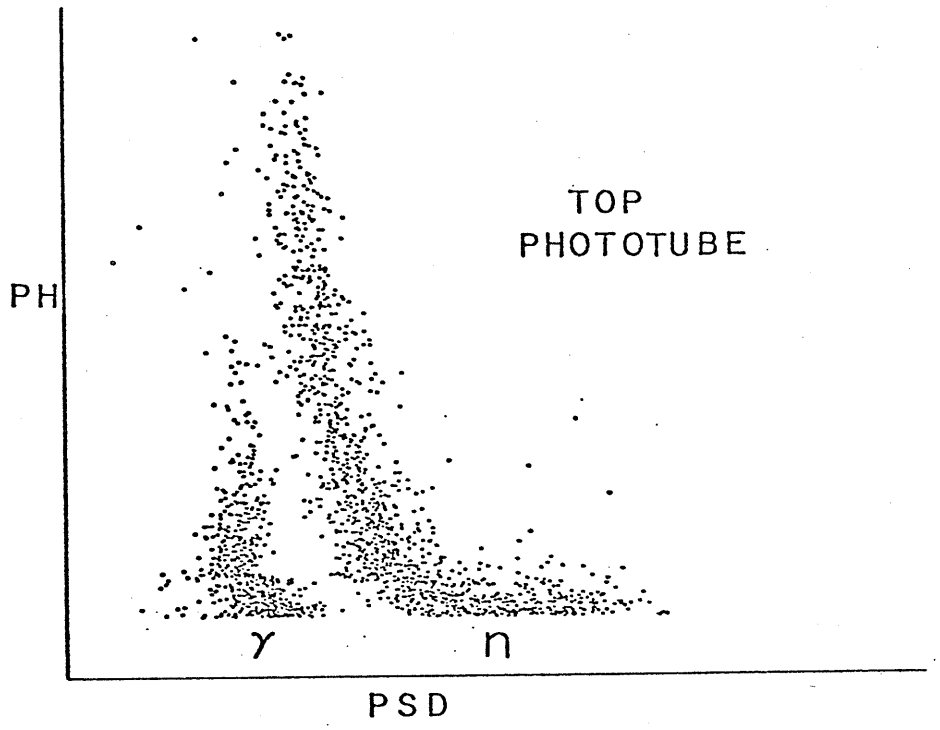

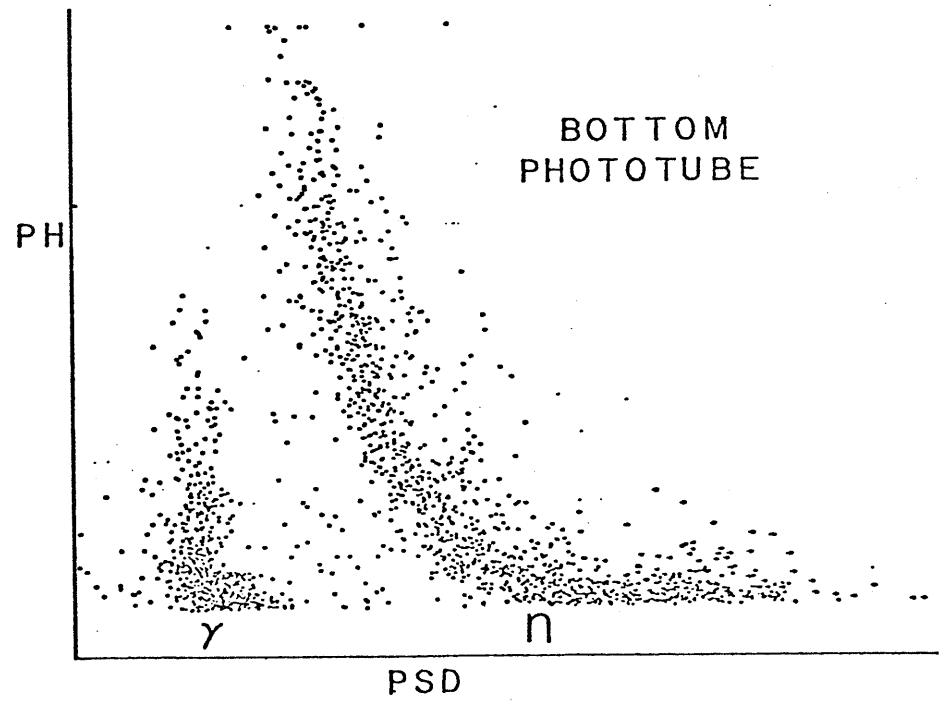

Figure 2.7.2 PSD Characteristics for the Scintillation Counters

Section 2.8 Tritium Content of the Target

After the last (p,pn) run a separate experiment was performed on the 45° right beamline to determine the tritium content of our target. A Los Alamos group has measured (D71) the proton elastic cross section for ^3H at several energies, the highest being 19.48 MeV. This energy was chosen for the incident protons in our experiment since it corresponds to the lower energy limit of the Manitoba cyclotron under normal beam extraction conditions. The recoil tritons were detected by a semiconductor telescope consisting of one 100 μm and one 1000 μm surface barrier detector. Using the PDP15 computer, particle identification loci were drawn around the triton peak at each angle and an energy spectrum was collected. At 19.48 MeV there is very little triton background from reactions on scandium and aluminum to contaminate the spectrum. A five point angular distribution centred around the minimum in the cross section (where the error due to nonzero slit size is smallest) was accumulated. A .6°x1.2° angular acceptance was used. The tritium content was determined to be .27±.01 mg/cm². A summary of the results is shown in Table III. The quoted uncertainties for the Los Alamos data are less than 1% in the majority of cases. After including kinematic and other factors an uncertainty of 4% is quoted for the tritium content of our target. This uncertainty is acceptable since it is smaller than most other contributions to the uncertainty in our (p,pn) cross sections.

The tritium was absorbed into the scandium at high

Table III

Tritium Content Analysis

Triton Lab Angle	Proton Lab Angle	Cross Section (mb/sr)	Counts in Peak	^3H Content (mg/cm^2)
10.1	150.0	17.43	10250	.2689
21.5	120.0	7.308	7344	.2608
25.7	110.0	4.443	5272	.2702
30.3	100.0	3.046	3476	.2705
45.7	70.0	18.42	7120	.2785
			average	.2698 mg/cm^2

Uncertainties

Maximum variation in measured content	3.3%
Maximum statistical uncertainty	1.5%
Maximum Los Alamos data uncertainty	1.4%
Estimated background uncertainty	.5%
Charge integration uncertainty	±.5%
total uncertainty	4.1%

temperatures. During the (p,pn) experiment the target was never exposed to more than 40 na of 45 MeV protons, depositing 4.6 mW. During the measurement of the tritium content no more than 10 na of 19.5 MeV protons was used, depositing no more than 3.3 mW in the target. Since the target is basically metallic and was securely fastened to relatively massive bodies, it was expected that thermal conduction would remove heat rapidly and avoid the liberation of much tritium. Any free gas would be pumped away by the special exhaust system already mentioned. The possibility was also considered that the scandium might peel off the aluminum backing, but the target cell and the molecular sieve should be capable of containing such radioactive components.

During the (p,pn) experiment, at intervals of one day, a monitor "singles" triton spectrum was collected at 35°. SCA windows were placed on the signals from the charged particle telescope to select only the recoil tritons and 10000 events collected. There was a substantial background from the Sc and Al, but the measurements confirmed that the tritium content was constant during each run. Typical spectra are shown in Figure 2.1.1. Because of the large background, it was necessary to subtract the contribution due to the scandium and aluminum. After this correction, the ^{3}H content for the second and third runs is calculated to be .31±.04 mg/cm^{2}. A cross section of 1 mb/sr from the $^{3}He(p,p)^{3}He$ 45 MeV experiment of Morales et al (M75) was used for these determinations (in the absence of any appropriate ^{3}H elastic scattering data). These were not

precision measurements and were only used to check for stability of the target within each run. Near the end of the third run, one monitor triton spectrum was collected with the target ladder moved 1/8 inch vertically in order to check the uniformity of the target. The same tritium content was observed from this measurement as at the original location.

Unfortunately any tritium in the pump or scattering chamber could not be detected immediately because no available monitor could sense small quantities of tritium. Standard radiation monitors easily detected the 4 keV Xrays produced in the scandium, but their sensitivity was reduced to several percent of the target by normal background. However, areas which had potential exposure to tritium evolved from the target were checked afterwards by collecting samples and depositing them in a liquid scintillation counter. Small quantities were detected on the aluminum around the target cell, but none in the pump or scattering chamber. These negative results support the view that the tritium content of the target was constant for all intents and purposes throughout the twelve month period spanned by the three runs, except for the normal decrease due to the 12.6 year half life of ^{3}H.

Chapter 3

THE ANALYSIS

Section 3.1 Method of Analysis

Energy spectra such as the one shown in Figure 3.1.1 for protons on CD2 allowed a calibration of the proton energy axis. Typically, more than half a dozen angles were covered to give a calibration extending from 7 MeV to 40 MeV. Linear fits to the data were always used.

Six ADC words describing each event were available on magnetic tape, stored in a time-ordered fashion along with the accumulated live time Faraday cup count and the three flags (PILE-UP, RANDOM, and TUBE-ID). Each file consisted of 17,856 events, most of them corresponding to neutron events, since on-line PSD as previously described had been used to reject most of the gamma rays and they were not logged on tape. Several scatter plots were created and displayed on a CRT for each file: EPSILON versus SIGMA, DELTA versus SIGMA, (Figure 3.1.2) and PH versus PSD (Figure 2.7.2). Using a light pen, loci were drawn around the protons or deuterons in the first two displays to accept them and around any remaining gamma rays in the third display to exclude them. The philosophy behind loci drawing is that if a choice must be made, it is better to include other reactions than to exclude any (p,pn) or (p,dn) events- expecting that the other reactions will occupy regions of phase space not of interest. Elastically scattered protons had sufficient energy so that they did not stop in the detector

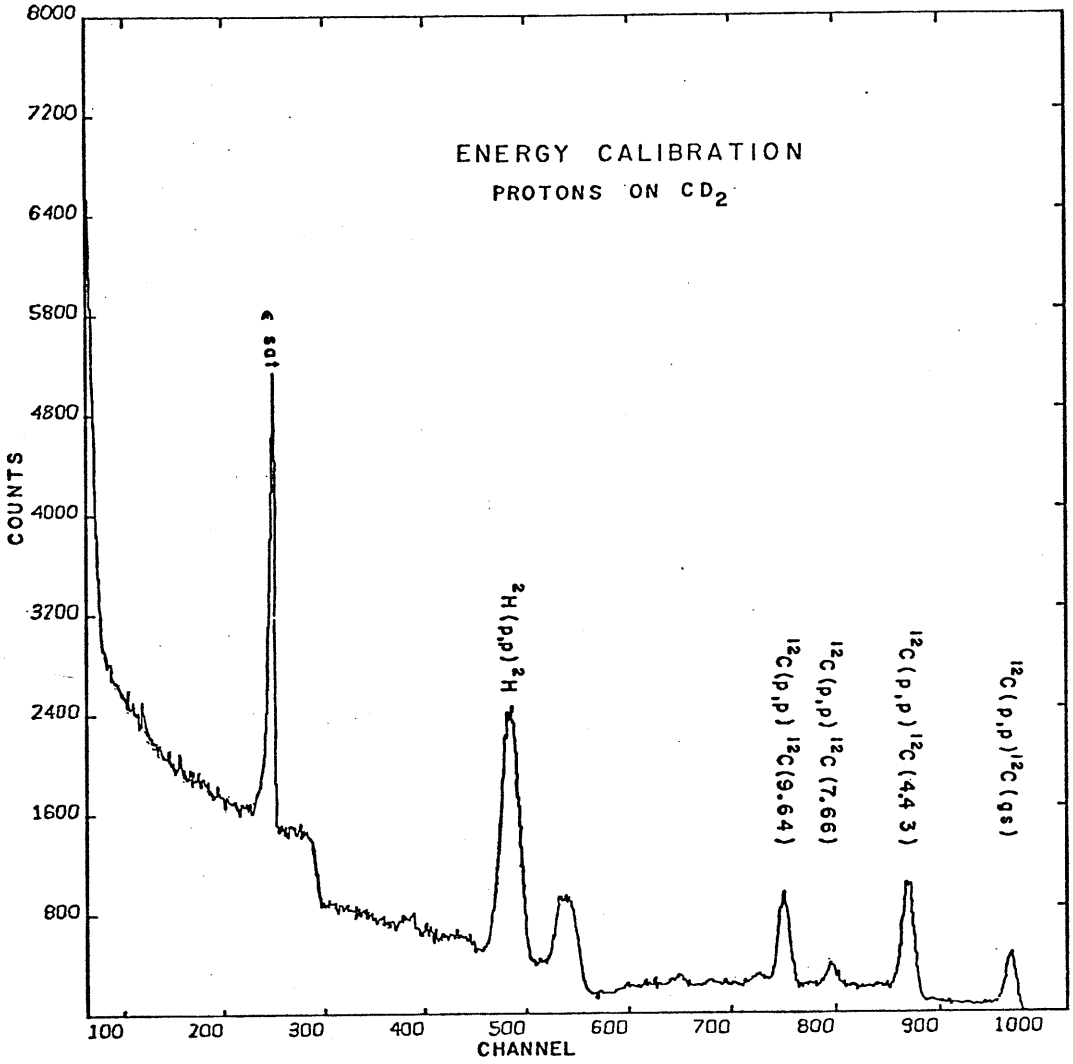

Figure 3.1.1 Energy Calibration for Charged Particle Detectors

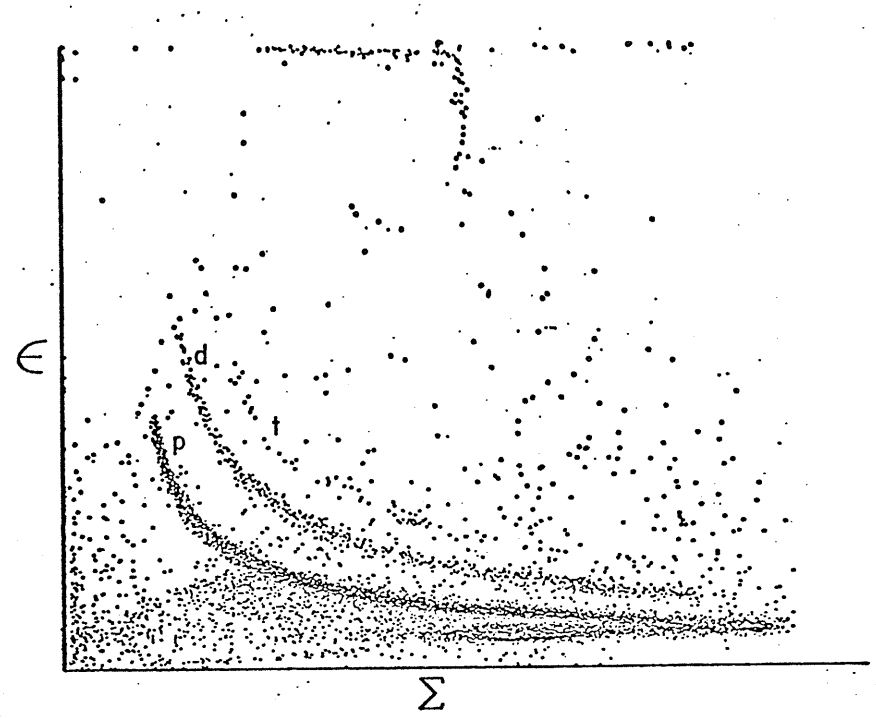

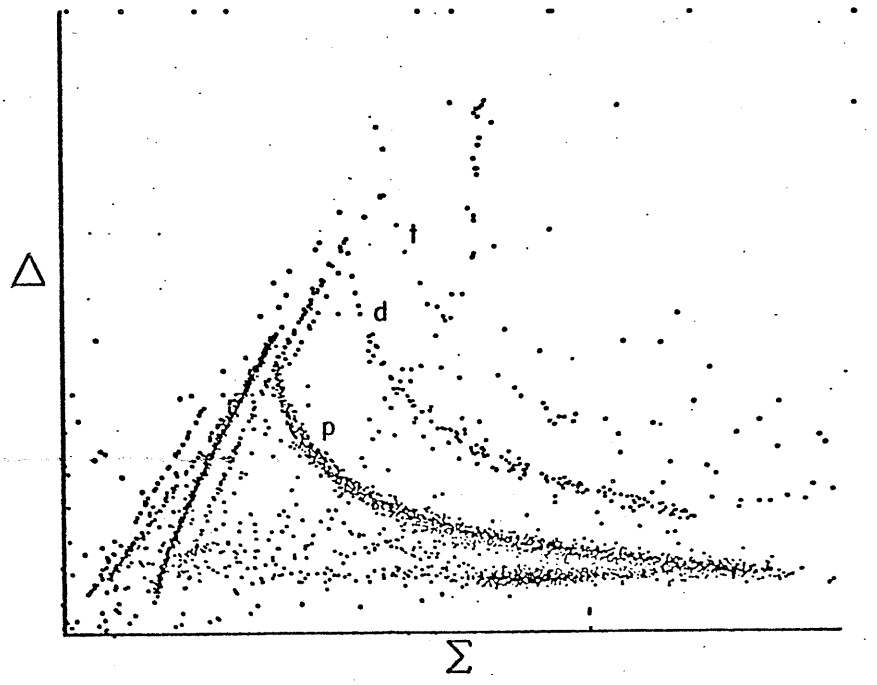

Figure 3.1.2 Particle Identification
The loci for p, d, and t are shown

stack. The higher the energy of these particles, the lower the energy that they deposited in the detectors. Thus the proton locus in Figure 3.1.2 "folds back" to lower energy. The maximum energy of interest was 33 MeV (so that a canted detector was not required to stop the particles), but the larger the thickness of silicon, the less the folded back proton locus would interfere with the locus for lower energy protons. The magnification of the EPSILON and DELTA signals produced better separation of the loci for the protons, deuterons, and tritons, as well as the folded back proton locus.

Off line analysis of the data tapes was performed as follows. For each angle pair studied, a set of criterion functions was generated telling the computer to construct four files of TOF versus SIGMA events for proton-neutron events that were not piled-up. These were top neutron detector reals, bottom reals, top randoms, and bottom randoms. The process was then repeated for deuteron events. Typically, no more than 6% of the events were rejected because they were piled up. The real:random ratio (a measure of the signal-to-noise ratio) near the peak was typically 8 for $^{3}H(p,pn)d$, 2 for $^{3}H(p,pn)d^{*}$, and 12 for $^{3}H(p,dn)p$. With as many points in the kinematic loci as possible displayed on the screen, two points were selected from the middle of the $^{3}H(p,pn)d$ locus using the light pen. The TOF axis was calibrated using proton energy calibrations, energy loss equations, corrections for the TOF of the proton, and relativistic kinematics, assuming only the linearity of TOF.

This calibration would change from angle to angle because the neutron detector was not always the same distance from the target. The procedure provided a typical calibration for 512 channels with 350 psec/channel for the TOF axis and 78 keV/channel for the SIGMA axis. Usually loci for (p,pn) events were better defined than (p,dn) loci because of greater straggling effects for deuterons than protons.

TOF versus SIGMA scatter plots have a slightly different appearance than the more standard energy versus energy plots. Figure 3.1.3 shows how the two compare for some of the angles studied.

The Q-values for some reactions of interest are as follows:

$^{3}H(p,pn)d$ and $^{3}H(p,dn)p$	Q = -6.258 MeV
$^{3}He(p,pn)pp$	Q = -7.718
$^{3}H(p,pn)d^{*}$	Q = -8.482
$^{45}Sc(p,pn)^{44}Sc$	Q = -11.321
$^{27}Al(p,pn)^{26}Al$	Q = -13.058

Figure 3.1.4 shows some kinematics emphasizing the shape of the $^{3}H(p,pn)$ loci for various Q-values and the relative energy loci for $^{3}H(p,dn)p$ and $^{3}H(p,pn)d$.

The data from the two neutron detectors were analysed separately in case of a disparity in the time origins or a marked difference in the thresholds. This also provided a check as to the consistency of the projected spectra for the two detectors. No statistically valid inconsistency was observed.

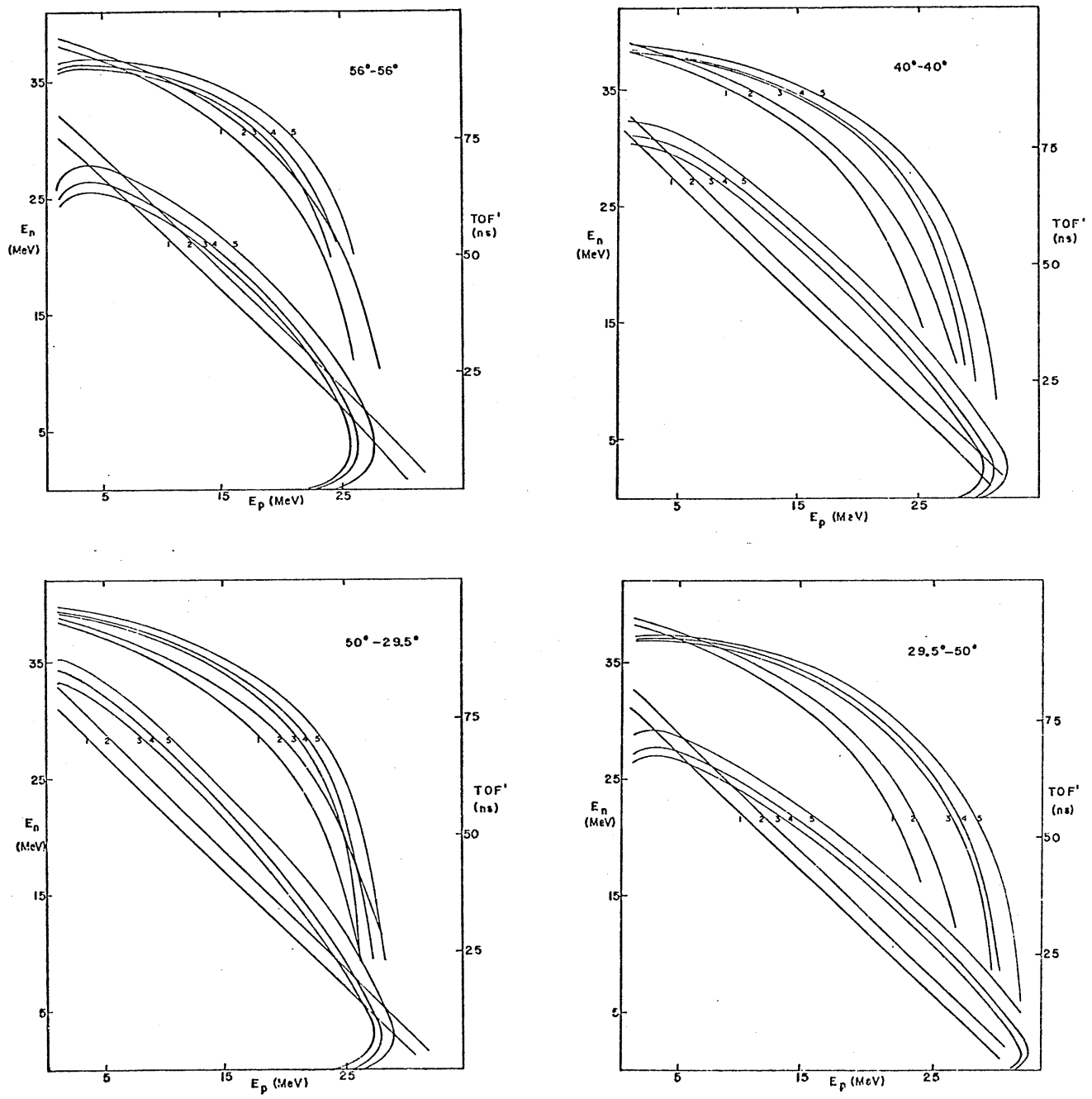

Figure 3.1.3 Comparison of Energy-TOF and Energy-Energy Loci

The shapes of the kinematic loci for various reactions at several angles are shown. Within each graph, the top set of curves represent T_3 vs TOF_4 loci while the bottom set are T_3 vs T_4 loci. 1) $^{27}Al(p,pn)^{26}Al$ 2) $^{45}Sc(p,pn)^{44}Sc$ 3) $^{3}H(p,pn)d^{*}$ 4) $^{3}He(p,pn)pp$ 5) $^{3}H(p,pn)d$

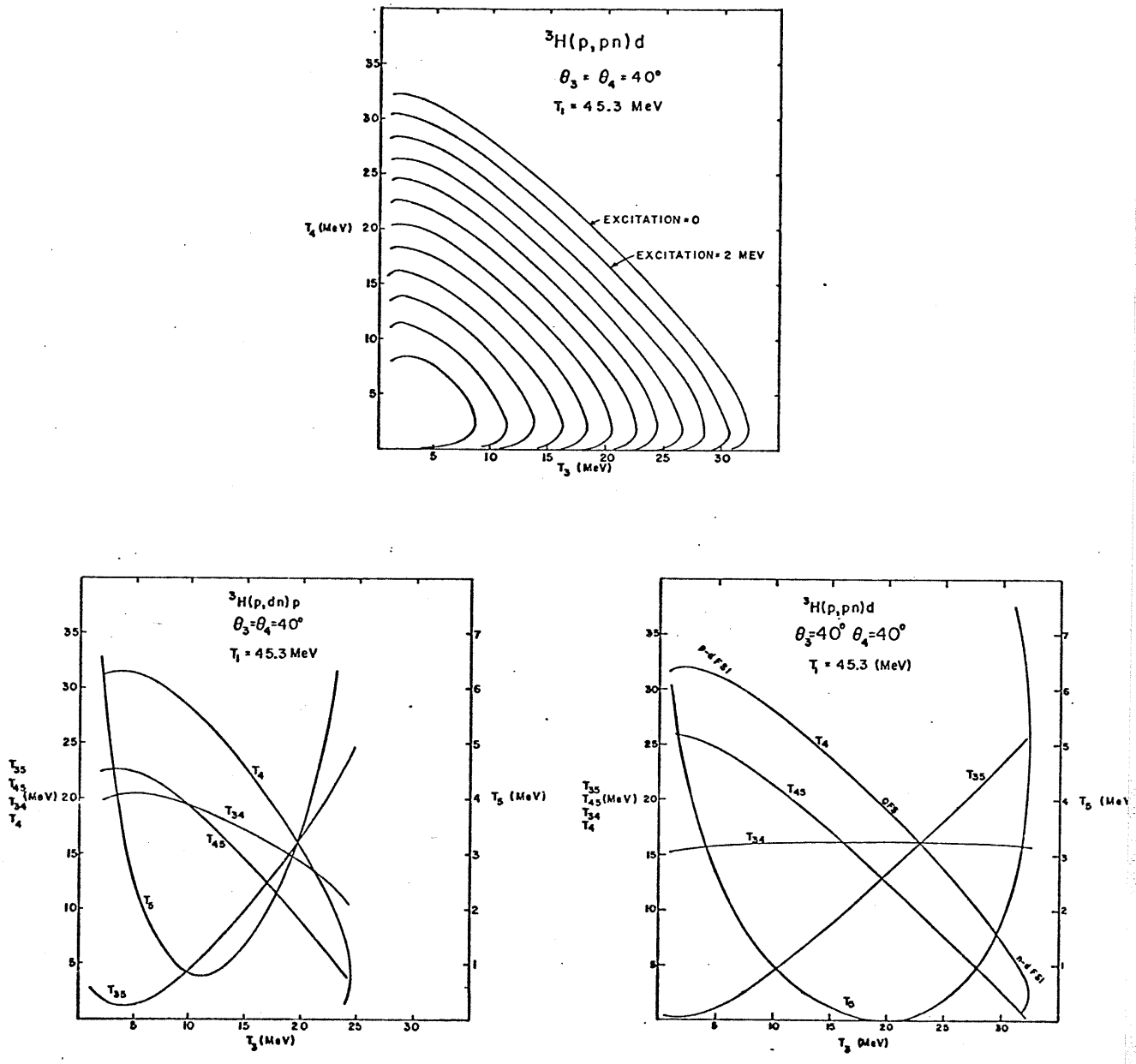

Figure 3.1.4 Q-Value and Relative Energy Kinematics

Top: This graph shows kinematic loci for ^{3}H(p,pn) at 40^o-40^o for Q-values in steps of 2 MeV excitation for recoil.

Bottom: Kinematics for ^{3}H(p,dn)p and ^{3}H(p,pn)d at 40^o-40^o emphasizing the variation in relative energies between two bodies.

Figure 3.1.5 shows a TOF versus SIGMA scatter plot populated with events associated with gamma rays. It is random with respect to SIGMA with the bands 35 nsec (the RF period) apart in time. Most of the aperiodic gamma rays are 2 MeV in energy, suggesting that they are a product of neutron capture by hydrogen in concrete, while the periodic gamma rays are associated with the gamma flash from the target. Some scatter plots of real and random neutron (p,pn) and (p,dn) events from the tritium and dummy targets are shown in Figures 3.1.6 and 3.1.7. Real and random events cancelled each other and were removed from the list of surviving events in the random-subtracted plots if a random event occurred within a certain radius of a real event in the plot. This technique was used only for display. The density of points in a scatter plot is proportional to

$$\frac{d^4\sigma}{d\Omega_3 d\Omega_4 dE_3 dTOF_4}$$

The enhancements due to the $^3H(p,pn)d$ and $^3H(p,dn)p$ reactions are clearly visible for all spectra.

Once the energy calibrations for TOF and SIGMA were available, loci could be generated for any relevant process, at any angle, by specifying the parameters of the reaction. An upper and a lower locus bounding the region of interest were specified using the Q-value. Thus, a 2 MeV wide band around the $^3H(p,pn)d^*$ region was created by specifying Q=-7.48 and -9.48 for the upper and lower limit respectively-even though the enhancement due to this process was never visible on the

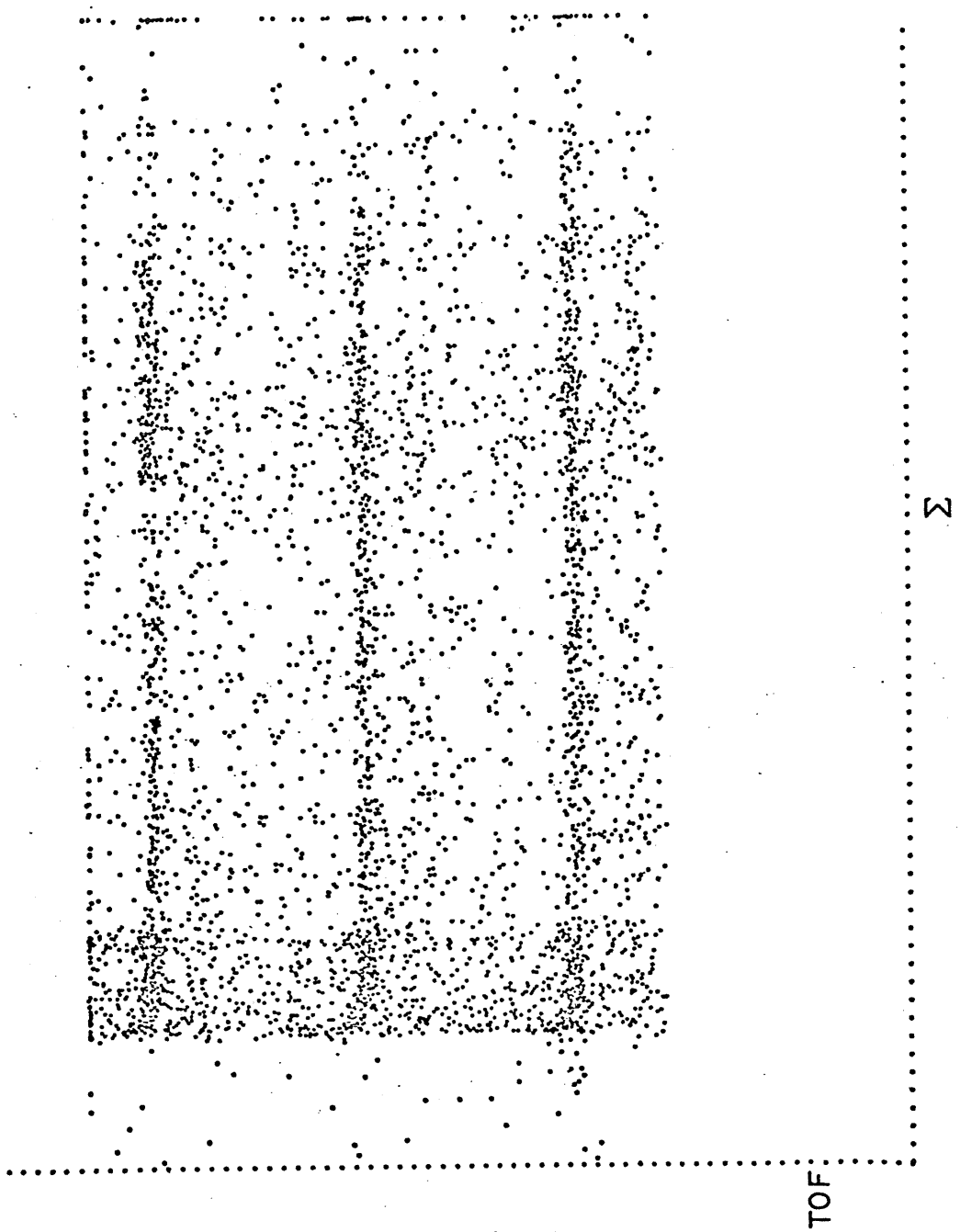

Figure 3.1.5 Gamma Ray Time Structure
The bands are 35 nsec apart.

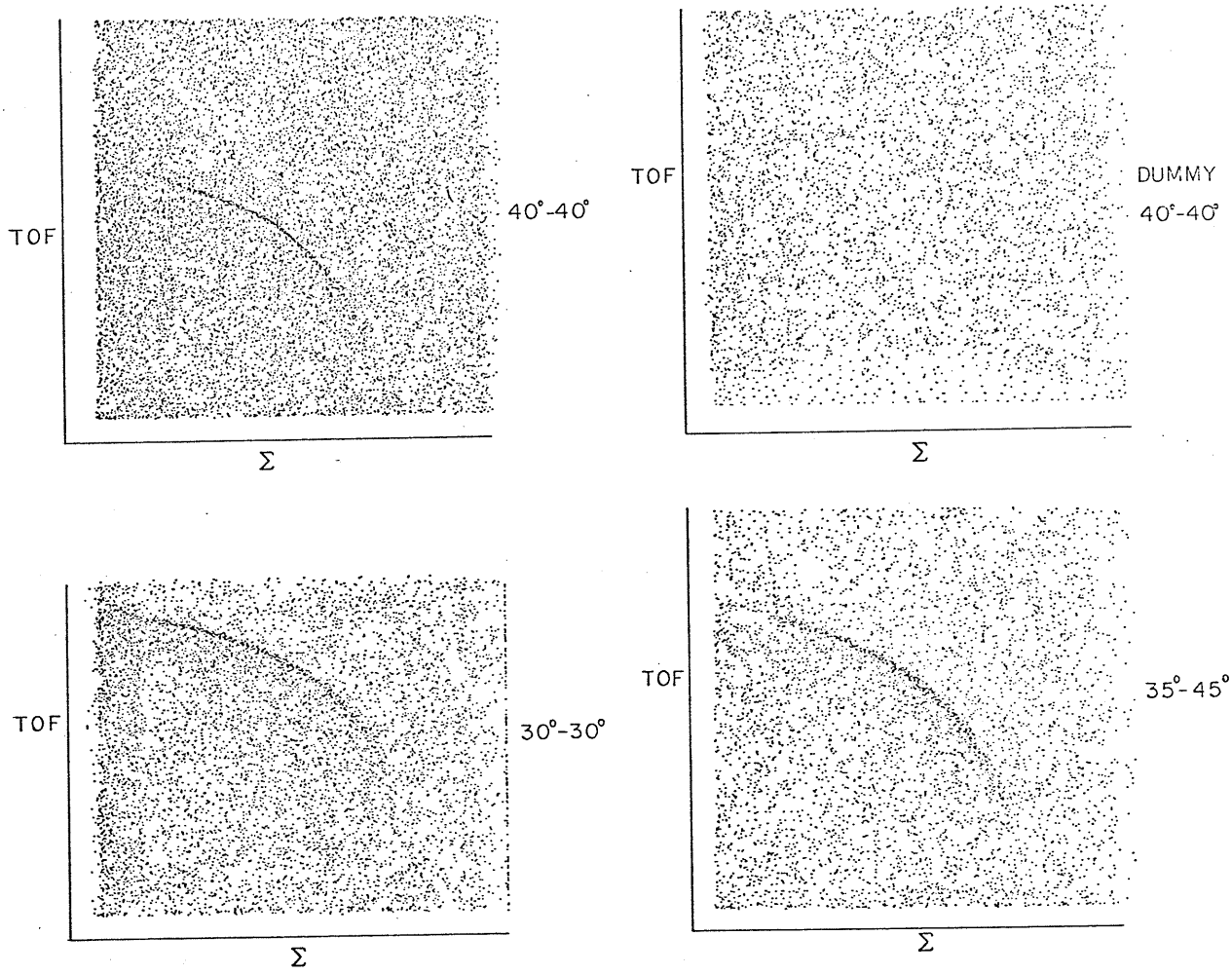

Figure 3.1.6 Some $^{3}H(p,pn)$ Random Subtracted Scatter Plots

Scatter plots are shown for (p,pn) on the tritiated target (top left) and dummy targets (top right) at 40^{o}-40^{o} and for $^{3}H(p,pn)$ at 30^{o}-30^{o} and 35^{o}-45^{o} (bottom).

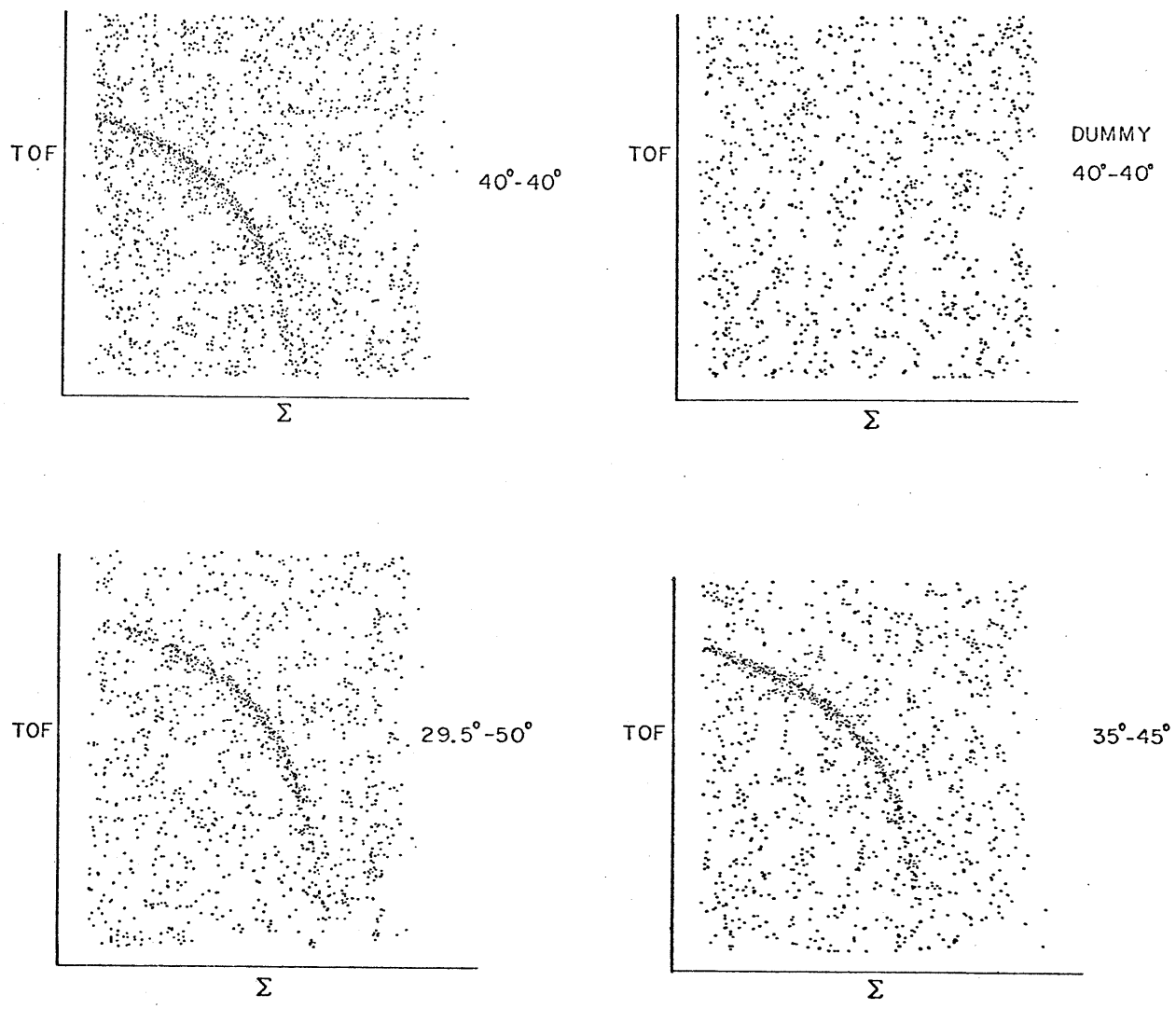

Figure 3.1.7 Some $^{3}H(p,dn)p$ Random Subtracted Scatter Plots

Top: Scatter plots for (p,pn) on the tritiated and dummy targets at 40^{o}-40^{o}.
Bottom: Scatter plots for $^{3}H(p,pn)$ at 29.5^{o}-50^{o} and 35^{o}-45^{o}.

display. Loci 2 MeV apart bounded the data accepted for $^3H(p,pn)d$ and $^3H(p,pn)d^*$, but the width varied from 2 to 3 MeV for the $^3H(p,dn)p$ data. The charged particle energy axis was divided into bins (decomposing the scatter plots into columns), and the number of events lying between the bounds in each column was counted and put into the appropriate bin. The resulting histogram is called a projected spectrum, since this operation is equivalent to projecting the events onto an axis. This process, illustrated in Figure 3.1.8, was repeated for all the real and random data. The net number of counts in each bin for the nuclear reaction is obtained by subtracting the random spectrum from the real spectrum. However, these random-subtracted spectra will still contain a contribution from Sc and Al real events. These may be eliminated by subtracting projected spectra for the dummy target from projected spectra for the tritiated target, being sure to normalize the number of counts in each bin for the dummy target to the same Faraday cup count as used for the tritiated target. The resultant spectrum is called dummy-subtracted. The dummy subtraction process may be performed on a real projection, random projection, or random-subtracted spectrum. For the latter case, the result is then dummy- and random-subtracted.

With a similar technique, a series of Q-value intervals was created automatically using the calibrations which were obtained as described above. A histogram was produced showing the number of events in each interval versus the Q-value. From these Q-value spectra it was determined that a 2 MeV wide locus

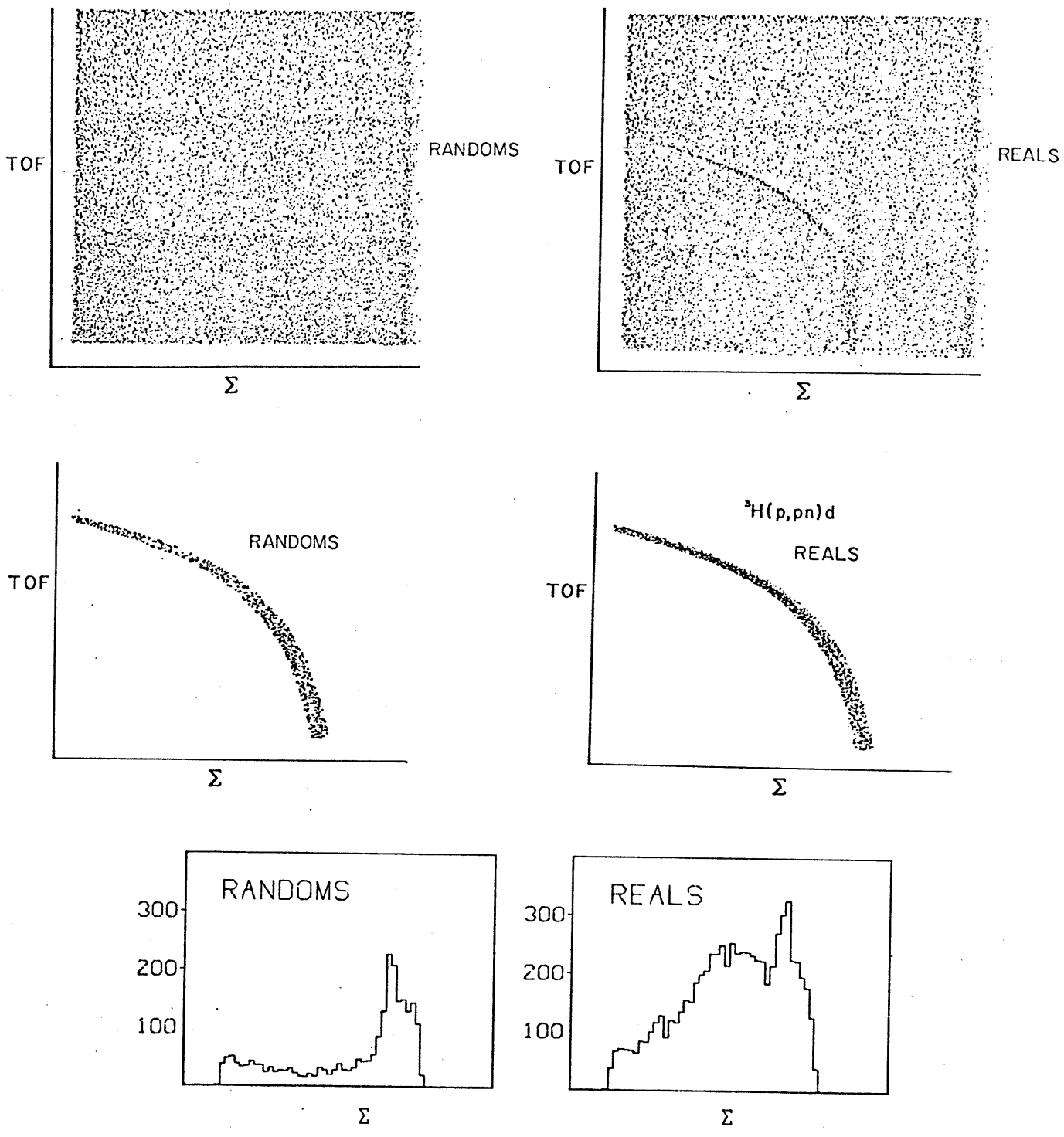

Figure 3.1.8 Method of Obtaining Projected Spectra

Top: Scatter plots show raw data for 'reals' and 'randoms'

Middle: Those events within a 2 MeV wide band are chosen.

Bottom: These selected events are projected onto the Σ axis.

was sufficient to accept most of the events within a kinematic band. Such spectra are also useful to compare the relative strengths of the d and d* final states, since they are a sum over all allowed proton energies (the phase space probability is almost the same for the two processes so no important correction need be made). Because of the larger number of events within each bin, it is simpler to perform dummy subtraction and retain statistical significance. One of the problems with the projected spectra is that there are relatively few counts in each channel for the $^{3}H(p,pn)d^{*}$ spectra and in the tails of the peak for the $^{3}H(p,pn)d$ spectra. Thus dummy subtraction can cause wild fluctuations because a small number is subtracted from a small number. Q-value spectra may also be random- and/or dummy-subtracted.

A few of the (p,dn) loci were drawn by hand because of the large discriminator walk that was evident in the TOF versus SIGMA loci. In fact, this was the technique used in all previous analyses of (p,pn) data at this laboratory. However, it could not be used for the present (p,pn) experiment since one of its objectives was to analyse spectra with a d* in the final state and these loci were not visible on the display, so no bounds could be accurately drawn by hand around the appropriate kinematic region. Also, automatic generation of the loci has the advantage of uniformity, meaning that spectra for different angles and different reactions are directly compatible. However, because of the characteristics of energy resolution in a TOF system, it suffers from the disadvantage

that the bounds are too far apart for high energy protons, while being barely large enough for low energy protons.

It may be seen from the scatter plots that the distribution of background is random in TOF-SIGMA space, but loci are generated in energy space to make the results compatible with those from the $^3H(p,2p)$, $^3H(p,pd)$, $^3H(p,2p)$, and $^3H(p,pd)$ experiments (B71,B72,T74) performed in this laboratory. Thus many more random events are accepted than would be the case if the loci were drawn by hand. For some runs and some angles, a loci width smaller than 2 MeV could be used, but in the interests of uniformity no change was made.

Once the projections were obtained, the bin width was increased so that the 42 MeV full scale was divided into 32 or 16 bins. The smaller the number of bins, the better the statistical significance of the contents. The energy at the centre of each bin was corrected for energy loss of the proton or deuteron in the aluminum, tritium, scandium, and Kapton foil. The number of counts in each bin was multiplied by the appropriate factors to include various corrections. The factor used to account for loss of neutron flux in the rupture shielding and air is

$$e^{-\sum_i n_i \sigma_i x_i}$$

where σ_i is the total cross section for the ith material and n_i is its density. x_i is the distance traversed through each material. The index i included nitrogen, oxygen, and aluminum. This correction was typically less than 12%. The factor accounting for pile-up in the charged particle detector is

S/(S-P) where S is the singles counting rate and P the pile-up rate. Deadtime correction was already applied because the live time Faraday cup was used. Error bars were generated from the statistical error associated with the reals - randoms counts:

$$\frac{\sqrt{reals + rands_1 + rands_2}}{reals + rands_1 - rands_2}$$

where 'reals+rands$_1$' is the number of counts associated with a real event and 'rands$_2$' is associated with an event flagged as random. The statistical error due to dummy target subtraction has not been included.

Section 3.2 Uncertainties

The formula for statistical uncertainties associated with random-subtracted coincidence data has been presented in Section 3.1. This is a relative error and is typically 5% for $^{3}H(p,pn)d$, and 10% for $^{3}H(p,pn)d^{*}$ and $^{3}H(p,dn)p$. These percentages do not include the statistical error due to dummy subtraction, but 'reals-randoms' for the dummy target is many times smaller than 'randoms' for the tritiated target and so no significant alteration in the error estimate should be necessary.

There are also a variety of contributions to uncertainties in absolute cross sections that must be considered. These are summarized in Table IV.

Table IV

Absolute Cross Section Uncertainties

Source of Uncertainty	Percent Contribution to Absolute Cross Section Uncertainty
Tritium target thickness	5
Solid angles	2
Neutron detector efficiency code	6
Neutron detector pulse height threshold	5
Loss of incident beam	3
Charge integration	1
Pile-up, dead-time, neutron attenuation	7

The components of the tritium target thickness uncertainty

are shown in Table III. Because the tritium content is only 21% of the estimate made by the supplier, Oak Ridge National Laboratories, this factor deserves detailed consideration. Tritium content was monitored during the experiment and was found to be consistent to within 5%. Another group has also discovered that their tritiated target (from the same supplier) was much weaker than the content quoted by the manufacturer. An additional complication was created by our ordering a target with an unusual composition, ^{3}H in Sc deposited on Al, rather than the more standard ^{3}H in Ti on Cu.

The charged particle collimator was studied in detail with a travelling microscope, while the distance of the neutron detector from the target was measured to the middle of the scintillators using a standard tape measure. The neutron efficiency code is thought to be accurate to within 6% including double scattering corrections, but no test on our detectors has been performed to compare the efficiency predictions with experiment. Perhaps a more serious problem is the error in neutron efficiency induced by uncertainties in the pulse height threshold for neutron detection. The possible error in choosing the correct position of the Compton edge for calibration gamma rays, combined with certain drifts in the electronic system (particularly during the first run), could cause an uncertainty in threshold of typically 100 keV. This would produce an error in the efficiency ranging from 9% for 5 MeV neutrons to 2% for 35 MeV neutrons. It is not known how much of the incident proton beam was not collected by the

Faraday cup, but calculations estimated it to be of the order of one percent. There is no provision in the scattering chamber for accurately aligned monitor detectors to provide a continuing assessment of beam quality (principally by recording changes in left-right symmetry for elastically scattered protons). However, beam optics were always arranged so that the beam was on axis through the quadrupole doublets and hence "non-steering" at the target and other important positions along the beamline. Since time-of-flight spectra referenced to the RF did not reveal gamma rays originating from collisions of the beam with the beampipe, a pessimistic estimate of beam loss might be several percent. The charge integrator has been tested several times and found to be reliable to within 1%. There is an additional uncertainty due to the production of ^{3}He in the target by the decay of ^{3}H. It is not known if the ^{3}He was evolved from the target or contributed several percent to the (p,pn) spectra.

There were also several factors used to correct the data for various effects. The dead-time correction was measured by comparing the number of real-time counts scaled directly from the charge integrator with the number of live-time counts accepted by the computer and ADCs. Since the computer had a large dead-time, at least 30 microseconds for every event, the live-time correction for the computer should greatly exceed the sub-microsecond dead-time correction for the TACs and SCAs. The dead-time correction was typically .2%. No pile-up monitor was used for the neutron detectors because the fast gating

requirement eliminated all but a negligible probability of pile-up. A pile-up gate with a 3 microsecond resolving time was used with the signals from the charged particle detectors. This was approximately the length of the linear pulses. The pile-up correction was typically 5%. The total cross sections used in the neutron attenuation calculation were taken from Fo71 and were assumed to be constant over the whole range of neutron energies studied. Since total cross sections were used, the calculation overestimates the neutron attenuation because neutrons scattered at small angles still reach the detector. Also, these total cross sections are only known (to be constant) over the range 10 to 15 MeV. This correction was typically 12%. The possible error in these corrections create an uncertainty of 7% in the coincidence cross section. The absolute cross section uncertainty is most evident for an angle pair studied in the first run which was repeated in the third run. There is a 20% normalization disagreement between the two spectra. The difference is consistent with the estimates of the error tabulated above.

Chapter 4

RESULTS

Section 4.1 Trion Wavefunctions

Several wavefunctions have been used to represent the three-nucleon bound state. Because of the increased complexity in extracting the wavefunctions from experimental data using hadrons as projectiles on trions, it has been common practice to use electron scattering data. As mentioned in Section 1.2, electron-induced trion disintegration data has been used in some cases, but these reactions still involve hadronic final state interactions which will distort the results. Thus, electron elastic scattering data provides some of the most reliable information on the structure of the trion. Only knowledge of the electromagnetic properties can be determined, but this should be sufficient to distinguish between nuclear wavefunctions to select the better representations. One should remember, however, that whereas electron scattering ($q > 100$ MeV/c) probes deeper into the nucleus, (p,pn) investigates only the surface regions. Consequently, wavefunctions that fit electron scattering data may not be good functions for our purposes, and vice versa. There are two distinct parameters of interest, the charge and magnetic form factors; the former are generally better defined experimentally and thus of more use. The charge form factor is defined as

$$F(q^2) = \frac{1}{Ze} \int \rho(\vec{r}) e^{i \vec{q} \cdot \vec{r}} d\vec{r} \qquad \rho = \text{charge density}$$

The charge form factors for ^3H and ^3He are shown in Figures 4.1.1 and 4.1.2 respectively, with the data from Collard et al (C65). The data are approximately linear in q^2. The slope is proportional (as may be seen by expanding the above exponent in a Taylor series) to the mean square charge radius, and is larger in magnitude for ^3He than ^3H (because of Coulomb repulsion between the protons, and because a neutron and proton form a quasi-deuteron in the trion leaving the extra particle to be weakly bound). One of the most popular trion wavefunctions has been the Irving-Gunn function (G51)

$$\psi(\vec{r}_1,\vec{r}_2,\vec{r}_3) = \frac{A e^{-\frac{1}{2}\alpha(r_{12}^2+r_{23}^2+r_{13}^2)^{1/2}}}{(r_{12}^2+r_{23}^2+r_{13}^2)^{1/2}}$$

$$A = \frac{3^{1/4}\alpha^2}{\sqrt{2}\,\pi^{3/2}} \qquad \vec{r}_{ij} = \vec{r}_i - \vec{r}_j$$

The parameter α has often been chosen to be 1.00 fm^{-1} for ^3H (G51) and .77 fm^{-1} for ^3He (B64). The solid curves in both figures represent these values while the dashed curves, which are closer to the data, were generated using the values .89 and .82 fm^{-1} for ^3H and ^3He respectively. Tin et al (T74) were able to deduce some of these results from $^3H(p,2p)nn$ data directly. The equation

$$F_B(q^2) = \frac{864}{(2q/\alpha)^4}\left\{1 - \frac{1+\frac{1}{2}(2q/\alpha)^2}{[1+\frac{1}{8}(2q/\alpha)^2]^{3/2}}\right\}$$

from B64 was used to generate these curves. The dot-dash curves represent the wavefunction

$$\psi(\vec{r}_1,\vec{r}_2,\vec{r}_3) = A e^{-R/2\,(r_{12}+r_{23}+r_{13})} \qquad A = \sqrt{\tfrac{4}{3}}\,\chi^3$$

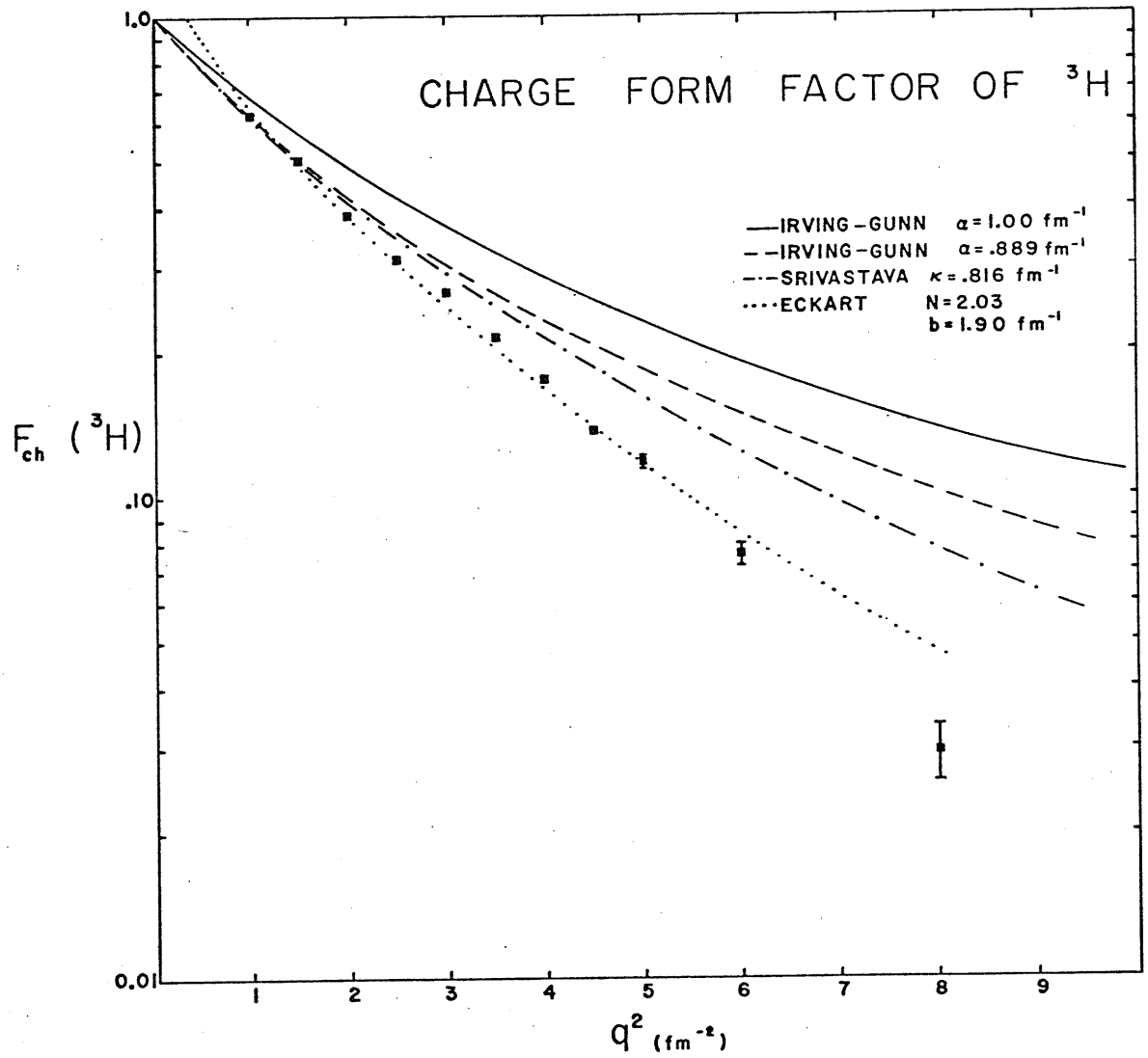

Figure 4.1.1 Charge Form Factor for ^3H
The predictions of various wavefunctions are compared with experiment.
The data are from Collard et al

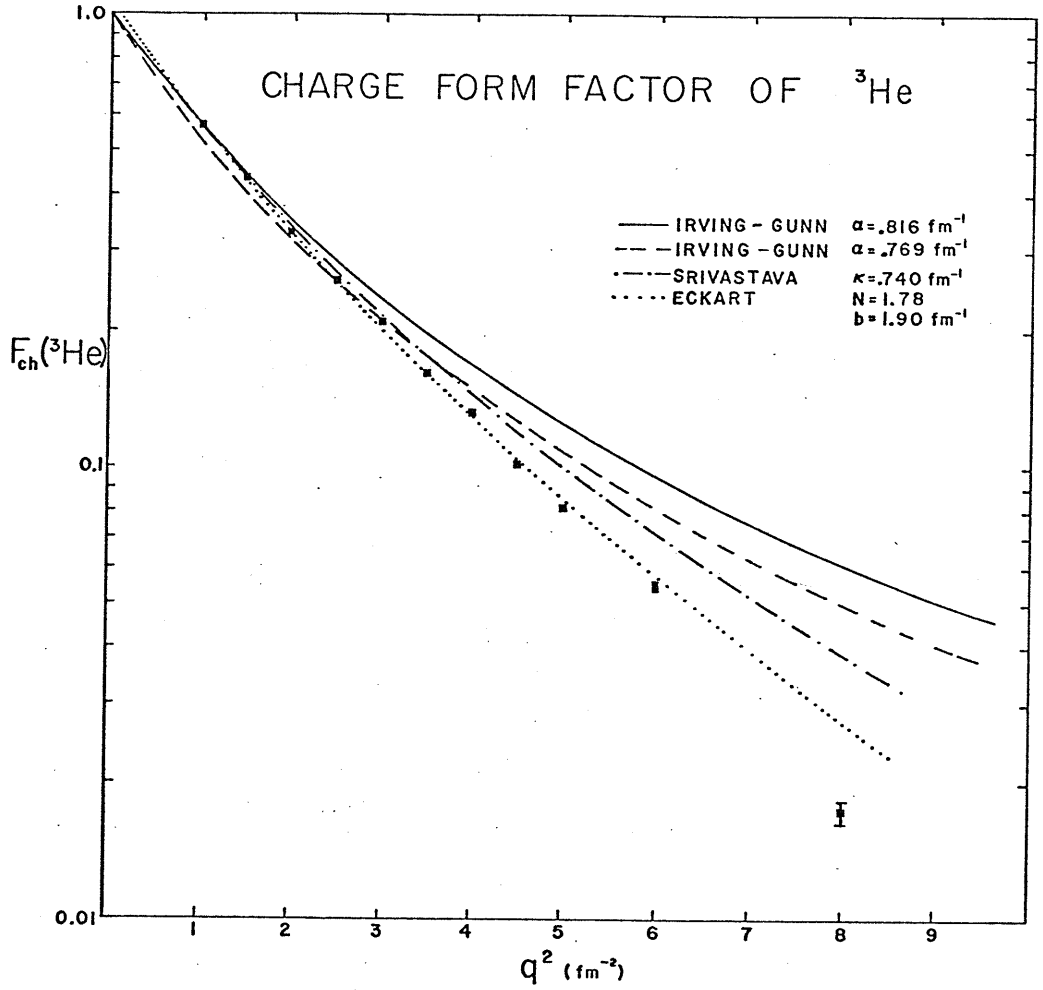

Figure 4.1.2 Charge Form Factor for ^{3}He
The predictions of various wavefunctions are compared with experiment.
The data are from Collard et al.

with a value for κ of .816 for ^3H and .74 fm^{-1} for ^3He. The curve was created using the numerical results of Srivastava (S64). The generation of the three types of curves also required the use of the equations (C65)

$$F_{ch}(^3H) = [F_{ch}(p) + 2F_{ch}(n)] \cdot F_B(q^2)$$

$$F_{ch}(^3He) = [F_{ch}(p) + \tfrac{1}{2}F_{ch}(n)] \cdot F_B(q^2)$$

where $F_{ch}(^3H)$ and $F_{ch}(^3He)$ are the charge form factors for ^3H and ^3He while $F_{ch}(n)$ and $F_{ch}(p)$ are the charge form factors for neutrons and protons. The latter numbers were obtained from S64. $F_B(q^2)$ is the body form factor and is related to the charge density for point-like nucleons.

$$F_B(q^2) = \int e^{i\vec{q}\cdot\vec{r}} |\Phi(\vec{r})|^2 d\vec{r}$$

An alternative approach is to explicitly include a deuteron function Φ_d in the trion wavefunction

$$\Psi(\vec{r}_1, \vec{r}_2, \vec{r}_3) = u(\vec{r}_{1-23})\Phi_d(\vec{r}_{23}) \qquad \vec{r}_{1-23} = \vec{r}_{13} - \frac{\vec{r}_{23}}{2}$$

The deuteron function is arbitrary at the moment but an often used version is the Hulthen wavefunction (H57)

$$\Phi_d(\vec{r}) = B\left(\frac{e^{-ar} - e^{-br}}{r}\right)$$

The dotted curves in Figures 4.1.1 and 4.1.2 were generated using the Eckart function (Li73)

$$u(r) = N\sqrt{\frac{\alpha}{2\pi}}\,\frac{e^{-\alpha r}}{r}\left(1 - e^{-br}\right)^4$$

$\alpha = \sqrt{4MS/3}$ where M is the nucleon mass, S is the nucleon (neutron for ^3H and proton for ^3He) separation energy, N is the

normalization factor, 2.03 for ^3H and 1.78 for ^3He, b is the shape parameter, 1.90 fm^{-1} for both nuclei, and the following relations hold:

$$F_{ch}(^3H) = F_{ch}(^2H) \cdot \int e^{i\vec{q}\cdot\vec{r}/3} |u(r)|^2 d\vec{r} + F_{ch}(n) \cdot \int e^{i2\vec{q}\cdot\vec{r}/3} |u(r)|^2 d\vec{r}$$

$$F_{ch}(^3He) = \frac{1}{2}\left\{ F_{ch}(^2H) \cdot \int e^{i\vec{q}\cdot\vec{r}/3} |u(r)|^2 d\vec{r} + F_{ch}(p) \cdot \int e^{i2\vec{q}\cdot\vec{r}/3} |u(r)|^2 d\vec{r} \right\}$$

The deuteron charge form factors $F_{ch}(^2H)$ were obtained from D62. With these parameters, the momentum distribution for ^3H has a half width of 54 MeV/c, which is comparable to the widths obtained using various overlaps as shown in Table I (the effective width generated by the attenuation model is smaller, namely about 42 MeV/c). Eckart functions themselves are not normalized to unity as were the previous two functions, but are normalized to fit the electron scattering data. The values of N required to fit the electron data represent an overnormalization (total probability greater than 100%), since the standard unity normalization yields values of N=1.77 and 1.72 for ^3H and ^3He (i.e. 15% excess for ^3H and 3% for ^3He). The deuteron wavefunction is taken to have a normalization of unity (that is, there is a 100% probability of finding a deuteron in a trion). This form is meaningful only near a deuteron pole in the reaction mechanism. One notices that the Eckart function fit has the unwholesome characteristic of having a charge form factor greater than unity at zero momentum transfer (because of the overnormalization). Presumably it would deviate from the elastic scattering data in this region if the latter existed. If the value of the exponent were one in the Eckart function, a Hulthen function would result. Whereas the Hulthen wavefunc-

tion attains a nonzero value at the origin (in configuration space), the Eckart function exhibits a repulsive core behavior and is zero. One notices that all of the functions seem to fit ^{3}He electron data better than ^{3}H data. This might be due to a complex internal structure of ^{3}H or merely due to incorrect values of $F_{ch}(n)$, since ^{3}H emphasizes this parameter to a greater extent than ^{3}He. $F_{ch}(n)$ is very poorly defined experimentally, but was chosen as $F_{ch}(n) = .021q^2$ (S64). The role of the neutron charge form factor in electron scattering from the three-nucleon system has been examined in some detail by Brandenburg and Sauer (B75). It is also possible that the ^{3}H data themselves are incorrect.

As far as the impulse approximation is concerned, the quantity of interest is the Fourier transform of the overlap integral between the spatial wavefunctions of the target and the residual nuclei. For the Irving-Gunn trion wavefunction and Hulthen deuteron wavefunction this is (G64)

$$\Phi(\vec{q}) = \frac{1}{(2\pi\hbar)^{3/2}} \int e^{i\vec{q}\cdot\vec{r}}\, d\vec{r} \int d\vec{\rho}\; \frac{A e^{-\frac{1}{2}\alpha(2r^2+\frac{3}{2}\rho^2)^{1/2}}}{(2r^2+\frac{3}{2}\rho^2)^{1/2}}\; B\left(\frac{e^{-a\rho}-e^{-b\rho}}{\rho}\right)$$

$$= \frac{256}{(2\pi\hbar)^{3/2}}\; \frac{\pi^{3/2}(b^2-a^2)AB}{\sqrt{3}\,\alpha^5} \int \frac{k^2\,dk}{(a^2+k^2)(b^2+k^2)\left[1+\frac{8k^2}{3\alpha^2}+\frac{2q^2}{\alpha^2}\right]^{5/2}}$$

There is no simple analytic expression for the Irving-Gunn-Hulthen overlap or the Srivastava exponential wavefunction. However, the result for the Eckart function

$$\Phi(\vec{q}) = \frac{1}{(2\pi\hbar)^{3/2}} \int d\vec{r}\, e^{i\vec{q}\cdot\vec{r}}\, N\sqrt{\frac{\alpha}{2\pi}}\; \frac{e^{-\alpha r}}{r}\,(1-e^{-br})^4$$

$$= \frac{4\pi N\sqrt{\frac{\alpha}{2\pi}}}{(2\pi\hbar)^{3/2}} \left\{ \frac{1}{q^2+\alpha^2} - \frac{4}{q^2+(\alpha+b)^2} + \frac{6}{q^2+(\alpha+2b)^2} - \frac{4}{q^2+(\alpha+3b)^2} + \frac{1}{q^2+(\alpha+4b)^2} \right\}$$

is particularly simple and this means that computer programmes using it are more efficient. The Eckart function behaves asymptotically as

$$\lim_{r \to \infty} u(r) = K \frac{e^{-\alpha r}}{r}$$

and this is the character predicted by elementary Quantum Mechanics for a body outside a potential well. According to Lehman (L72), two characteristics are necessary to fit trion breakup data: 1) factorizability into deuteron times n-d wavefunction, and 2) the above asymptotic behavior. Both of these properties are present in the Eckart representation. Five percent changes in the parameters for the above wavefunctions noticeably spoiled the quality of the fit to the electron scattering data. However, such changes generally changed the momentum wavefunction by an amount which is almost undetectable when compared to our coincidence cross section data.

Section 4.2 Two-Body Cross Sections

As was mentioned in Section 1.3, there exists an ambiguity in the choice of energies at which to evaluate the two-body cross section used in the impulse approximation. The "prior prescription" is evaluated using the on-shell cross section at the relative momentum (p) of the two bodies before the reaction occurred, while the "post prescription" is evaluated at their relative momentum (k) after the collision. There is some evidence (M69) from the Faddeev equations to indicate that the latter form should be more reliable. Both methods use the same scattering angle

$$\theta = \cos^{-1}\left[\frac{P_1 P_3 \cos\theta_3 - E_1 E_3 + E_{1cm} E_{3cm}}{P_{1cm}\, P_{3cm}}\right]$$

where 'cm' refers to quantities measured in the centre of mass system of particles 3 and 4. The triple differential cross sections evaluated using the two approximations differ in magnitude and shape (T74). A form having a firmer theoretical justification is the half-off-the-energy-shell t-matrix approximation (Y54)

$$t(p^2, k^2, k^2+i\epsilon) = \frac{1}{p^2+\beta^2} \quad \frac{1}{k^2+\beta^2} \quad \frac{\lambda(k+i\beta)}{(k-i\alpha)(k-i\gamma)}$$

This t-matrix is separable into initial and final momenta and is s-wave (no angular dependence). The energy (k^2) is chosen to correspond to the final state momentum in accordance with the results of Meboniya (M69). Because $p \neq k$ (they differ by less than .4% for $^3H(p,pn)$ at 45 MeV), the cross section is called off-shell.

Figure 4.2.1 shows differential n-p cross section data from several sources (A75) along with three different parametrizations. One parametrization is due to Gammel (Ga60) and is symmetric about 90°. A more recent formulation, due to Binstock (B74) and based on a phase shift analysis, is considerably more complex, but yields only marginally better results. The half-off-shell results are also shown and are made anisotropic by combining the angular dependence of Gammel's parametrization with the 90° energy dependence from Yamaguchi's work (Y54)

$$\frac{d\sigma}{d\Omega} = \frac{10}{4}\left\{|t_{singlet}|^2 + 3|t_{triplet}|^2\right\}\left\{1 + 2\left(\frac{E_{lab}}{90}\right)^2 \cos^2\theta\right\}$$

The parameters used were

$\alpha_{singlet} = -.0401\ fm^{-1}$ $\alpha_{triplet} = .2316\ fm^{-1}$ $\gamma = 2\beta - \alpha$

$\beta_{singlet} = 1.177\ fm^{-1}$ $\beta_{triplet} = 1.415\ fm^{-1}$ $\lambda = 2\beta(\alpha+\beta)^2$

and were obtained from Ebenhoh (E72). This calculation showed that the triplet provided more than 6 times the singlet contribution to the scattering. Typically, an angular range of 60°-120° and an effective incident neutron energy of 20-40 MeV was required for the SIA, although larger ranges were used for the more extreme angles of 50°-50° and 56°-56°.

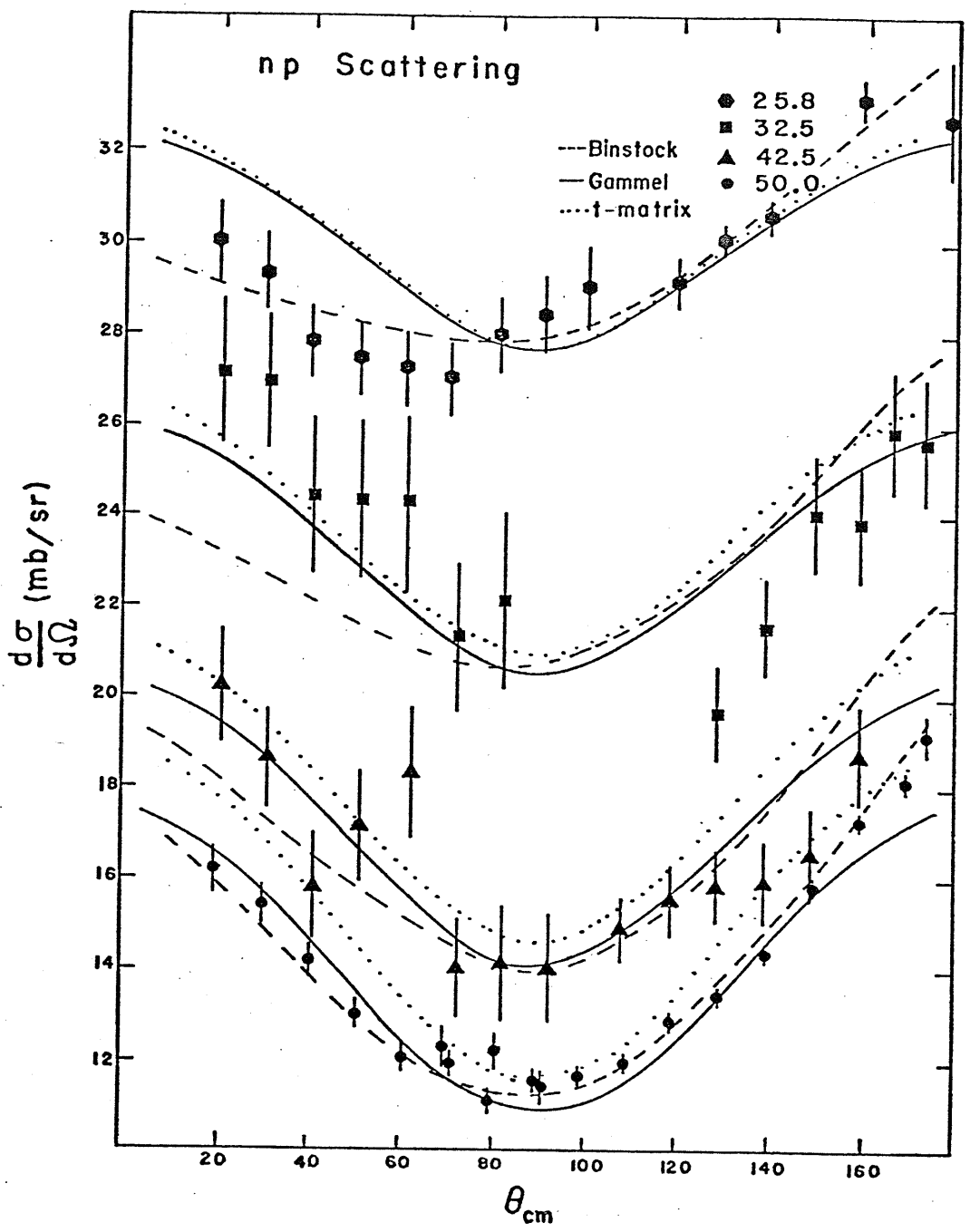

Figure 4.2.1 n-p Differential Cross Sections

Experimental results at 25.8, 32.5, 42.5, and 50.0 MeV are compared with the Binstock, Gammel, and t-matrix parametrizations.

Section 4.3 Doublet Cross Sections

The attenuation model requires a knowledge of the n-d total cross sections in order to calculate the loss of flux from the (p,pn) reaction due to collisions with the spectator deuteron. The n-d relative wavefunction in the trion is S=1/2 (only the doublet interaction is present) and thus only doublet n-d cross sections should be used. No polarization data exists and so the only method of extracting the doublet cross sections is through a phase shift analysis of n-d data. Several such analyses exist, but the Arvieux (A74) results are most recent and provide a smooth doublet cross section. Figure 4.3.1 shows the total and doublet total cross section extracted from this phase shift analysis using the equations

$$\sigma_{\substack{doublet \\ quartet}} = \frac{\pi}{k_{rel}^2} \sum_{\ell}' (2\ell+1) \left[1 - |S_\ell|^2 + |1 - S_\ell|^2 \right]$$

$$= \frac{2\pi}{k_{rel}^2} \sum_{\ell}' (2\ell+1) \left[1 - \eta_\ell \cos 2\delta_\ell \right]$$

$$\sigma_{total} = \frac{1}{3} \left(\sigma_{doublet} + 2\,\sigma_{quartet} \right) \qquad S = S_{matrix} = \sum_{\ell}' S_\ell = \sum_{\ell}' \sqrt{\eta_\ell}\, e^{i\delta_\ell}$$

Partial waves up to L=8 were included. Experimental total cross sections from Seagrave's tabulation (S70) are compared with those predicted by the phase shift analysis. As far as the present (p,pn) experiment is concerned, the region from 10 to 30 MeV is most important. Figure 4.3.1 shows that the doublet total cross section decreases at low energy. This may be due in part to the inability of the phase shift analysis to fit the experimental total cross sections in this kinematic region, but other phase shift analyses demonstrate the same property. It seems unlikely that the predominant reason for

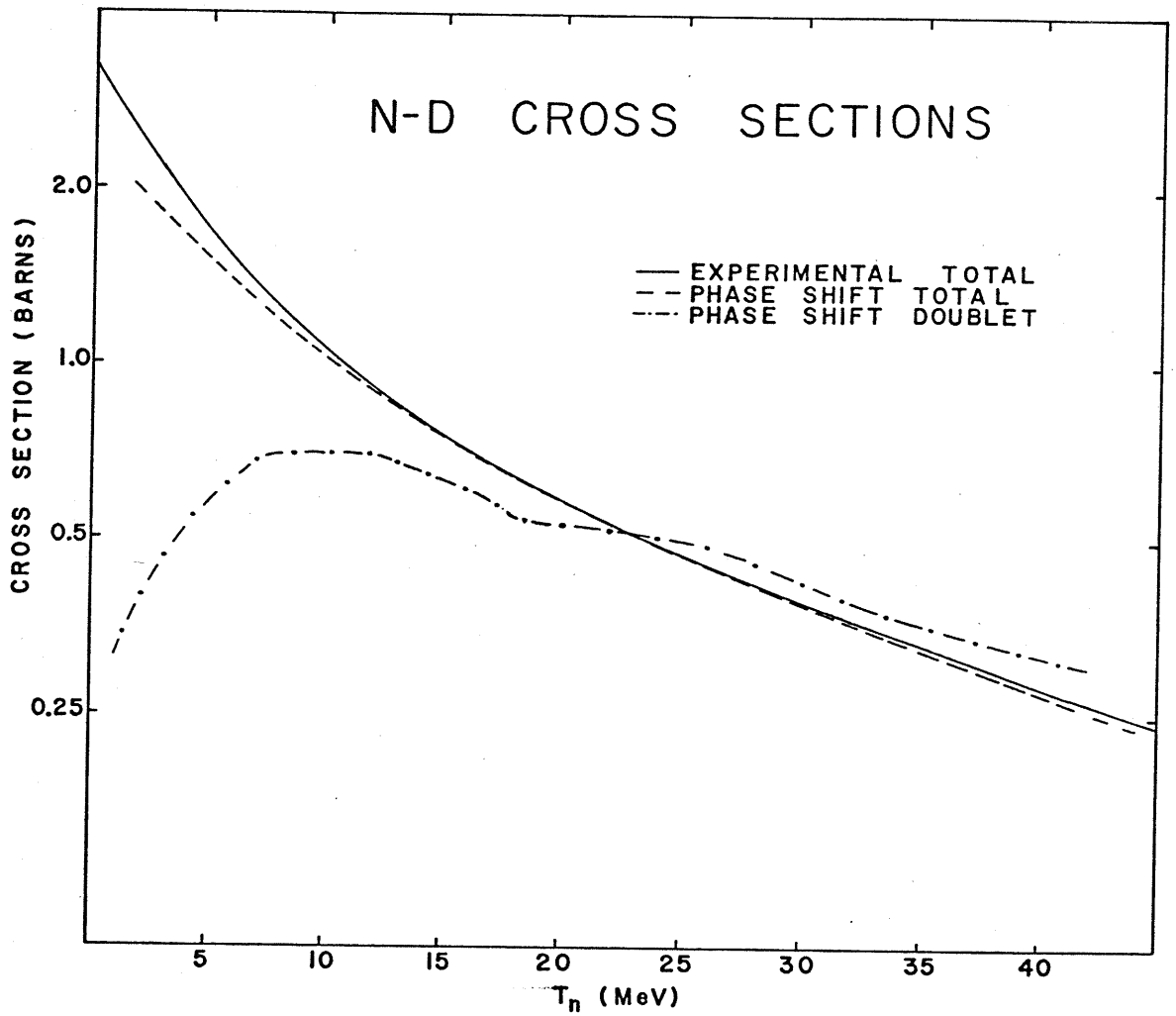

Figure 4.3.1 N-D Total Cross Sections
The N-D total cross section and doublet N-D total cross section are compared to experiment.

the low total cross section is an underestimation of only the doublet component, since the doublet contribution per spin state (i.e. ignoring the spin factors of 4 and 2) dominates for higher energy. Therefore, we shall assume that the doublet total cross sections do in fact decrease at low energy.

Section 4.4 Q-Value Spectra

A Q-value spectrum is sometimes called a missing mass spectrum. Increasing absolute value of the Q-value (or missing mass) corresponds to increasing invariant mass (or excitation) of the unobserved recoiling system (d* here). (Particle physicists were often unable to observe uncharged recoiling particles and plotted results as a function of the kinematically determined recoil mass, and hence the term missing mass.) Figure 4.4.1 displays Q-value spectra for real and random events for both the tritiated and dummy targets. It also reveals the effect of random and dummy subtraction. The improvement in resolution due to dummy subtraction is also studied in Figure 4.4.2. It appears that dummy subtraction is not really worthwhile; no significant benefits accrue from the time taken to duplicate the experiment on the dummy target. On the other hand, it is clear that random subtraction is able to substantially improve the resolution. Figures 4.4.3 and 4.4.4 show random-subtracted spectra for most of the angles considered. It is evident that a 2 MeV wide window (which accepts almost all of the $^{3}H(p,pn)d$ events) will put some of the d events into the d* projected spectra, as well as including some events from scandium. However, if the window were made smaller for the d* and not the d spectra, then cross sections for the two processes would not be comparable. The width of the d and d* states should be the same (experimentally) and so the d* state should also be 2 MeV wide, therefore no decrease in window width is possible. It may be seen from the spectra that

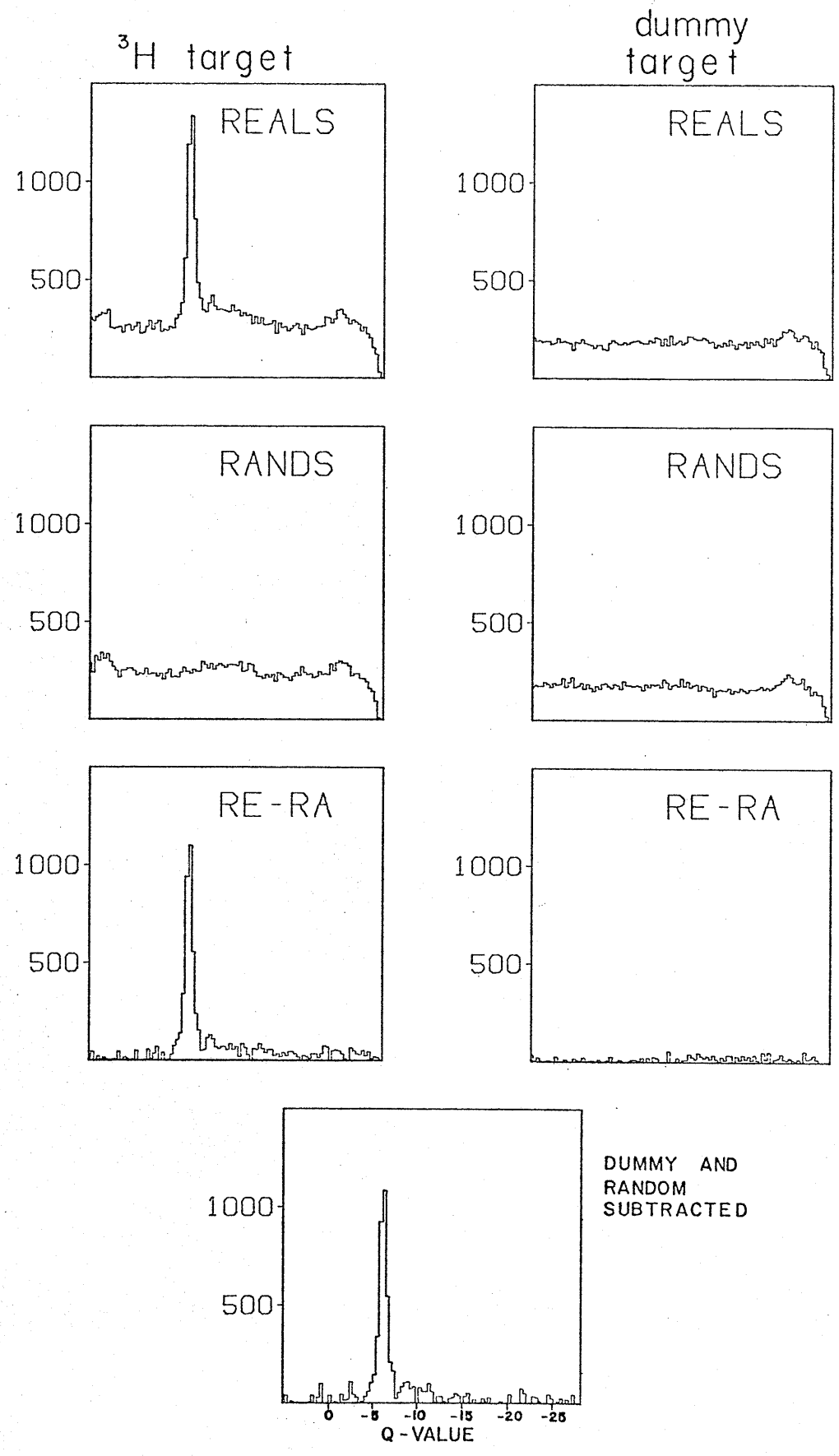

Figure 4.4.1 Q-Value Histograms Showing the Method of Performing Random- and Dummy Subtraction

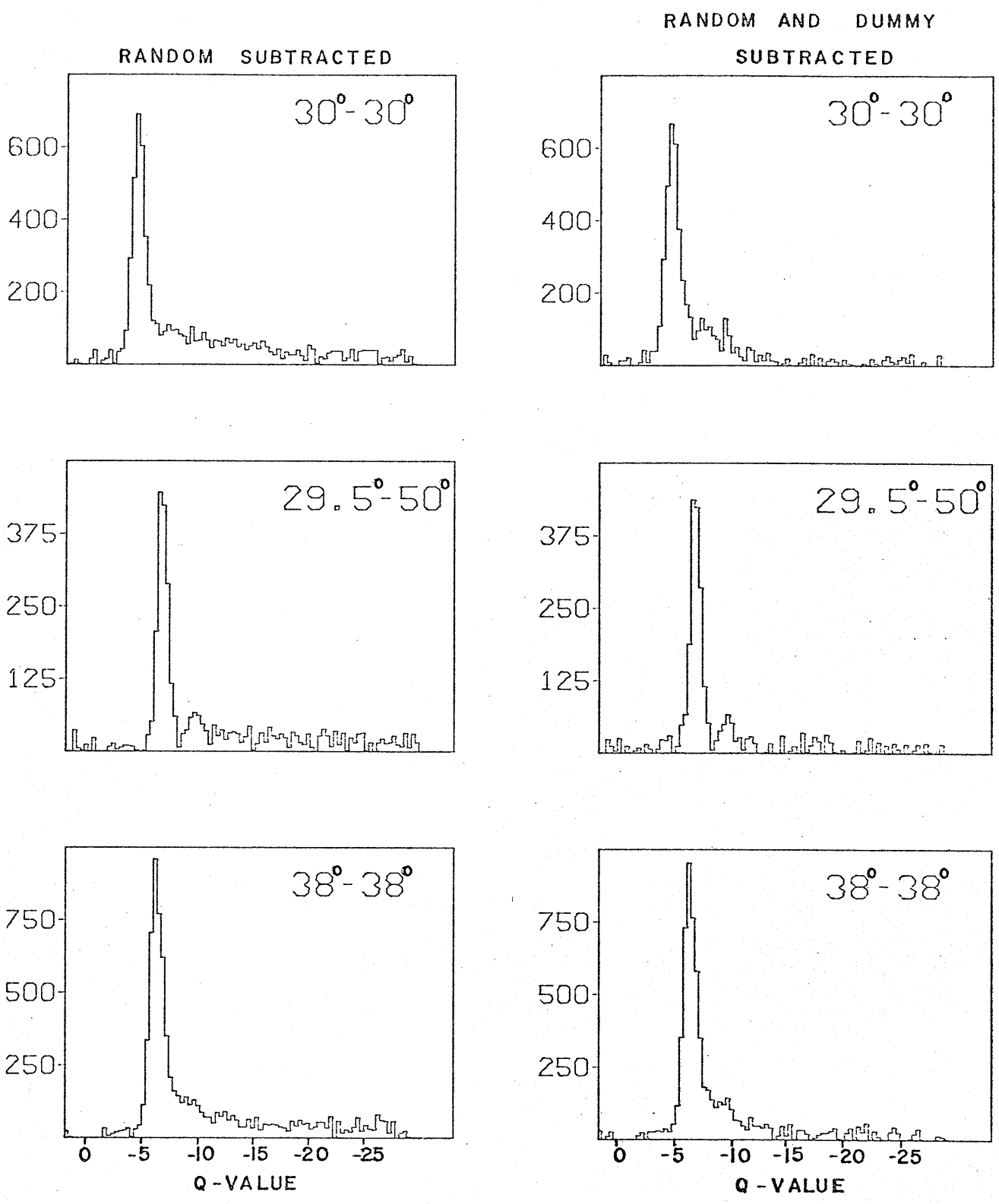

Figure 4.4.2 Q-Value Histograms Showing the Effect of Dummy Subtraction.

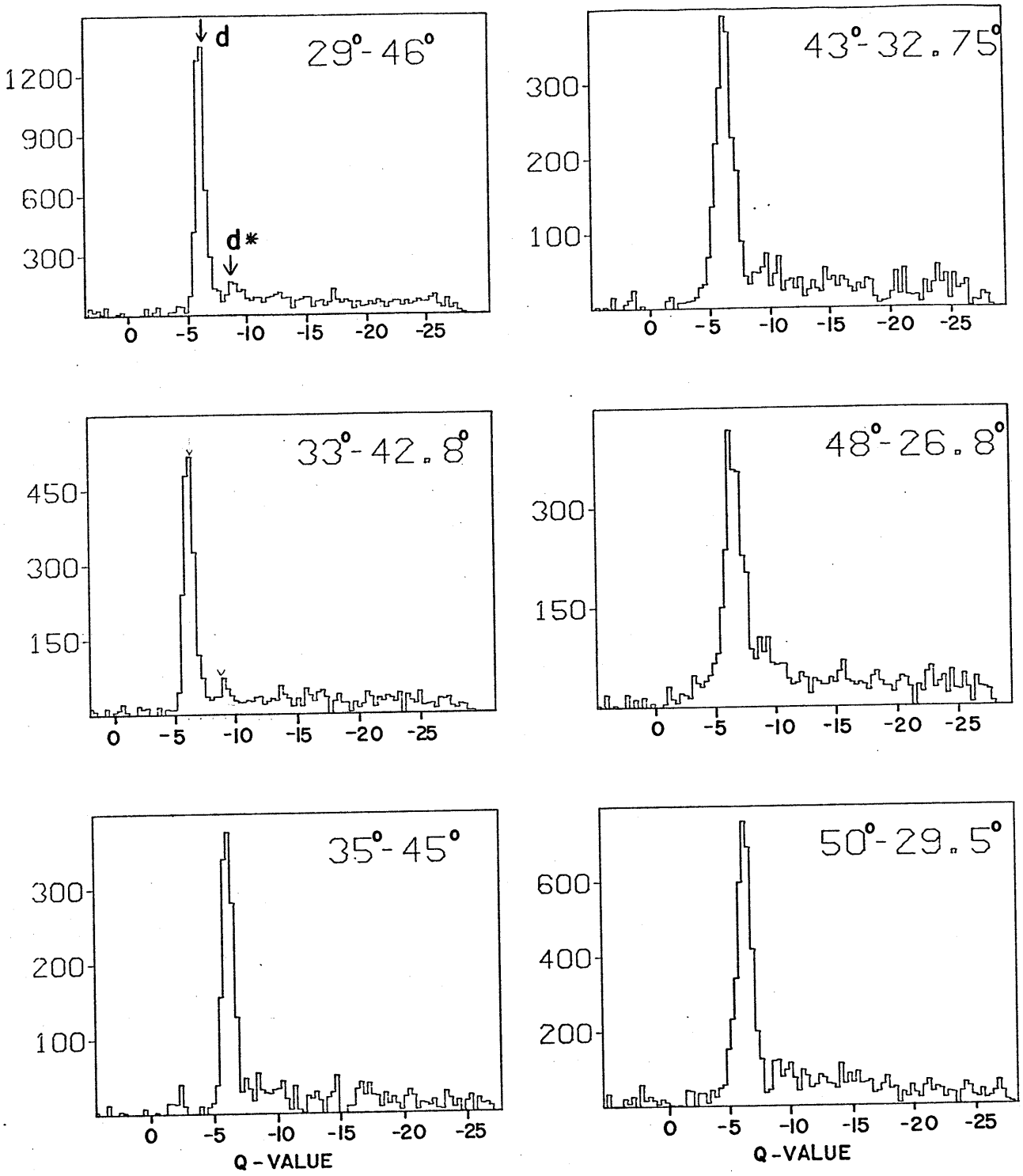

Figure 4.4.3 Q-Value Histograms

These data are random-subtracted but not dummy-subtracted.

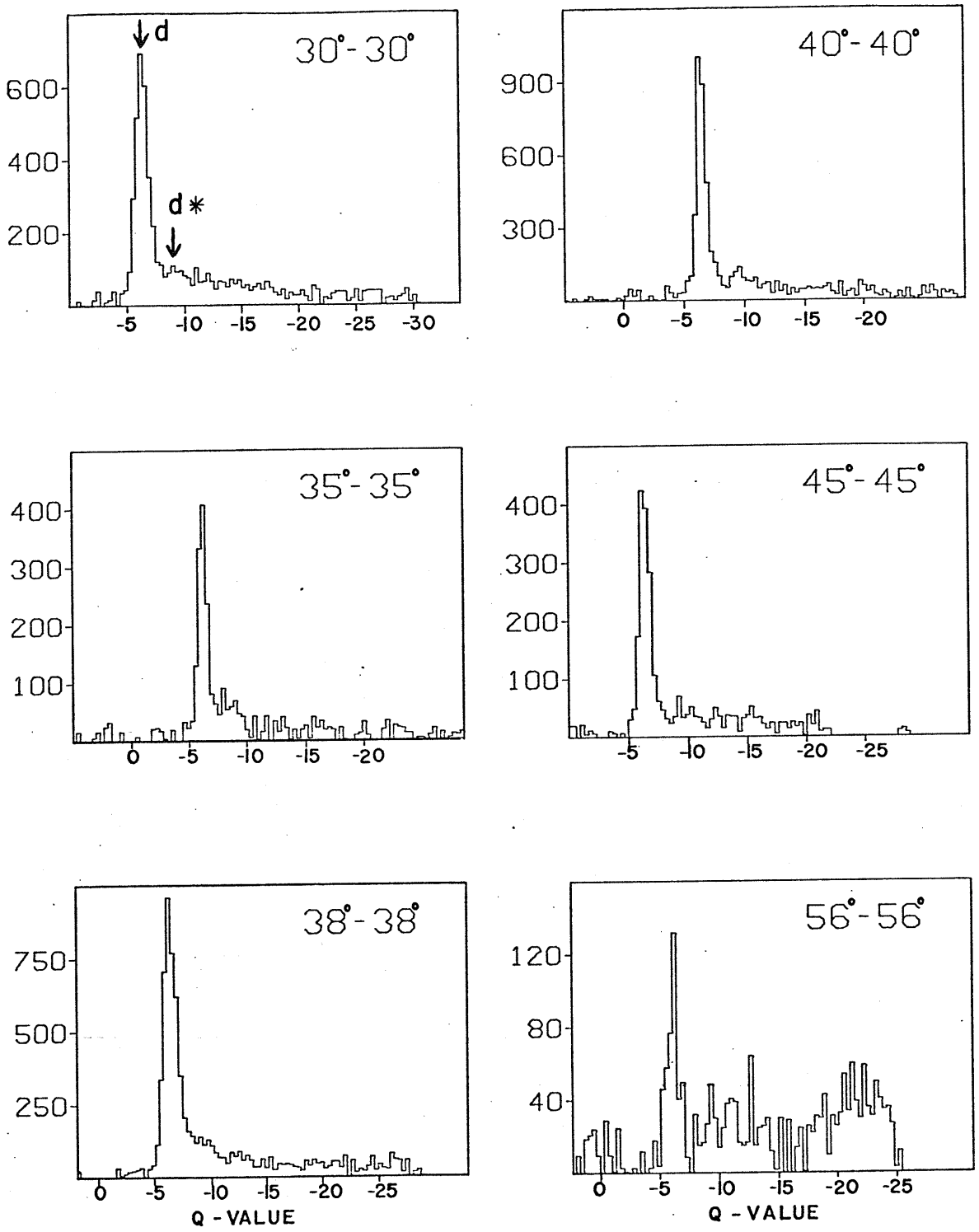

Figure 4.4.4 Q-Value Histograms

These data are random-subtracted but not dummy-subtracted.

the continuum representing four-body processes occurs to the right of the d* state. Enhancements due to the scandium and aluminum may also be seen in some of the spectra. The kinematic loci for (p,pn) on these materials run approximately parallel to a kinematic locus for ^{3}H(p,pn) for some values of Q, and will thus appear as enhancements in the histogram near the appropriate positions using the ^{3}H calibration labelling the horizontal axes. The Q-value resolution is actually better for the middle of the kinematic locus than for the entire locus, because the enhancement is stronger in the middle and the neutron timing is better than for areas of low charged particle energy. Figure 4.4.5 illustrates this effect.

In principle it is possible to use the Watson-Migdal (W52) formulation to fit the region around the d* peak in the missing mass spectrum and thus obtain a value for the n-p scattering length. In practice (T74), even for the better resolution provided in (p,2p) experiments, this method does not yield a reasonable value for this parameter because of the dominance of the QFS contribution to the peak.

It has been reported that the process p + ^{3}H $\rightarrow$ d* + d* has been observed at 55°-55° in the ^{3}H(p,2p) reaction (T74). No evidence for this process is visible for our data at 56°-56° in Figure 4.4.4, but this may be the result of poor statistics.

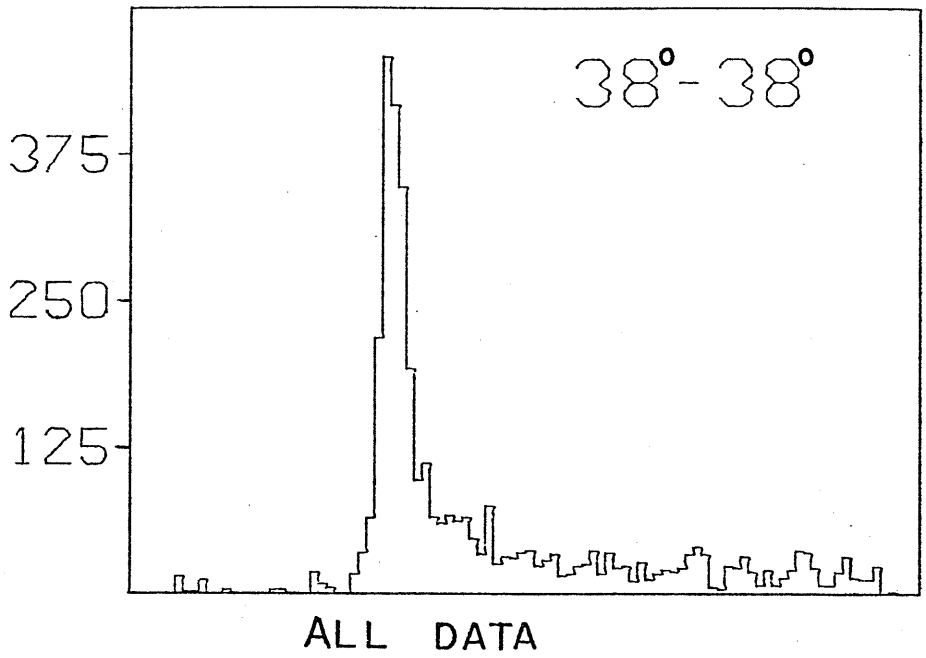

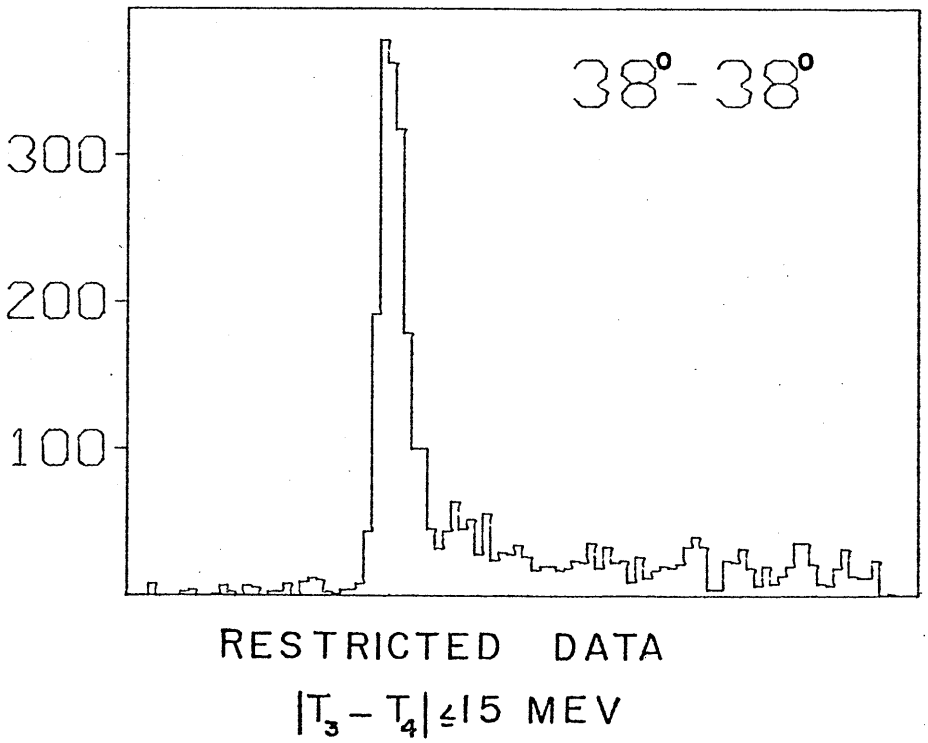

Figure 4.4.5 Effect of Restricting Data in Q-Value Spectra

In the upper graph, all data has been included in the spectrum, but the lower graph shows only data satisfying a kinematic restriction.

Section 4.5 $^3H(p,pn)d$

Table V shows the angles that were covered in the various experimental runs (see Figure 4.5.1) and the minimum values of the deuteron momentum p5 that were kinematically possible. The angle pair 29.5°-50° was studied on two separate runs. Figure 4.5.2 shows the $^3H(p,pn)d$ experimental data and the attenuation model predictions (normalized to the data) for several angles using doublet n-d total cross sections. The shapes of the predictions are obviously incorrect for regions to the right of the peak. This feature is repeated for all other angle pairs studied. As proton energy increases, above 5 MeV, the p-d relative energy rises and the n-d relative energy decreases. Also, the p-d total cross section monotonically decreases for increasing relative energy but the doublet cross section peaks near 20 MeV. Thus the p-d transmission coefficient drops monotonically for increasing proton energy, but the n-d coefficient peaks at some value. Therefore, the product of the two transmission coefficients has only a relative maximum at the experimental peak cross section and then starts to increase again for higher energy protons. For symmetric angles, then, the approximately Gaussian prediction of the SIA is made highly asymmetric by the two transmission coefficients. A conclusion one may draw from this disagreement with experiment is that the n-d system is no longer in a definite spin state once QFS has occurred; the n-p interaction completely destroys any previous spin alignment between the n and the d. This effect is not unexpected since the depolarization has been observed in ^2H

Table V

History of Runs

Run Number	Incident Energy MeV	Angles Covered θ p-θ n	p5 min ^{3}H(p,pn)d MeV/c	p5 min ^{3}H(p,pn)d* MeV/c	p5 min ^{3}H(p,dn)p MeV/c
1	45.4	29.5-50	1.0	9.7	57.4
		35-35	19.8	10.9	54.3
		35-45	.7	9.3	47.5
		40-40	.3	8.9	38.7
		45-35	.6	9.3	29.7
		50-29.5	.9	9.6	21.1
2	45.3	29-46	8.0	.8	62.9
		38-38	8.1	.7	45.5
		43-32.75	7.9	.88	35.9
		48-26.8	7.3	1.5	26.2
3	46.5	29.5-50	.5	9.	58.6
		30-30	37.7	28.7	65.6
		33-33	27.8	18.9	60.2
		33-42.8	8.5	.1	56.3
		50-50	49.9	57.8	8.8
		56-56	85.9	93.2	49.8

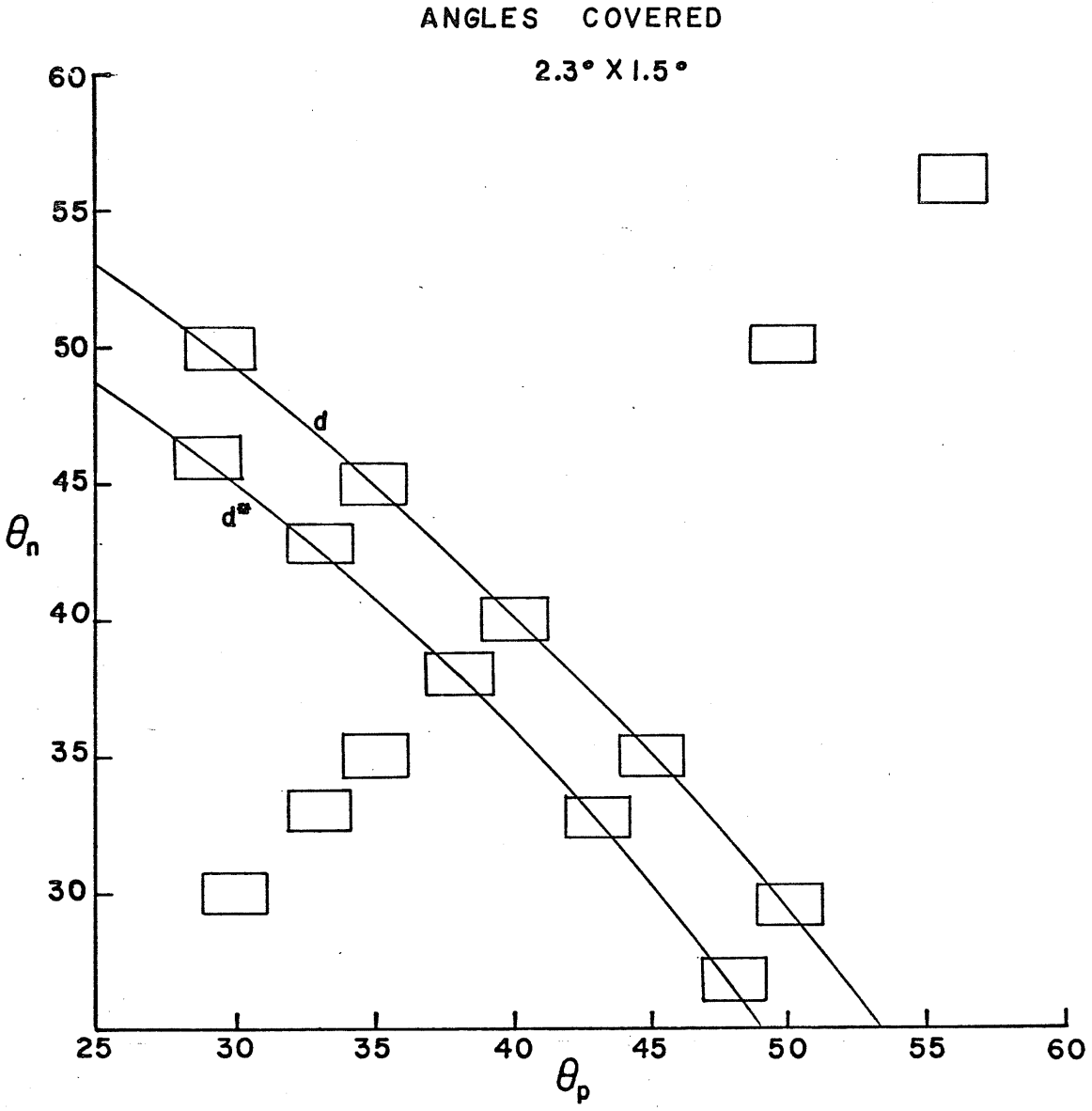

Figure 4.5.1 Angles Studied

Angle pairs consistent with $^3H(p,pn)d$ and $^3H(p,pn)d^*$ quasi-free kinematics are described by two loci, as shown.

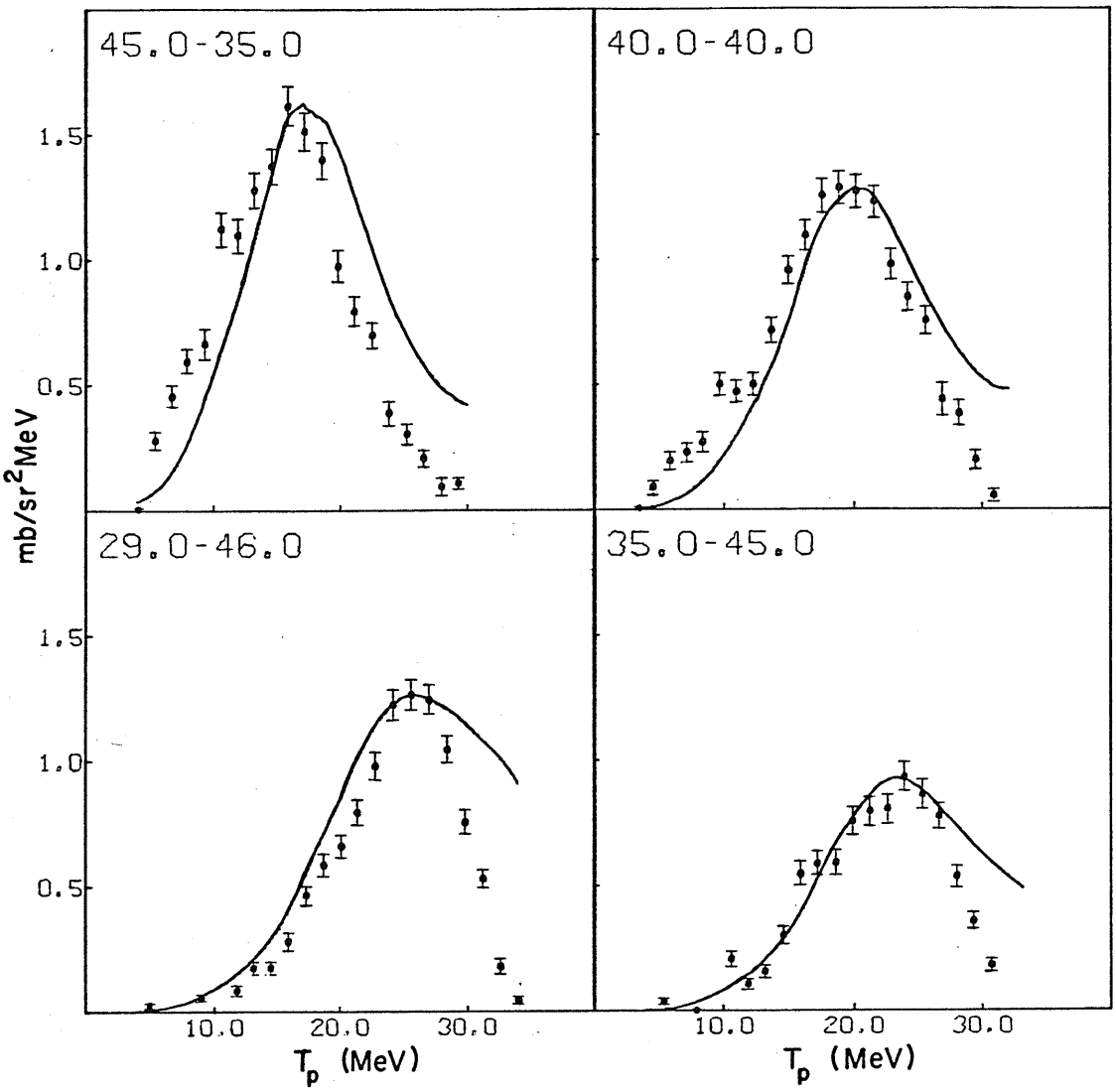

Figure 4.5.2 $^{3}H(p,pn)d$ Data and Attenuation Model Predictions Using Doublet n-d Total Cross Sections

The curves have been normalized to the data.

breakup and may be predicted using the Wolfenstein parameters (R76). It is unfortunate that this effect exists because the wavefunctions used to compute the transmission coefficients assume that this structure is still valid (that is, Eckart functions are used which represent ^{3}H and ^{3}He structure). One hopes that the error induced by the use of these functions is not large, and in any case there is little alternative within the attenuation model formalism except to use nucleon-deuteron scattering states. There is no evidence that these functions would perform more reliably, and in fact normalization problems would be more severe since scattering states are not square integrable. Henceforth, only standard N-d total cross sections, as shown in Figure 4.3.1, will be used with the attenuation model. It will be demonstrated that the attenuation model does account for many features of the data, and so the theory appears to be relatively insensitive to nature of the wavefunctions used in computing the transmission coefficients.

As mentioned in Section 1.3, Lim has suggested (L73) that the transmission coefficient calculation overestimates the effect of attenuation. This is partly because p-d and n-d scattering cannot both ruin a QFS event (it takes only one scattering with the spectator to spoil the event), and also because n-d or p-d small angle scattering may result in only negligible deviation from QFS distributions. It may also account for the fact that a real deuteron does not actually exist inside the trion. For these reasons, it is necessary

somehow to decrease the n-d and p-d total cross sections used in the calculation. The easiest method of accomplishing this objective is simply to multiply the experimental cross sections for these processes by a factor D. Lim discovered (L73) that D=.8 produced good results for ^{2}H and ^{3}H breakup. Figure 4.5.3 compares our experimental results for 40°-40° (which we shall consider a typical angle pair because it is approximately midway between the extremes studied in our experiment) with the predictions of the attenuation model for different values of D. It appears that the major effect of this parameter is to alter the attenuation; the shapes of the peaks are left approximately unchanged for small variations in D.

Figure 4.5.4 shows more $^{3}H(p,pn)d$ data with the attenuaton model calculation (using D=.7) and the predictions of the SIA. Both calculations have been normalized to the data for this figure, and Table VI displays the normalization factors that were necessary for the theories to fit the data (i.e. these numbers multiply the theory). It would be interesting to see if the same value of D would allow a good fit to the data at other projectile energies, since the attenuation model provides an energy dependence in the total cross sections that are used. It is clear that the attenuation model shifts the position of the peak in the calculated distribution away from the data for asymmetric angle pairs. The SIA appears to peak in the correct place for most spectra, but the widths and heights of the data more closely resemble the attenuation model than the SIA. Eckart functions with N=2.03 and b=1.90 fm^{-1} were used for both

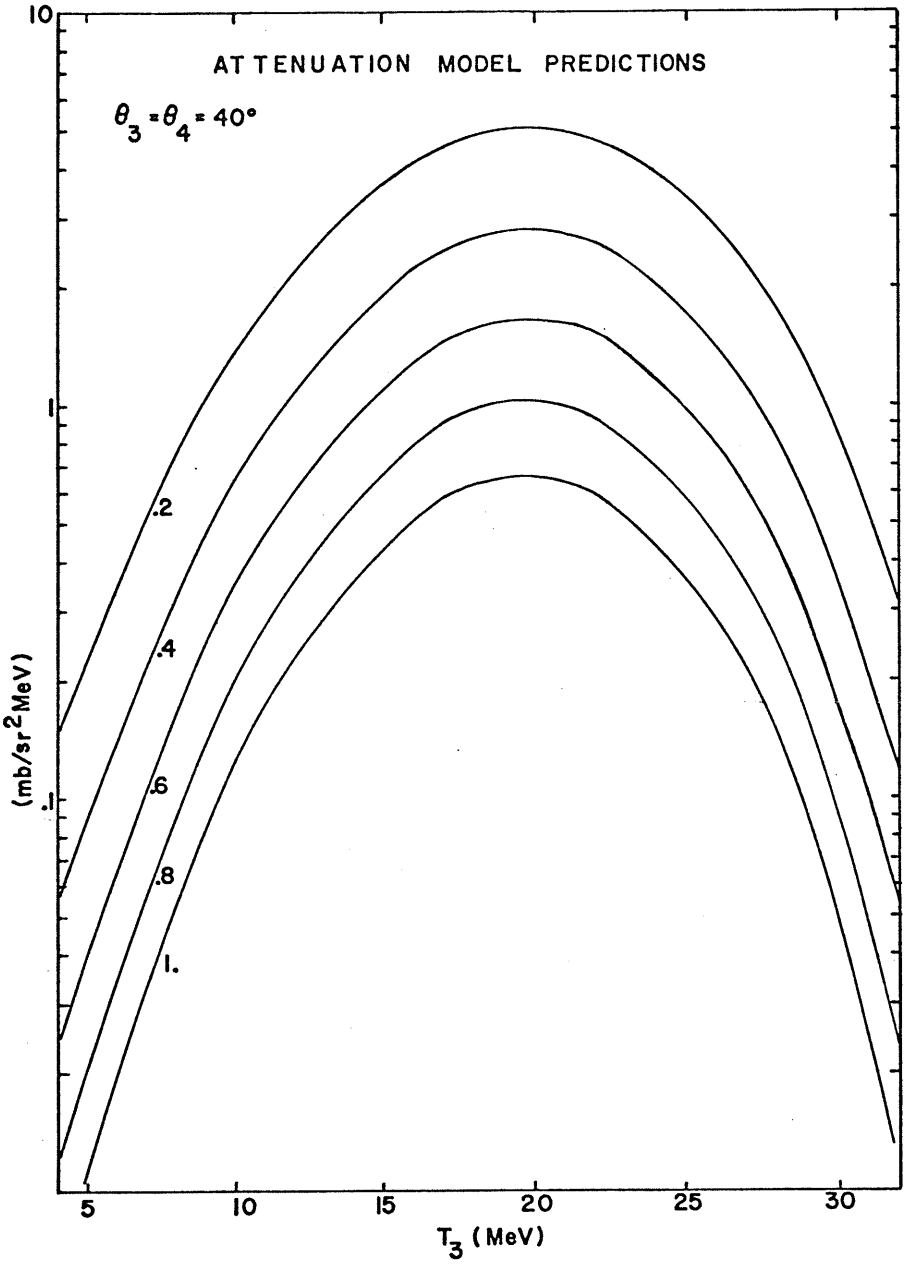

Figure 4.5.3 Effect of Changing the Parameter D on the Attenuation Model Prediction for the Reaction $^3H(p,pn)d$ at 40^o-40^o.

The results are shown for values of D ranging from .2 to 1.0.

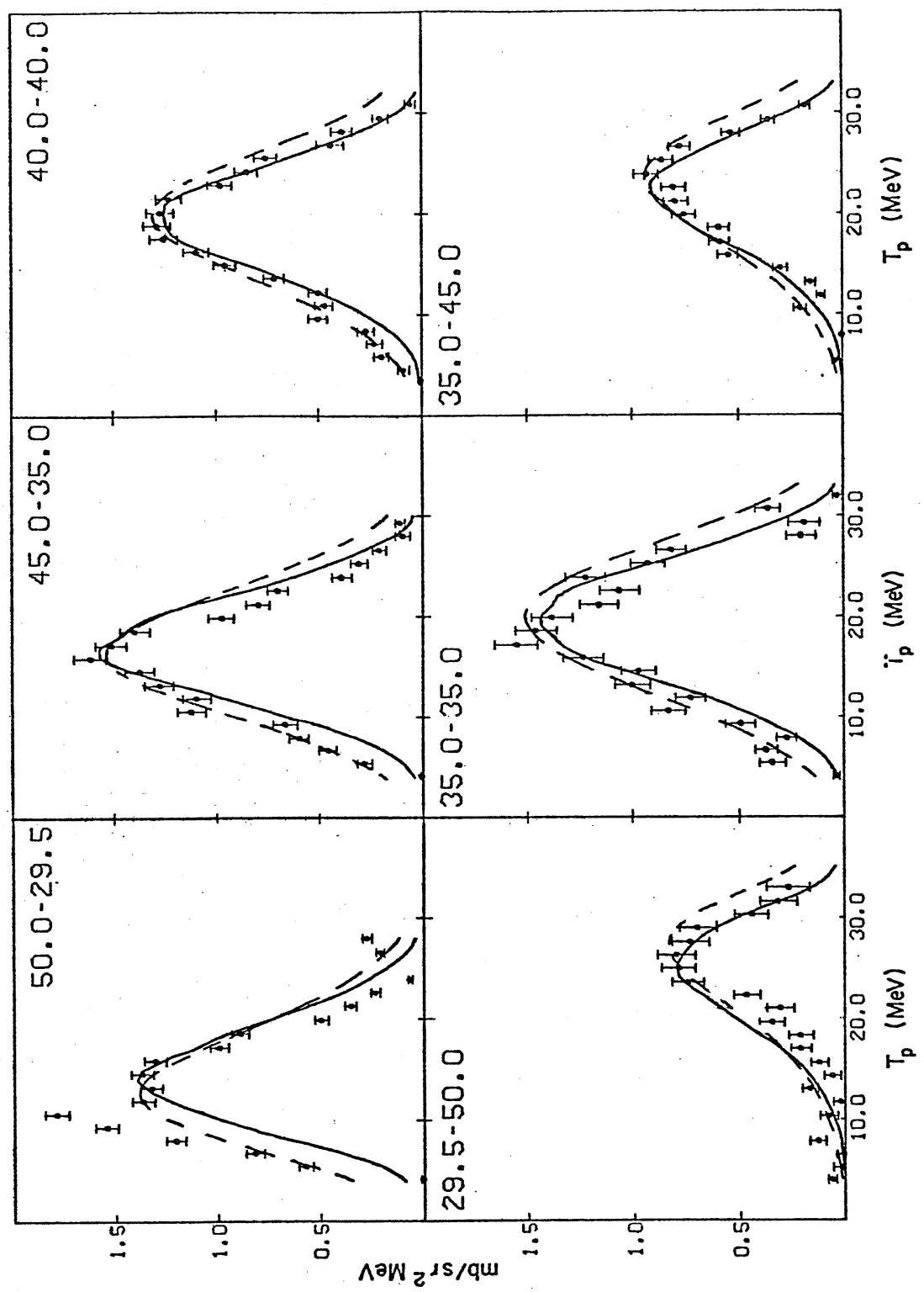

Figure 4.5.4 Part (a) ^{3}H(p,pn)d Data and Theoretical Curves Using the SIA (dashed) and Attenuation Model (solid).

These data were taken during the first run.

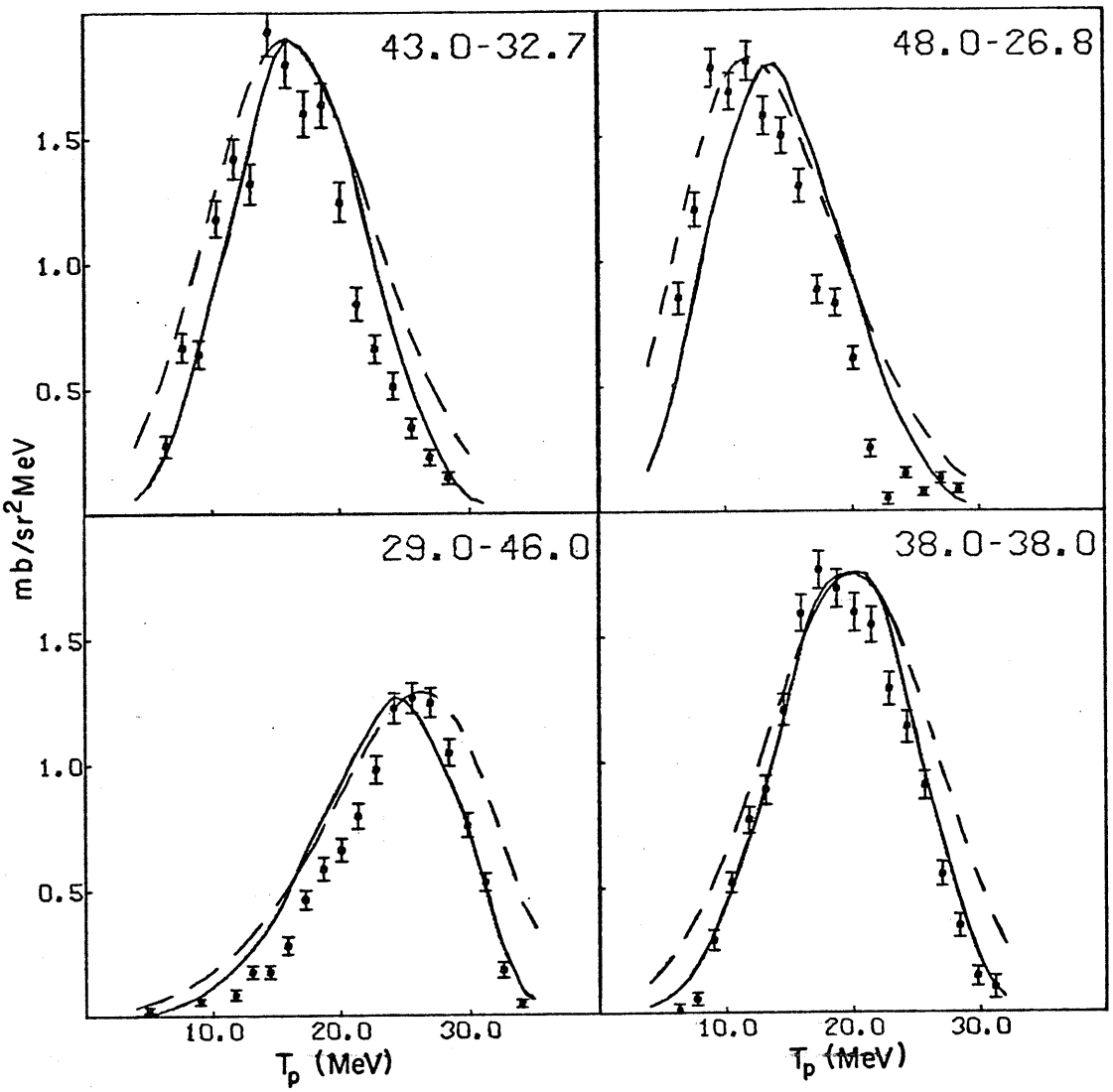

Figure 4.5.4 Part (b) $^{3}H(p,pn)d$ Data and Theoretical Curves using the SIA (dashed) and Attenuation Model (solid). These data were taken during the second run.

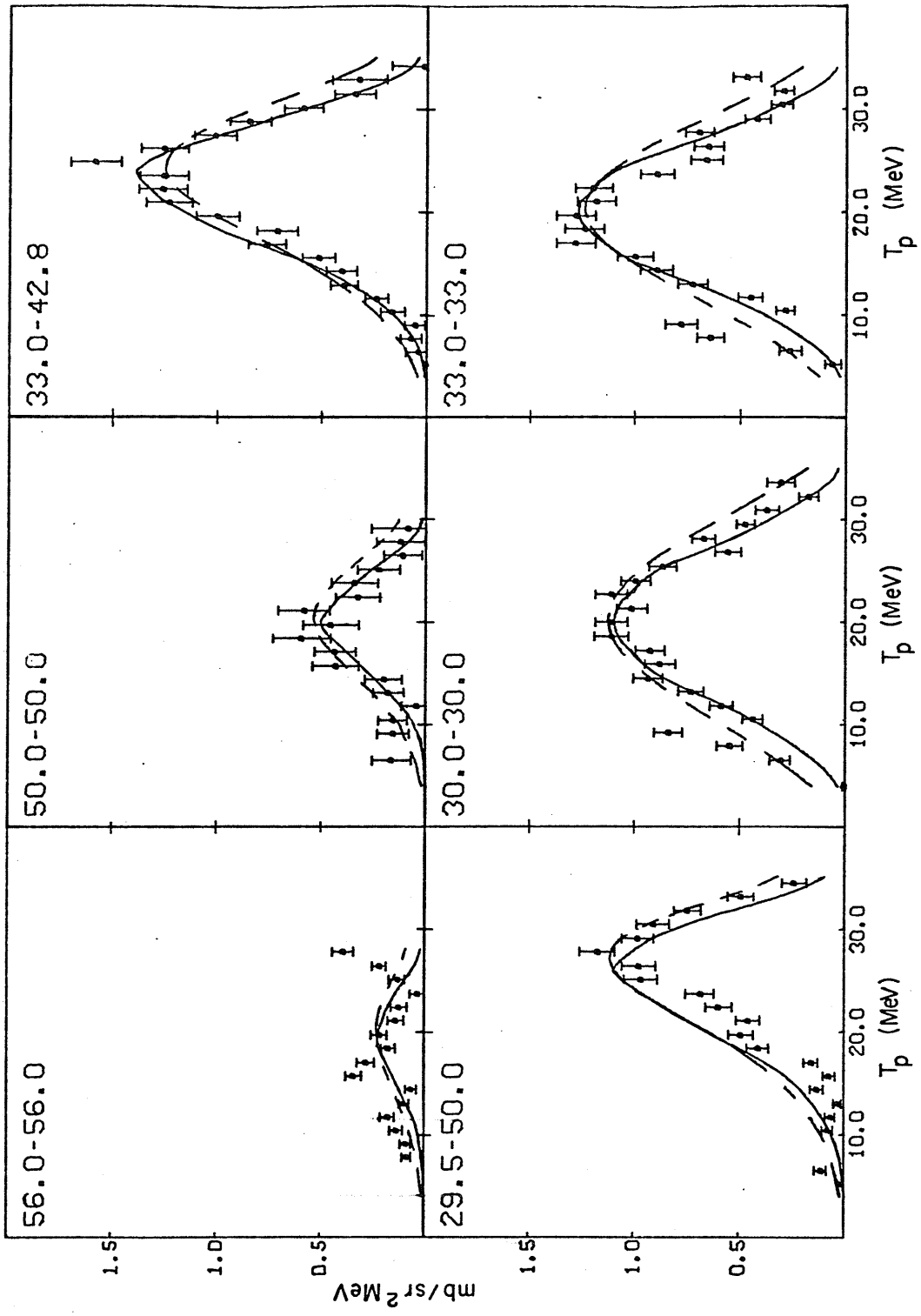

Figure 4.5.4 Part (c) ^{3}H(p,pn)d Data and Theoretical Curves Using the SIA (dashed) and Attenuation Model (solid). These data were taken during the third run.

Table VI

$^{3}H(p,pn)d$

Angle Pair	Peak Height (mb/sr²MeV)	SIA Normal-ization	Att'n Normal-ization
29 -46	1.27	.17	1.00
29.5-50	.80	.12	.75
29.5-50	1.00	.17	1.00
30 -30	1.09	.13	.61
33 -33	1.27	.16	1.00
33 -42.8	1.35	.17	1.00
35 -35	1.50	.18	.90
35 -45	.90	.13	.75
38 -38	1.72	.22	1.26
40 -40	1.29	.18	1.00
43 -32.75	1.85	.23	1.34
45 -35	1.56	.21	1.25
48 -26.8	1.75	.24	1.40
50 -29.5	1.78	.20	1.20
50 -50	.56	.20	1.20
56 -56	.22	.25	2.00

the SIA term and the n-d attenuation calculation, while N=1.78 and b=1.90 fm^{-1} was used for p-d scattering. A spin factor of S=3/2 (see Section 1.1) was used in the SIA calculation and the half-off-the-energy-shell t-matrix was used to describe the n-p interaction. Figure 4.5.5 shows the n-d momentum distribution that was used in the calculation. This function has an exponential behavior (linear on a semi-logarithmic plot) beyond 60 MeV/c. Some of the data exhibit peaks around 11 MeV which are the result of technical problems with the charged particle detector (in particular, poor particle identification at the energy at which protons start to enter the E detector). We have also found that D=.7 fits data from the ^{3}He(p,2p)d reaction (T74) using the ^{3}He Eckart wavefunction to describe the ^{3}He nucleus.

Figure 4.5.6 shows the variation in peak cross section for ^{3}H(p,pn)d "quasi-free angles". At these angles, small spectator momentum is possible for some value of the outgoing proton's energy. At this position in the spectrum, the momentum distribution and SIA cross section peak. Thus $|\phi(q)|^2$ is the same at the maximum for all of these angles and the only difference in the coincidence cross sections that the SIA predicts is due to variations in $\frac{d\sigma}{d\Omega_{34}}$ and KF, but these are generally minor. Therefore, the SIA predicts an approximately flat angular distribution. However, the data are certainly not flat, as are ^{3}H(p,pd)n and ^{3}He(p,2p)d (T74), but exhibit a strong angular dependence. This variation in the cross section suggests that the ^{3}H(p,pn)d cross section depends on the n-d relative

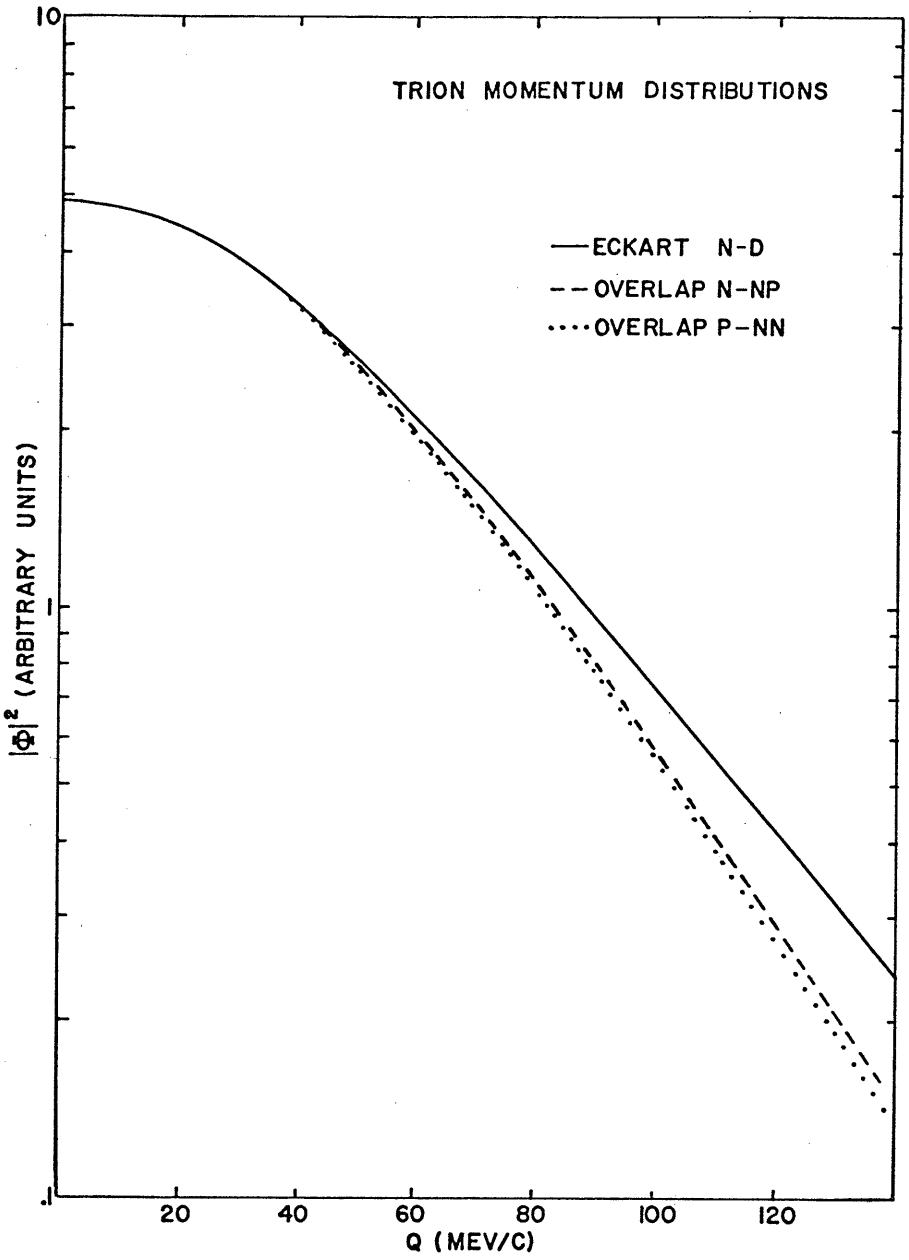

Figure 4.5.5 The n-d Momentum Distribution

Curves are shown for the n-d momentum distribution using an Eckart function, overlaps of an asymptotic n-p or n-n function with an Irving-Gunn function.

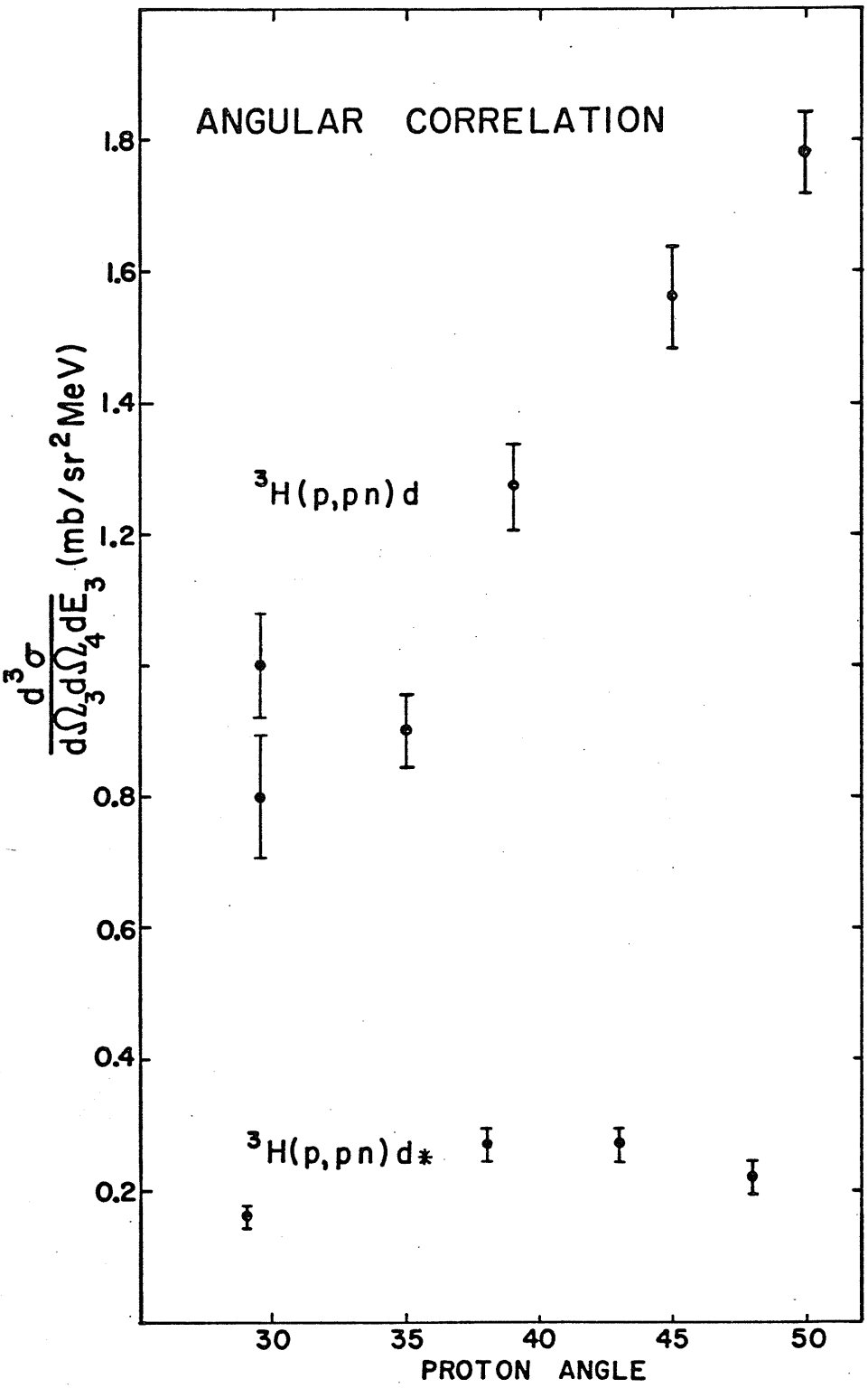

Figure 4.5.6 Variation of ^{3}H(p,pn)d and ^{3}H(p,pn)d* Cross Sections with Proton Angle
Only angle pairs with quasi-free kinematics are shown.

momentum vector before the collision, and not just its magnitude as the SIA predicts. It was hoped that the attenuation model calculations would simulate this angular dependence because of the different values of the n-d (doublet) and p-d total cross sections near the SIA peak at different angle pairs. Use of the doublet total cross sections produced only minor anisotropy in the angular correlation but had an adverse effect on the peak shape. Doublet cross sections were then abandoned and identical total cross sections were used for the n-d and p-d interactions. Hence, no angular variation is possible, and the effect of the attenuation coefficients has been to narrow the peak, decrease its height, and shift its position by a few MeV.

Near the peak in the coincidence cross sections, the n-p scattering angle is near 90° only for symmetric angle pairs. It is for asymmetric angle pairs, then, that the effects of P, D, etc. partial waves in the n-p scattering cross section are most strongly felt. The anisotropic t-matrix used for the calculation performs fairly well at duplicating these effects. The overall good agreement of the data with the theoretical curves supports the view that the wavefunction is primarily S state and the reaction mechanism is dominated by quasi-free scattering.

One notices that some of the experimental cross sections seem to rise for proton energies to the right of the peak. This may partially be the result of reaction mechanisms competing with QFS (like FSI), but is more likely due to the

important effect of vanishingly small detection efficiencies for very low neutron energies. Any background counts that have not been subtracted away effectively contribute an enormous cross section in the region above proton energies of 33 MeV. Figure 4.5.7 shows the effect of dummy subtraction on the cross section for two angles with good statistics. There is essentially no change for $^{3}H(p,pn)d$, but the $^{3}H(p,pn)d^{*}$ cross sections are made somewhat more ragged. For the angle pair 29.5°-50° studied in the first run and 33°-42.8° and 50°-50° studied in the third run, no dummy subtraction was performed, but as has been demonstrated, this does not affect the validity of the data.

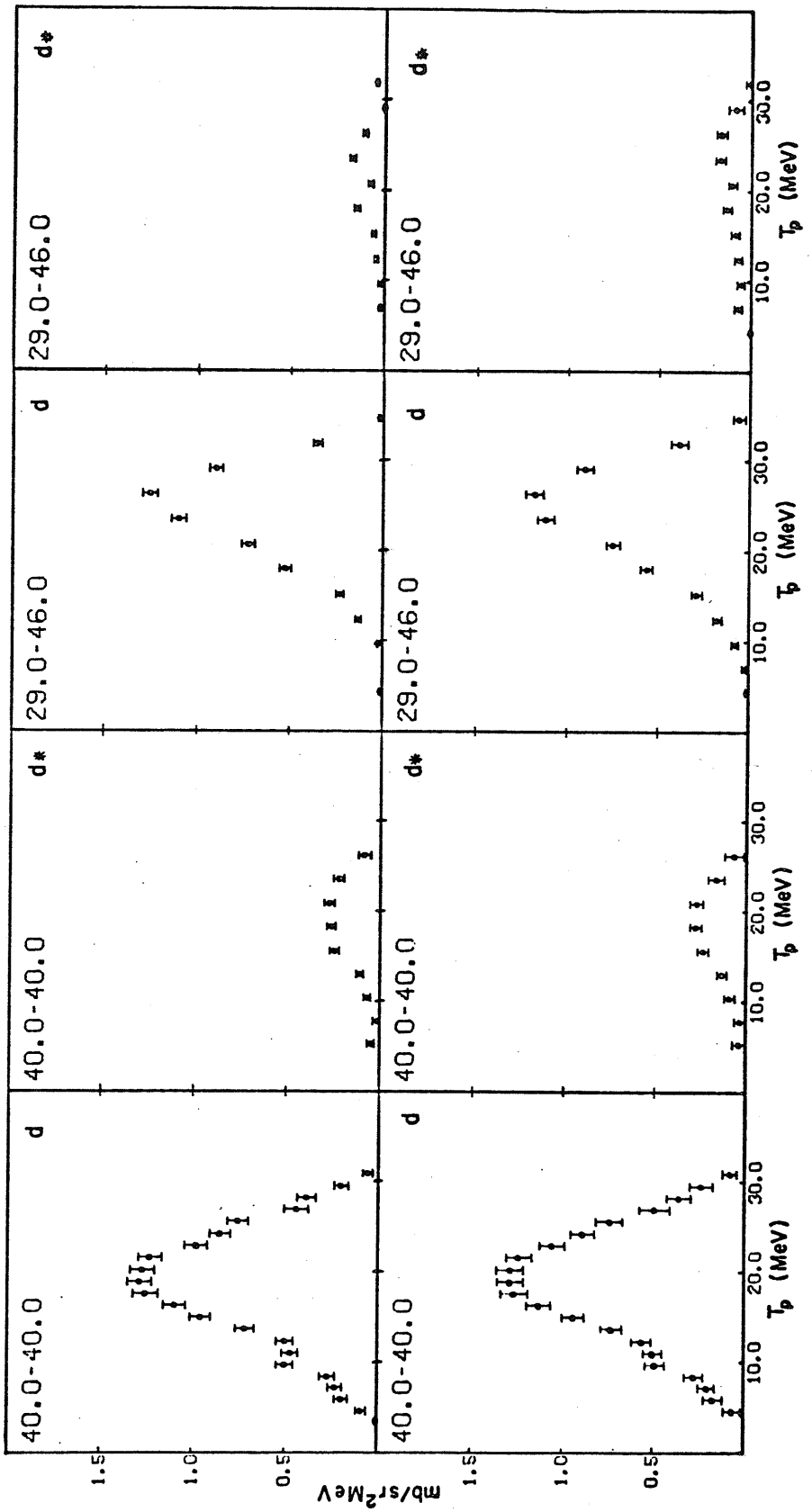

Figure 4.5.7 Effect of Dummy Subtraction on $^3H(p,pn)$ Data for d and d* Final States

The upper set of data is dummy-subtracted but the lower set is not.

Section 4.6 $^3H(p,pn)d^*$

Figure 4.6.1 shows $^3H(p,pn)d^*$ data for various angles. The attenuation model and SIA were used to generate the theoretical results. For most angle pairs, the attenuation model once again demonstrates its superiority in predicting the width of the peak, although the effect is not as pronounced as for the $^3H(p,pn)d$ data (probably because the statistics are poorer). Table VII displays the peak heights and normalization factors. The off-shell t-matrix was used to generate n-p cross sections while an overlap of an Irving-Gunn trion wavefunction (α =.89) and an asymptotic d* wavefunction (H57)

$$\Phi(\vec{\rho}) = \frac{a_{np}}{\rho}\left(1 - \frac{\rho}{a_{np}} - e^{-\beta\rho}\right) \qquad \beta = 1.14\ fm^{-1},\quad a_{np} = -23.7\ fm$$

was used for the momentum distribution (see Figure 4.5.5). The shape of this distribution is quite insensitive (T74) to the n-p scattering length. The derivation of the above equation is based upon its being a low energy limit of an asymptotic spatial equation. Since the trion is only a few fermis in diameter and its most important region (if no cutoff is used) occurs at the origin (where all three particles are at the same location), some doubt may be cast upon its validity. However, it has been demonstrated (T74) that it provides acceptable results when used in its current context, although this may be due to the fact that the overlap resembles the n-d wavefunction (Figure 4.5.5). A spin factor of S=1/2 has been used in the SIA calculation. The cross sections used in the transmission coefficient calculation were the N-d total cross sections

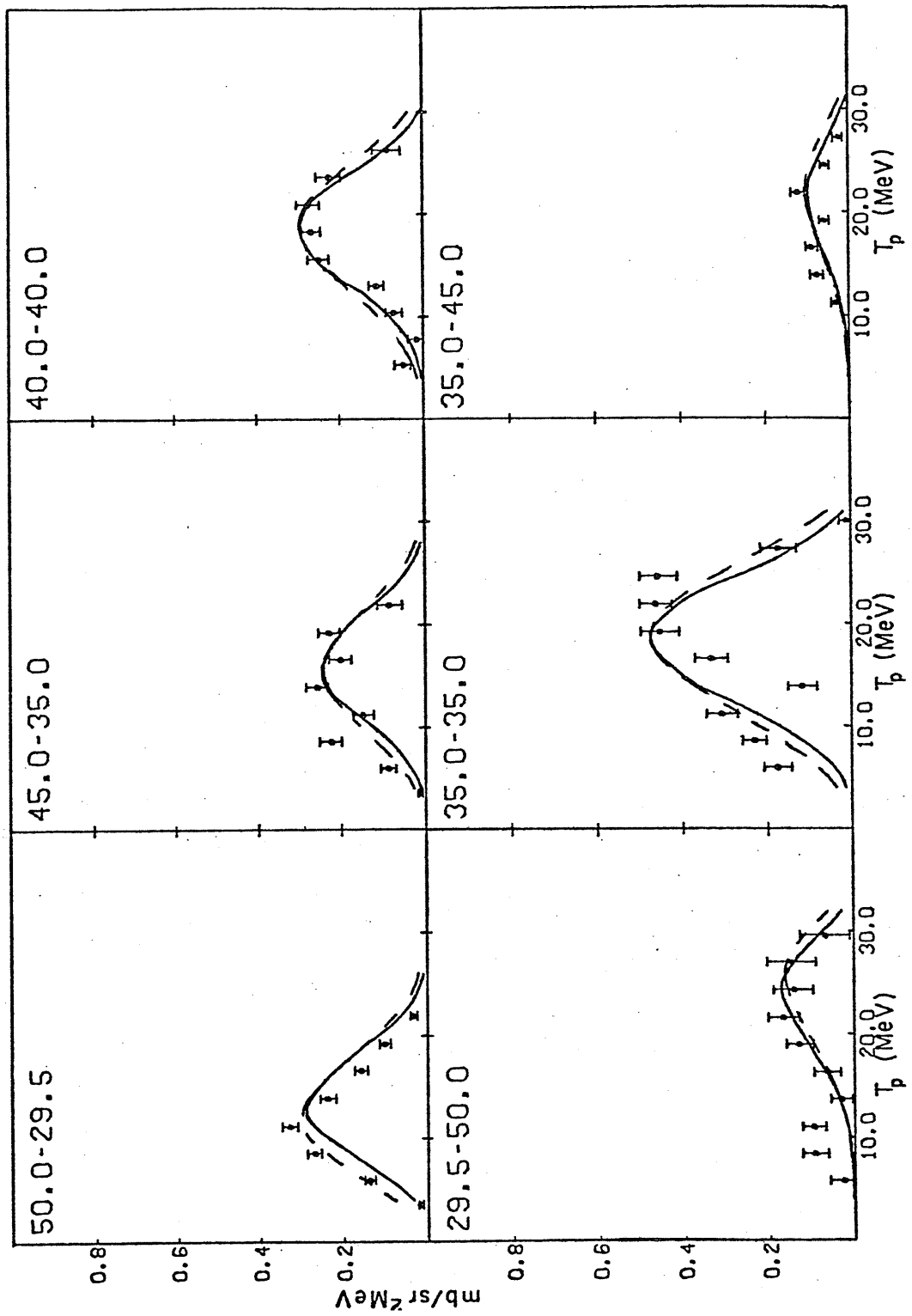

Figure 4.6.1 Part (a) $^3H(p,pn)d^*$ Data and Theoretical Curves Using the SIA (dashed) and Attenuation Model (solid). These data were taken during the first run. Theory is normalized to data.

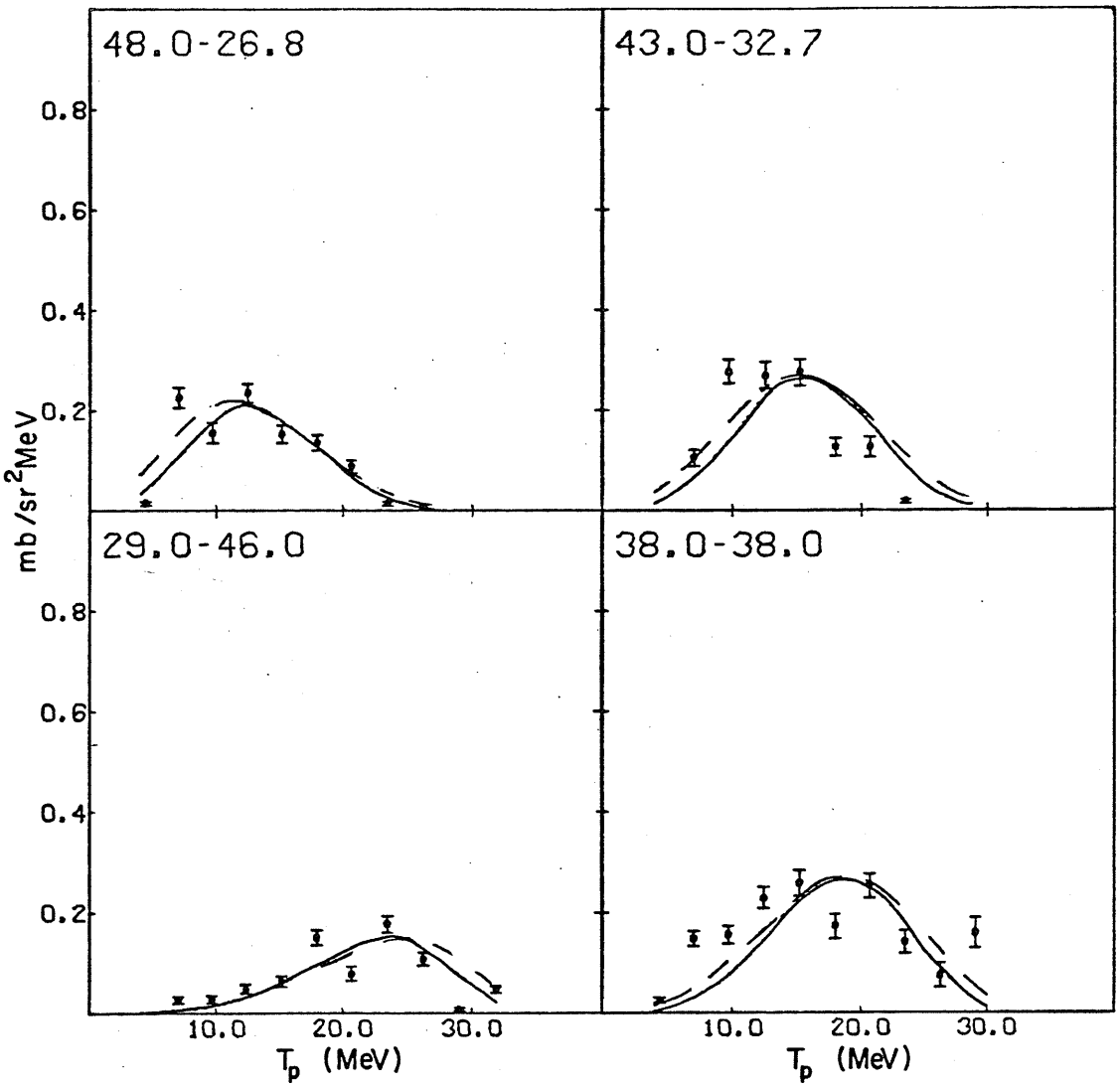

Figure 4.6.1 Part (b) $^{3}H(p,pn)d^{*}$ Data and Theoretical Curves Using the SIA (dashed) and Attenuation Model (solid).

These data were taken during the second run. Theory is normalized to data.

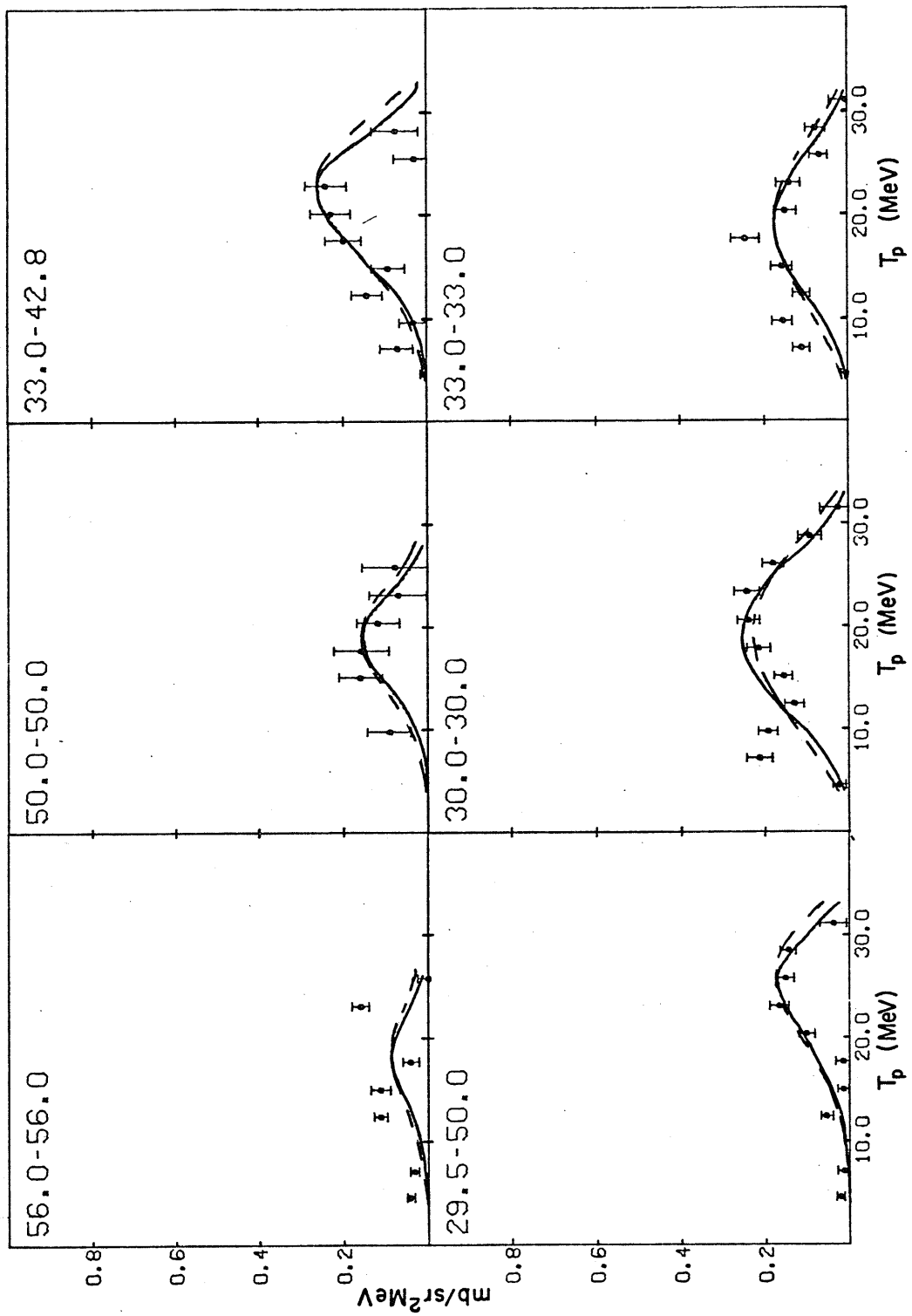

Figure 4.6.1 Part (c) ^{3}H(p,pn)d* Data and Theoretical Curves Using the SIA (dashed) and Attenuation Model (solid). These data were taken during the third run. Theory is normalized to data.

Table VII

$^{3}H(p,pn)d^{*}$

Angle Pair	Peak Height (mb/sr²MeV)	SIA Normalization X 10^{-5}	Att'n Normalization X 10^{-5}
29 -46	.16	.12	.66
29.5-50	.18	.15	.90
29.5-50	.17	.17	.90
30 -30	.24	.15	.72
33 -33	.20	.12	.54
33 -42.8	.23	.21	1.05
35 -35	.47	.33	1.59
35 -45	.15	.09	.45
38 -38	.25	.21	1.05
40 -40	.27	.26	1.35
43 -32.75	.28	.21	1.05
45 -35	.25	.21	1.14
48 -26.8	.22	.18	.90
50 -29.5	.31	.27	1.41
50 -50	.15	.45	2.70
56 -56	.09	.90	6.00

multiplied by D=.7, as described in Section 4.5. In principle, N-d* total cross sections should have been used, but these would be difficult to generate. The only important feature of the attenuation calculation for ^{3}H(p,pn)d* is its effect on the shape of the peak, since the theoretical magnitude is undefined (because the scattering function used in the overlap is not square integrable and so has arbitrary normalization). It is reasonable to assume that that the N-d and N-d* total cross sections should differ in magnitude but not in energy dependence (B70). Figure 4.5.3 showed that if only the magnitude of the cross section changes, the major effect is an alteration of the magnitude of the theoretical cross section. Therefore, the attenuation calculation should be insensitive to the substitution of the N-d for the N-d* total cross sections.

Figure 4.5.6 shows the angular variation of the peak cross section for ^{3}H(p,pn)d* for the quasi-free angles considered. This variation is almost flat in contrast to the ^{3}H(p,pn)d data (Figure 4.5.4). If there were any doubts that the ^{3}H(p,pn)d* cross sections were only the tails of the ^{3}H(p,pn)d distributions, this graph should put them to rest. No dummy subtraction was performed for the angles 29.5°-50° (first run), and 33°-42.8° and 50°-50°.

Section 4.7 ^{3}H(p,dn)p

Figure 4.7.1 shows ^{3}H(p,dn)p data for various angles. Most of the spectra that contain a peak have approximately the same characteristic: the data peak where the energy of the outgoing proton is lowest. This suggests that the proton plays the role of a spectator in a quasi-free reaction (not a QFS). Referring to Figure 4.7.2, the ^{3}H decomposes into a proton and di-neutron with the latter being struck by the projectile proton. The quasi-free reaction nn(p,n)d occurs at the upper vertex. Unfortunately this process cannot be observed directly but we will approximate the vertex form factor with a constant.

A simplified SIA theory has been used to generate the curves in Figure 4.7.1. An overlap of an Irving-Gunn trion wavefunction with α =.89 and an asymptotic n-n wavefunction

(H57) $$\Phi(\vec{\rho}) = \frac{a_{nn}}{\rho}\left(1 - \frac{\rho}{a_{nn}} - e^{-\beta\rho}\right) \qquad \beta = 1.19\ fm^{-1},\quad a_{nn} = -16.4\ fm$$

was used to generate the momentum distribution (see Figure 4.5.5) required by the SIA. The most interesting feature of the data is the appearance of peaks. The shape of these peaks in the impulse approximation is determined almost wholly by the momentum distribution squared. In order to see if the SIA can predict the shape and position of these peaks, then, it is sufficient to compare the momentum distribution and the KF with the data (i.e. theory $|\phi(q)|^2$*KF, no two-body cross section is used). This comparison is made in Figure 4.7.1. There is good agreement in many cases demonstrating the dominance of the quasi-free process. Agreement might be even better if an

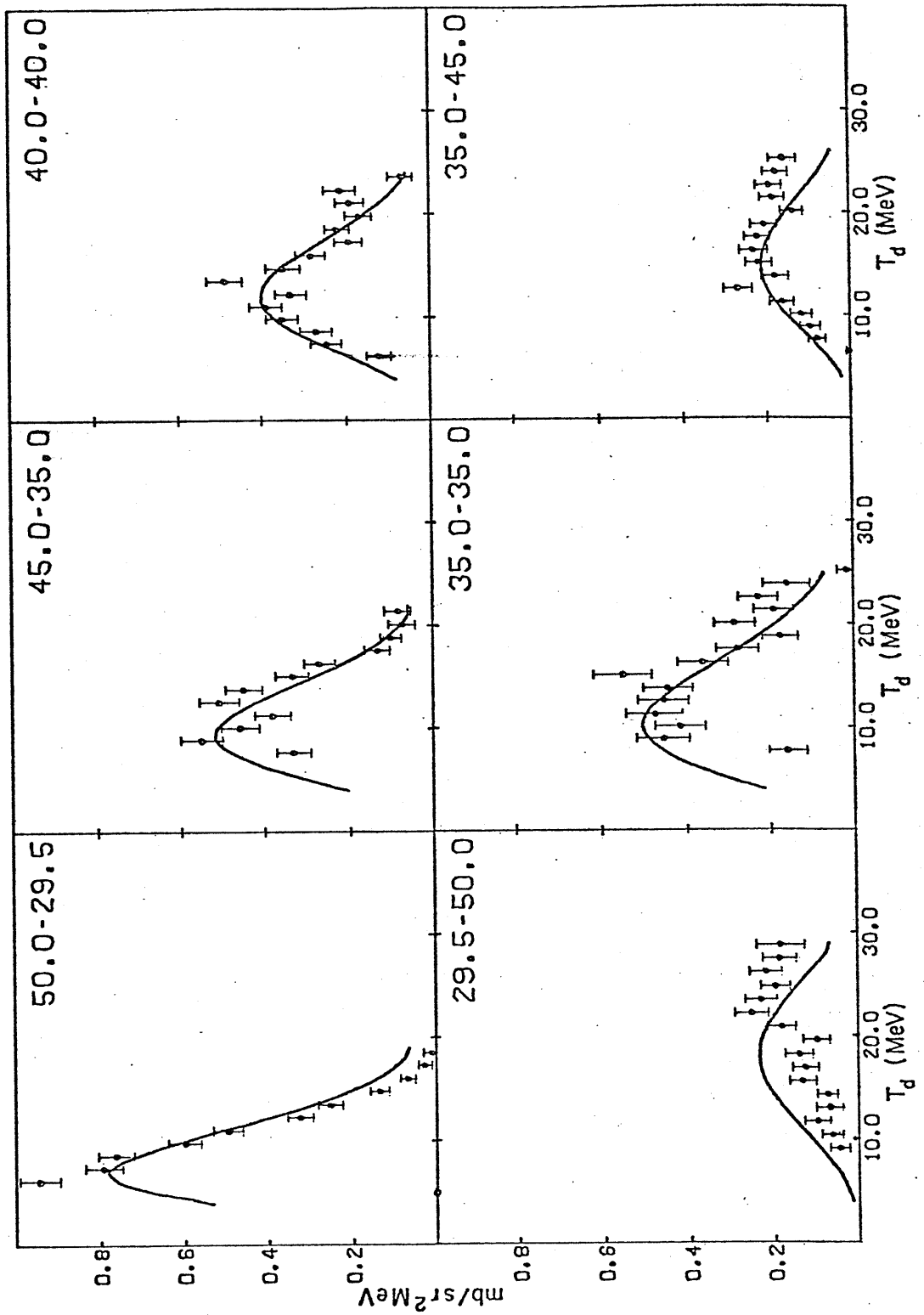

Figure 4.7.1 Part (a) $^3H(p,dn)p$ Data and SIA Predictions

Constant two body cross sections have been assumed for the SIA. These data were taken during the first run. The theory is normalized to the data.

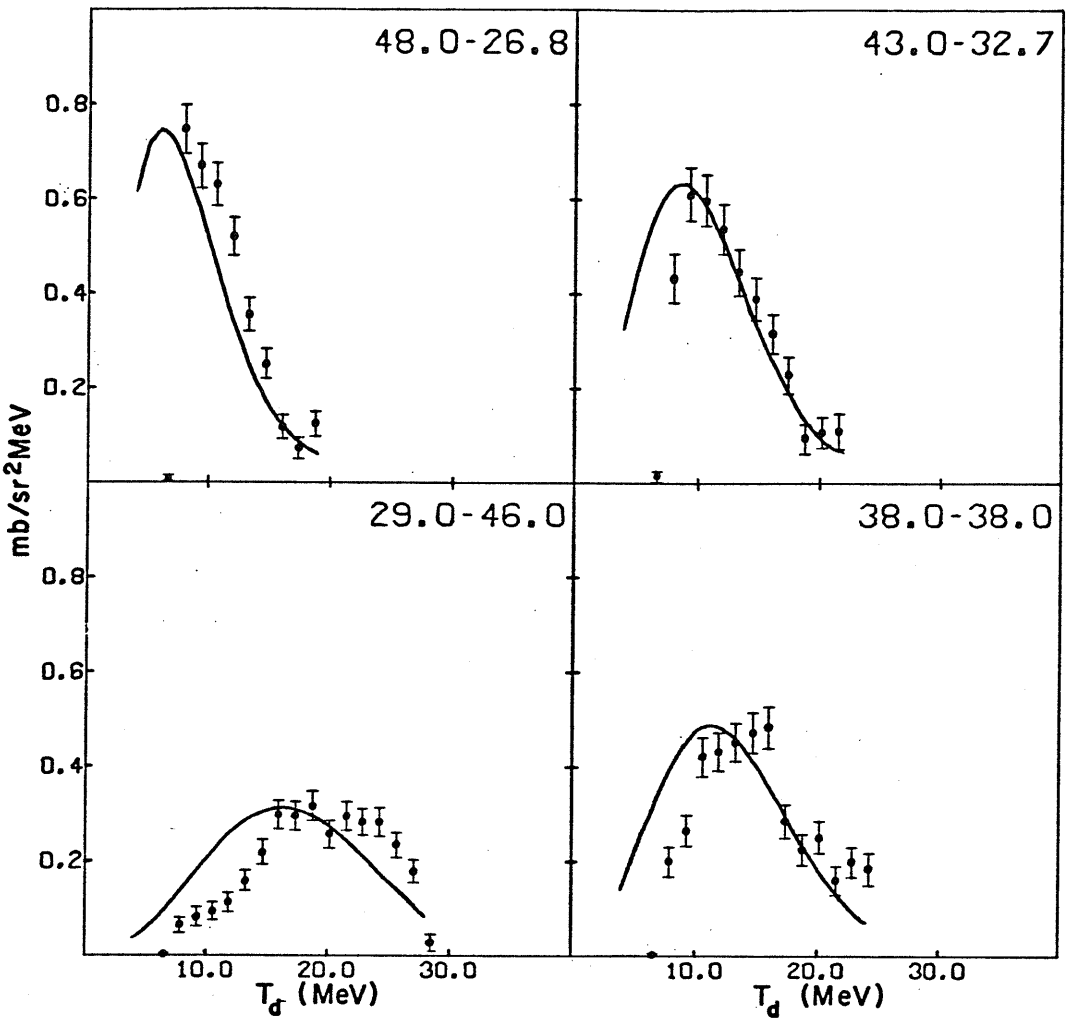

Figure 4.7.1 Part (b) $^{3}H(p,dn)p$ Data and SIA Predictions

Constant two body cross sections have been used for the SIA. The data were accumulated during the second run.

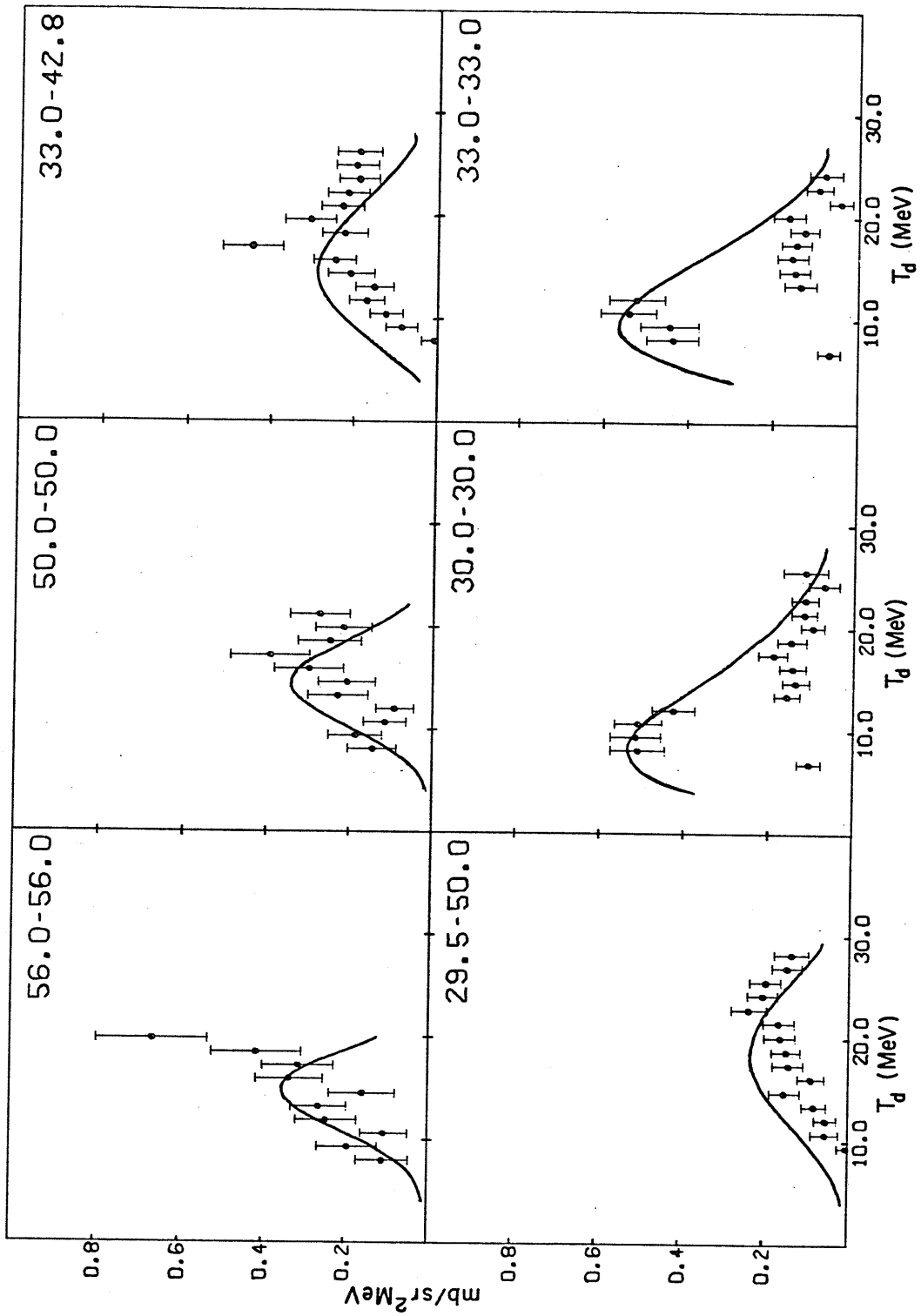

Figure 4.7.1 Part (c) $^{3}H(p,dn)p$ Data and SIA Prediction

Constant two body cross sections have been assumed for the SIA. The data were accumulated on the third run.

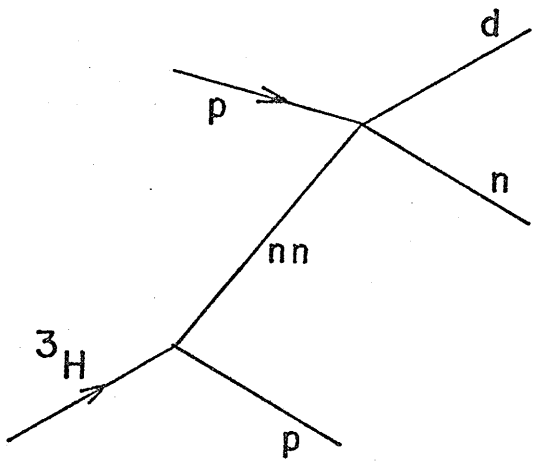

Figure 4.7.2 Feynman Diagram Showing a Quasi-Free Reaction for the Process ^{3}H(p,dn)p

appropriate two-body cross section could be generated. If deuteron energies are high, the behavior of the upper vertex might resemble neutron pickup. A comparison with the similar $^{2}H(p,d)p$ reaction reveals that the angular distribution should show strong peaking (Bo71). Alternatively, where the neutron emerges at forward angles, the cross section should behave similarly to that of a charge exchange reaction like $^{2}H(p,n)pp$ which has a relatively flat angular dependence (Ma68). One might expect an energy dependence like that of elastic n-d scattering. One might take an alternate stance and deduce the two-body cross section assuming the validity of the SIA. However, one would not expect reliable results because of the diffuseness of the di-neutron, the large off-the-energy-shell effect, and the weak sensitivity to the two-body cross section. The most notable failure of the simplified SIA occurs for 56°-56°, but near this angle pair quasi-two-body processes such as $p+t \rightarrow d+d^{*}$ are possible with deuteron energies near 20 MeV. The existence of such reactions may explain the anomalous enhancement for this angle pair. Table VIII shows the normalization factors and peak heights for the $^{3}H(p,dn)p$ data.

Table VIII

$^{3}H(p,dn)p$

Angle Pair	Peak Height (mb/sr²MeV)	SIA Normal-ization X 10^{-5}
29 -46	.29	.40
29.5-50	.23	.25
29.5-50	.23	.25
30 -30	.51	.90
33 -33	.54	.75
33 -42.8	.28	.30
35 -35	.47	.55
35 -45	.21	.17
38 -38	.48	.40
40 -40	.41	.27
43 -32.75	.60	.45
45 -35	.51	.31
48 -26.8	.73	.50
50 -29.5	.93	.45
50 -50	.39	.12
56 -56	.66	.20

Chapter 5

SUMMARY AND CONCLUSIONS

The experimental cross sections for $^3H(p,pn)d$, $^3H(p,pn)d^*$, and $^3H(p,dn)p$ have been compared with the predictions of the SIA and attenuation model. The latter adequately describes the $^3H(p,pn)d$ reaction for symmetric angles if the total cross sections used to evaluate the transmission coefficients are reduced in magnitude by 30%. For asymmetric angles, the attenuation model shifts the peaks to higher or lower proton energies, but the SIA predicts the correct position for the peak. When total cross sections for n-d in a doublet state are used, there is poor agreement with the experimental shape of the peak. This suggests that the n-d system is no longer in a doublet spin state after the reaction has occurred. Because the peaks predicted with the SIA are generally at the correct proton energy but are more than a factor of 5 too large, multiple scattering (i.e. multi-step) effects must indeed be significant for a projectile of 45 MeV. Because the diagrams for the competing processes add coherently with QFS, the factorizability inherent in the SIA is destroyed and the cross section for a given geometry is no longer largely dependent on only the relative momentum of the n-d system.

The $^3H(p,pn)d^*$ data are smaller by a factor of 5 compared to the $^3H(p,pn)d$ data and have poorer statistical significance. However, the data show that the attenuation model performs more reliably than the SIA in predicting the width of the momentum

distribution.

The $^{3}H(p,dn)p$ data peaks in a kinematic region where the outgoing proton has low laboratory energy. This suggests that the reaction is dominated by a quasi-free process with the proton being a spectator, and an n-n system is struck by the projectile yielding a deuteron and neutron.

REFERENCES

A63 R.D. Amado, Phys. Rev. 132, 485 (1963)
C.A. Lovelace, Phys. Rev. 135, B1255 (1964)
E.O. Alt, P. Grassberger, and W. Sandhas. Nucl. Phys. 82, 167 (1967)

A64 R. Aaron, R.D. Amado, and Y.Y. Yam, Phys. Rev. Lett. 13, 574 (1964)

A66 R. Aaron and R.D. Amado, Phys. Rev. 150, 857 (1966)
R.T. Cahill and I.H. Sloan, Nucl. Phys. A165, 161 (1971)
Mahavir Jain and Gary D. Doolen, Phys. Rev. C 8, 126 (1973)

A74 J. Arvieux, Nucl. Phys. A221, 253 (1974)

A75 R.A. Arndt, tabulation of N-N data, Private Communication, 1975

B56 F.D. Brooks, Progress in Nuclear Physics, 5, 252 (1956)

B57 S.T. Butler and O.H. Hittmair, "Nuclear Stripping Reactions", (Wiley, New York, 1957)

B64 B.L. Berman, L.J. Koester, Jr., and J.H. Smith, Phys. Rev. 133, B117 (1964)

B69 A.I. Baz', Ya.B. Zel'dovich, and A.M. Peredomov, "Scattering, Reactions and Decay in Nonrelativistic Quantum Mechanics", Israel Program for Scientific Translations, Jerusalem (1969)

B70 H. Bruckmann, W. Kluge, H. Matthay, L. Schanzler, and K. Wick, Nucl. Phys. A157, 209 (1970)

B71 K.H. Bray, S.N. Bunker, M. Jain, K.S. Jayaraman, G.A. Moss, W.T.H. van Oers, D.O. Wells, and Y.I. Wu, Phys. Rev. C 3, 1771 (1971)

Bo71 I. Borbely, Phys. Lett. 35B, 388 (1971)

B72 S.N. Bunker, Mahavir Jain, C.A. Miller, J.M. Nelson, P.J. Tivin, and W.T.H. van Oers, Can. J. Phys. 50, 1295 (1972)

B74 Judith Binstock, Phys. Rev. C 10, 19 (1974)

B75 R.A. Brandenburg and P.U. Sauer, Phys. Rev. C 12, 1101 (1975)

C59 G.F. Chew and F.E. Low, Phys. Rev. 113, 1640 (1959)

C65 H. Collard, R. Hofstadter, E.B. Hughes, A. Johansson, M.R. Jearian, R.B. Day, and R.T. Wagner, Phys. Rev. 138, B57 (1965)

C67 B.L. Cohen and C.L. Fink, Nucl. Instr. and Meth. 57, 93 (1967)

C69 B.L. Cohen, E.C. May, T.M. O'Keefe, and C.L. Fink, Phys. Rev. 179, 962 (1969)

C71 R. Corfu, J.-P. Egger, C. Lunke, C. Nussbaum, J. Rossel, E. Scharwz, J. Durand, and C. Perrin, Phys. Rev. Lett. 27, 1661 (1971)
N.T. Okumusoglu, C.O. Blyth, P.B. Dunscombe, N. Berovic, and J.S.C. McKee, Nucl. Phys. A231, 391 (1974)
A.D. Ijpenberg, R. van Dantzig, B.J. Wielinga, and I. Slaus, in "Few Particle Problems in the Nuclear Interaction", edited by I. Slaus, R.P. Haddock, S.A. Moszkowski and W.T.H. van Oers (North-Holland, Amsterdam, 1972), p. 651

Ca71 R.T. Cahill and I.H. Sloan, Nucl. Phys. A165, 151 (1971)
R. Bouchez, S. Desreumaux, J.C. Gondrand, C. Perrin, P. Perrin, and R.T. Cahill, Nucl. Phys. A185, 166 (1972)

C72 A.A. Cowley, H.G. Pugh, P.G. Roos, G. Tibell, R. Woody in "Few Particle Problems in the Nuclear Interaction", edited by I. Slaus, R.P. Haddock, S.A. Moszkowski and W.T.H. van Oers (North-Holland, Amsterdam, 1972), p. 614 ; Phys. Lett. 46B, 192 (1973); Nucl. Phys. A220, 429 (1974)

C74 R.T. Cahill, Phys. Lett. 49B, 150 (1974)

D62 D.J. Drickey and L.N. Hand, Phys. Rev. Lett. 9, 521 (1962)
D. Benaksas, D. Drickey, and D. Frerejacque, Phys. Rev. 148, 1327 (1966)

D71 J.L. Detch, Jr., R.L. Hutson, Nelson Jarmie, and J.H. Jett, Phys. Rev. C 4, 52 (1971)

E71 W.-D. Emmerich, A. Hofmann, G. Philipp, K. Thomas and F. Vogler, Nucl. Instr. and Meth. 93, 397 (1971)

E72 Wolfgang Ebenhoh, Nucl. Phys. A191, 97 (1972)

F61 L.D. Faddeev, Sov. Phys. JETP 12, 1014 (1961)

F62 E. Ferrari and F. Selleri, Nuovo Cimento Supp. 24, 453 (1962)

F71 R. Frascaria, V. Comparat, N. Marty, M.Morlet, A. Willis, and N. Willis, Nucl. Phys. A178, 307 (1971)

Fo71 D.G. Foster, Jr., and D.W. Glasgow, Phys. Rev. C 3, 576 (1971)

F72 M.J. Fritts and P.D. Parker, Nucl. Phys. A198, 109 (1972)

G51 J.C. Gunn and J. Irving, Phil. Mag. 42, 1353 (1951)

G60 A.M. Green and G.E. Brown, Nucl. Phys. 18, 1 (1960)

Ga60 J.L. Gammel, Fast Neutron Physics (Interscience, New York, 1960), Part II, p. 2185

G64 T.A. Griffy and R.J. Oakes, Phys. Rev. 135, B1161 (1964)

G70 B. Gottschalk and S.L. Kannenberg, Phys. Rev. C 2, 24 (1970)

H57 L. Hulthen and M. Sugawara in "Handbuch der Physik" edited by S. Flugge (Springer-Verlag, Berlin, 1957)

H72 A. Hofmann, G. Philipp, K. Thomas and F. Vogler, Nucl. Instr. and Meth. 101, 467 (1972)

I51 J. Irving, Pil. Mag. 42, 338 (1951)

J73 M. Jain, S.N. Bunker, C.A. Miller, J.M. Nelson and W.T.H. van Oers, Lettere al Nuovo Cimento 8, 844 (1973)

K61 A.F. Kuckes, Richard Wilson, and Paul F. Cooper, Jr., Annals of Physics 15, 193 (1961)

K64 R.J. Kurz, "A 709/7090 FORTRAN Program to Compute the Neutron Detection Efficiency of Plastic Scintillator for Neutron Energies from 1 to 300 MeV", UCRL-11339, Lawrence Radiation Laboratory, March 1964

K72 P. Kitching, G.A. Moss, W.C. Olsen, W.J. Roberts, J.C. Alder, W. Dolhopf, W.J. Kossler, C.F. Perdrisat, D.R. Lehman, and J.R. Priest, Phys. Rev. C 6,769 (1972)

Kn72 H. Knox and T.G. Miller, Nucl. Instr. and Meth. 101, 579 (1972)

K73 W.M. Kloet and J.A. Tjon, Nucl. Phys. A210, 380 (1973)

K74 W. Kluge, R. Schlufter, and W. Ebenhoh, Nucl. Phys. A228, 29 (1974)

L72 D.R. Lehman, Phys. Rev. C 6, 2023 (1972)

L73 T.K. Lim, Phys. Rev. Lett. 31, 1258 (1973); Ibid. 1263
T.K. Lim, Phys. Lett. 47B, 397 (1973)
R.D. Haracz and T.K. Lim, Phys. Rev. C 10, 431 (1974)
R.D. Haracz and T.K. Lim, Phys. Rev. C 11, 634 (1975)

Li73 T.L. Lim, Phys. Lett. 43B, 349 (1973)

M68 T.G. Miller, Nucl. Instr. and Meth. 63, 121 (1968)

Ma68 D.J. Margaziotis, B.T. Wright, and W.T.H. van Oers, Phys. Rev. 171, 1170 (1968)

M69 J.V. Meboniya, Phys. Lett. 30B, 153 (1969)

M70 T.G. Masterson, Nucl. Instr. and Meth. 88, 61 (1970)

M72 C.A. Miller, D.I. Bonbright, J.W. Watson, and F.J. Wilson, in "Few Particle Problems in the Nuclear Interaction", edited by I. Slaus, R.P. Haddock, S.A. Moszkowski, and W.T.H. van Oers (North-Holland, Amsterdam, 1972), p. 731

M74 C.A. Miller, thesis, Physics Department, University of Manitoba 1974, unpublished

M74a C.A. Miller, J.W. Watson, D.I. Bonbright, F.J.S. Wilson, and D.O. Wells, Phys. Rev. Lett. 32, 684 (1974)

M75 J.R. Morales, T.A. Cahill, D.J. Shadoan, and H. Wilmes, Phys. Rev. C 119, 1905 (1975)

P61 J.R. Prescott and A.S. Pupaal, Can. J. Phys. 39, 221 (1961)
L.E. Beghian and S. Wilensky, Nucl. Instr. and Meth. 35, 34 (1965)
R. Honecker and H. Grassler, Nucl. Instr. and Meth. 46, 282 (1962)

P69 E.L. Petersen, R. Bondelid, P. Thomas, G. Paic, J. Reginald Richardson, and J.W. Verba, Phys. Rev. 188, 1497 (1969); Phys. Lett. 31B, 209 (1970); Phys. Rev. Lett. 27, 1454 (1971)

R68 Roderick V. Reid, Jr., Annals of Physics 50, 411 (1968)

R72 J.G. Rogers and D.P. Saylor, Phys. Rev. C 6,734 (1972)

R76 J.G. Rogers, Private Communication, 1976

S64 B.K. Srivastava, Phys. Rev. 133, B545 (1964)

S68 I.S. Sherman, R.G. Roddick and A.J. Metz, IEEE Trans. Nucl. Sci. NS-15, 500 (1968)

Sh68 I.S. Shapiro, Sov. Physics Uspekhi 10, 515 (1968)

S69 I.H. Sloan, Phys. Rev. 185, 1361 (1969)
R.D. Amado and M.H. Rubin, Phys. Rev. C 7, 2151 (1973)

S70 J.D. Seagrave, in "The Few Particle Problem in Nuclear and Particle Physics", edited by J.S.C. McKee and P.M. Rolph (North-Holland, Amsterdam, 1970), p. 41

S171 I. Slaus, M.B. Epstein, G. Paic, J.R. Richardson, D.L. Shannon, J.W. Verba, H.H. Forster, C.C. Kim, D.Y. Park and L.C. Welch, Phys. Rev. Lett. 27, 751 (1971); Phys. Lett. 36B, 305 (1971); Nucl. Phys. A199, 225 (1973)

St71 N.R. Stanton, "A Monte Carlo Program for Calculating Neutron Detector Efficiencies in Plastic Scintillators", Ohio State University Preprint C00-1545-92, Feb. 1971

S73 Ivo Slaus,R.G. Allas, L.A. Beach, R.O. Bondelid, E.L. Petersen, J.M. Lambert, and D.L. Shannon, Phys. Rev. C 8, 444 (1973)

S74 M.R. Strayer and P.U. Sauer, Nucl. Phys. A231, 1 (1974)

T58 H. Tyren, G. Tibill, and Th.A.J. Maris, Nucl. Phys. 7,281 (1958)

T62 S.B. Trieman and C.N. Yang, Phys. Rev. Lett. 8, 140 (1962)

T74 E.S.Y. Tin, thesis, Physics Department, University of Manitoba 1974, unpublished

V71 V. Valkovic, D. Rendic, V.A. Otte, W. von Witsch, and G.C. Phillips, Nucl. Phys. A166, 547 (1971); A182, 225 (1972); A183, 126 (1972); A183, 145 (1972)

Va71 W.T.H. van Oers, Particles and Nuclei 2, 207 (1971)

W52 K.M. Watson, Phys. Rev. 88, 1163 (1952)
A.B. Migdal, Sov. Phys. JETP 1, 2 (1955)

W70 J.W. Watson, thesis, Physics Department, University of Maryland 1970

W71 B.J. Wielinga, A.D. IJpenberg, K. Mulder, R. van Dantzig, and I. Slaus, Phys. Rev. Lett. 27, 1229 (1971)

Wi71 F.J. Wilson, Private Communication, 1971

Wo71 A. van der Woude, M.L. Halbert, C.R. Bingham, and B.D. Belt, Phys. Rev. Lett. 26, 909 (1971); Ibid. 1124
L.E. Williams, C.J. Batty, B.E. Bonner, C.Tschalar, H.C. Benohr, and A.S. Clough, Phys. Rev. Lett. 23, 1181 (1969)

Y54 Yoshio Yamaguchi, Phys. Rev. 95, 1628 (1954)

Y67 O.A. Yakubovsky, Sov. J. Nucl. Phys. 5, 937 (1967)
L.D. Faddeev, in "The Three Body Problem in Nuclear and Particle Physics", edited by J.S.C. McKee and P.M. Rolph (North-Holland, Amsterdam, 1970)
V.F. Kharchenko and V.E. Kuzmichev, Nucl. Phys. A183, 606 (1972)
C.O. Alt, P. Grassberger and W. Sandhas, Phys. Rev. C 1, 85 (1970)
Ian. H. Sloan, Phys. Rev. C 6, 1945 (1972)